Theses and Dissertations

Spring 2015

Multimodal nanoparticles for image-guided delivery of mesenchymal stem cells in the treatment of myocardial infarction

Sean Sweeney
University of Iowa

Recommended Citation

MULTIMODAL NANOPARTICLES FOR IMAGE-GUIDED DELIVERY OF
MESENCHYMAL STEM CELLS IN THE TREATMENT OF MYOCARDIAL
INFARCTION

by

Sean Sweeney

A thesis submitted in partial fulfillment
of the requirements for the Doctor of Philosophy
degree in Biomedical Engineering in the
Graduate College of
The University of Iowa

December 2015

Thesis Supervisor: Adjunct Associate Professor Jose Assouline

Graduate College
The University of Iowa
Iowa City, Iowa

CERTIFICATE OF APPROVAL

_____

PH.D. THESIS

_____

This is to certify that the Ph.D. thesis of

Sean Sweeney

has been approved by the Examining Committee for
the thesis requirement for the Doctor of Philosophy degree
in Biomedical Engineering at the December 2015 graduation.

Thesis Committee: _____
                   Jose Assouline, Thesis Supervisor

                   _____
                   Tae-Hong Lim

                   _____
                   Joseph Reinhardt

                   _____
                   Edwin Dove

                   _____
                   Eric Hoffman

To Ken, Heather, and all my family and friends that supported me throughout the process.

ACKNOWLEDGEMENTS

ABSTRACT

One of the leading causes of death and hospital stays in the United States, myocardial infarction (MI) occurs when coronary blockages lead to downstream ischemia in the myocardium. Following the MI, the heart activates a number of pathways to repair or remodel the infarcted zone. Endothelial cells respond to ischemia by de-differentiating to form neovasculature and myofibroblasts. The resident cardiac differentiable stem cells (CDCs) are recruited via local cytokines and chemokines to the infarct zone where they too differentiate into myofibroblasts. Mesenchymal stem cells (MSCs) of the bone marrow respond to circulating factors by immobilizing to the heart and differentiating down cardiac lineages. In regenerative medicine approaches, these processes are exploited to augment the resident supply of reparative cells.

Clinical trials to transplant cardiac stem cells into MI zones have been met with mixed results. When CDCs are harvested from autologous or type-matched donors, the cells are prepared with a minimum of manipulations, but the yield is quite small. Conversely, MSCs from bone marrow are highly proliferative, but the manipulations in culture required to trigger cardiac differentiation have been found to transform the cell into a more immunogenic phenotype. In addition, there is a dearth of *in vivo* evidence for the fate of transplanted cells. Currently, intracardiac echocardiographs are used to assess the infarcted area and to guide delivery of stem cell transplants. However, this modality is invasive, short-term, and does not image the transplanted cells directly.

In this project, I addressed these shortcomings with a regenerative medicine and bioimaging approach. Our lab has developed multimodal nanoparticles based on a core of mesoporous silica, functionalized with fluorescein or tetramethylrhodamine

isothiocyanate for visibility in fluorescent microscopy, Gd_2O_3 for magnetic resonance imaging (MRI), and trifluoropropyl moieties for ultrasound applications. After establishing *in vitro* models of cardiac stem cells using CDCs and MSCs, the particles were implemented and characterized *in vitro*. At a concentration of 125 µg/mL in culture, the particles are highly biocompatible, and labeled cells were found to be fluorescent, echogenic, and detectable with MRI in prepared agar phantoms. *Ex vivo* mouse hearts, first mounted in agar phantoms, then left *in situ*, were implemented as a model for guided delivery using ultrasound and follow-up cell tracking with MRI.

These results in this project demonstrate the feasibility of this highly novel and practical approach. Additional studies will be carried out to evaluate the biocompatibility and retention versus clearance in live animal models, prior to the carrying out of true pre-clinical models for myocardial infarction.

PUBLIC ABSTRACT

Every year in the U.S. an estimated 1.5 million individuals suffer a first, recurrent, or "silent" heart attack, causing a total financial burden of $11.5 billion. After a heart attack, several processes activate the body's native stem cell population to repair the heart, using resident stem cells from the heart as well as mobilized stem cells from the bone marrow. Over the past 2 decades, clinical trials have performed stem cell transplants to provide an additional supply of cells to the heart for it to repair itself. Results have been mixed, and one factor is the requirement for precise placement of the transplanted cells. Current approaches are invasive, short-lived, and only track the damaged tissue, not the transplanted cells themselves.

In order to address these shortcomings, I have evaluated a novel approach for direct, non-invasive tracking of stem cells transplanted following heart attack. Our lab has developed nanoparticles that are engulfed by the stem cells. Labeled cells are tracked using ultrasound during the transplantation procedure, and follow-up ultrasound and MRI scans can be used to verify that the transplanted cells remain in their desired location. This novel technology represents a new approach to tracking stem cells in clinical applications as well as gathering new data about heart repair in animal models.

TABLE OF CONTENTS

LIST OF TABLES

LIST OF FIGURES

PREFACE

I see the work presented herein as the culmination of all my years of post-high school study. As an undergraduate, I joined Dr. Assouline's lab to learn about cell biology, producing a senior design project in which the oxygen consumption of cells would be measured during 3 dimensional growth on hollow fiber bioreactors with stem cell applications. In my Master's thesis, I studied a number of mesenchymal stem cell applications and tracking options with a variety of nanoparticles in various tissues of the body. Using this as a foundation, in my Ph.D. research I chose to focus on one biomedical problem-myocardial infarction-implementing one solution, and taking it as far as possible towards its completion.

CHAPTER 1: INTRODUCTION

Background/significance

Myocardial infarction regenerative medicine: major players/pathways

In the United States, nearly 1.5 million people suffer a first, recurrent, or "silent" myocardial infarction (MI) each year[1]. These events account for about 612,000 hospital stays, with a financial burden of about $11.5 billion. The 12 month survival rate for MI has increased with improvements to care to about 85%. The downside to this is a concomitant increase in the number of patients whose hearts undergo cellular remodeling, usually to the detriment of cardiac output.

An MI occurs when blood flow to the myocardium is blocked long enough to cause an ischemic injury to the affected tissue; following MI, the affected myocardium undergoes numerous remodeling events. Endothelial cells near the coronary blockage respond to ischemia by de-differentiating, and are capable of forming neovasculature as well as myofibroblasts, the progenitors to myocardium[2-4]. The resident cardiac progenitor cells respond to local chemokines and cytokines, among which Notch1, Wnt, and Jagged1 are primarily observed, by also moving to the infarcted area and differentiating into myofibroblasts[2,5]. Lastly, mesenchymal stem cells of the bone marrow respond to factors circulating in the bloodstream by mobilizing and circulating to the heart where they too have the capacity for cardiac differentiation[2,6].

In the absence of sufficient repair mechanisms, white blood cells (neutrophils) infiltrate the damaged tissue and activate matrix metalloproteinases, which degrade the collagen that makes up the extracellular matrix, leading to wall thinning and mechanical stress. The long-term responses to this stress include hypertrophy of remaining

cardiomyocytes and infiltration of fibroblasts that remodel the collagen matrix in the

infarct zone[7-11]. The remodeled infarct is therefore fibrous rather than muscular, and

incapable of coordinated contraction with the remainder of the heart, which undergoes

additional, compensatory hypertrophy (figure 1).
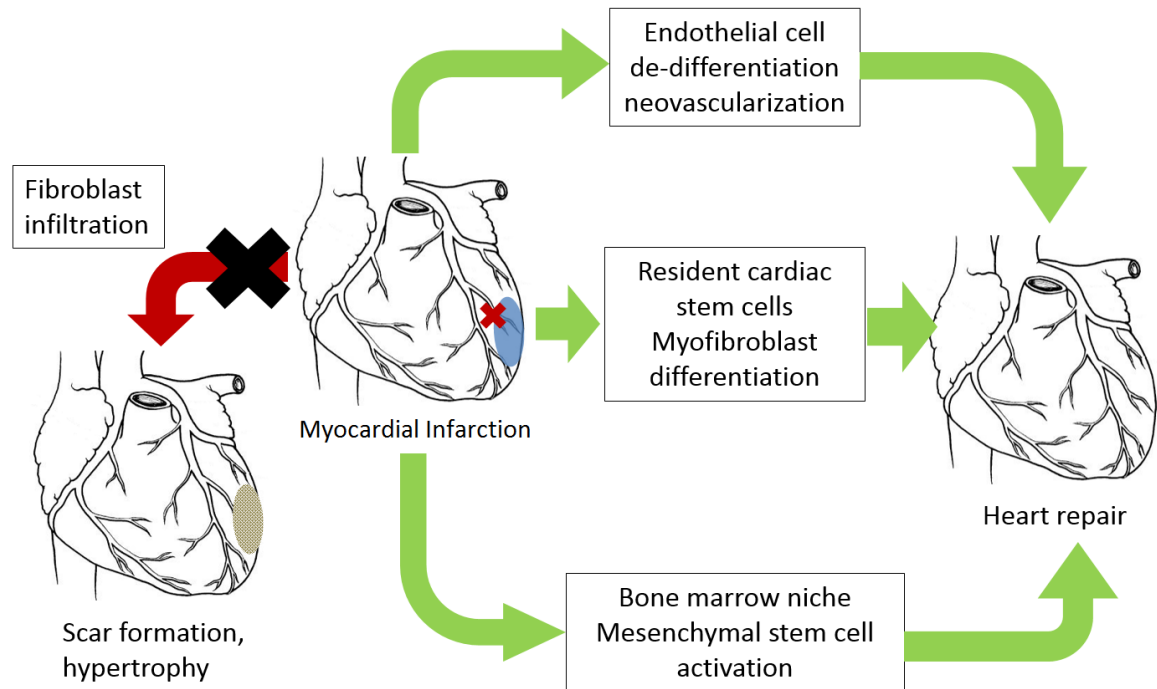
Figure 1. Illustration depicting the mechanisms of cardiac repair versus scar tissue

formation. Three sources of stem cells (endothelial cells, resident cardiac stem cells, and

bone marrow mesenchymal stem cells) are recruited via paracrine and endocrine

signaling to differentiate into myofibroblasts and inhibit scar formation.

Many pre-clinical and clinical studies have attempted to augment healthy repair and suppress scar formation by transplanting autologous cells from various sources into the infarcted heart (Table 1). A number of sources have been identified for these cells, including mesenchymal stem cells (MSCs) derived from bone marrow, adipose tissue-derived regenerative cells (ADRCs), and cardiac-derived stem cells (CDCs) derived from heart biopsy[2-6,12]. MSCs are easily isolated from bone marrow aspirates due to their adherence in tissue culture, and are characterized by their positive expression of, among other markers, STRO-1, CD29, CD44, CD71, CD90, CD106, CD124, SH2, and SH3[13,14].

While the cell yields can be favorable for MSCs and ADRCs, an important consideration is the immune response to transplantation of these cells. The immunomodulatory properties of MSCs are not fully understood; the consensus is that MSCs are positive for major histocompatibility complex (MHC) class I, but negative for MHC class II[14]. Positive expression of MHC class I is important for evasion of deletion by natural killer (NK) T-cells, while the absence of MHC class II alloantigens allows for the escape of recognition by CD4 T-cells. MSCs also lack several other surface markers known for T cell induction: CD80, CD86, and CD40[14]. To that end, many studies have found evidence that MSCs do not induce proliferative T-cell responses, even in mismatched tissue types[15-24]. Despite strong evidence for immune evasion/suppression by MSCs *in vitro*, several studies have demonstrated immunogenicity in animals[25-27]. This phenomenon may be related to levels of interferon gamma (IFN-γ)[26,27], the differentiation stage of the cells used, or mechanical factors related to the injection process[28]. Additionally, the manipulations required to push the cells towards cardiac differentiation, such as culture in a defined cytokine cocktail, may contribute to the

immune rejection of these cells, regardless of whether they come from autologous

sources. Other factors often associated with myocardial infarction, such as advanced age,

diabetes, or renal failure, also negatively affect the capacity for MSC differentiation[29,30].

Conversely, CDCs are already partially committed towards cardiac differentiation,

so fewer manipulations are needed; however, these cells may not be present in sufficient

numbers to significantly affect regeneration. CDCs are identified histologically by

positive expression of the c-kit marker; in adult rats, Beltrami et al identified an average

of 1 c-kit positive cell for every 10^4 mature cardiomyocytes[31]. Thus, a small biopsy is

likely to produce a very low yield of useable stem cells.

Results from clinical and pre-clinical trials have been mixed—even when cardiac

function is improved, the engraftment and role of MSCs is unclear. In a pre-clinical trial

of 27 adult rats, Hou, et al injected isolated MSCs of human patients with coronary artery

disease. Although left ventricular function was improved and remodeling and

neovascularization was observed 4 weeks after transplantation, very few cardiomyocytes

of human origin were observed in the infarct. The few MSCs that engrafted stained

positive for desmin, a marker of immature myocytes[32]. Hida, et al, derived human MSCs

from menstrual blood rather than bone marrow. When induced for cardiac

differentiation, about 30% of the cells contracted spontaneously, and when transplanted

as a sheet onto the infarcted surface of nude rat hearts, ventricular function was improved,

though the graft did not incorporate itself into the host tissue, merely lying atop it[33]. In

another xenomodel, Grinnemo et al injected human MSCs into nude and

immunocompetent Fischer rats, with our without immunosuppression. They observed

that cells engrafted only in immunosuppressed animals, and cells that did engraft did not

affect myocardial function[34]. In a clinical trial of 11 patients, Katritsis et al transplanted a mix of MSCs and endothelial progenitor cells (EPCs, to promote angiogenesis) via left anterior descending coronary artery. Improvement of myocardial contractility was seen in 5 of 11 patients 4 months following the transplant[35].

Because of the large differences between these studies, it is difficult to identify specific variables leading to their respective success or failure. While the optimal conditions for isolation, culture, and cardiac differentiation of MSCs have not yet been agreed upon, it is clear that placement of the cells is critical to the ability of the transplant to affect myocardial regeneration. If the cells are placed too far towards the middle of the infarct, there will be insufficient blood supply and important microenvironmental cues (growth factors, electrical activity, etc) will not be present. Placement of the stem cells in healthy myocardium would only contribute to the cardiac hypertrophy already underway. Therefore, a system that provides cell tracking during and after transplantation would be of great benefit to the patient's prognosis.

Table 1. Summary of cardiac regenerative stem cell transplant pre-clinical trials

Cell type	Outcomes	References
• Mesenchymal stem cells, Adipose tissue-derived regenerative cells	• High yield • Immunomodulatory *in vitro*; reported immunogenicity *in vivo*	15-30
• Cardiac-derived stem cells	• Low yield (1 cell per 10^4) • Infarctions are reduced but long-term electrical coupling *in vivo* is not shown	31-35

Ultrasound imaging: applications for guidance, rapid cell tracking

Non-invasive contrast imaging is a rapidly expanding market in medicine; in a
Kalorama Inc. report, the market for medical contrast agents is projected to reach $15
billion by 2015[36]. Of particular interest is in new agents for multimodal and/or targeted
imaging which promise to specifically highlight tissues or pathologies of interest. Novel
medical treatments such as stem cell transplants and chemotherapeutic drug delivery will
benefit greatly from these types of novel agents. Because different tissues are involved,
different imaging modalities will be needed—for example, imaging in the brain works
very well with magnetic resonance imaging (MRI), but less so with computed
tomography (CT). Lungs can be observed in CT, but not as easily in MRI. Therefore, an
agent with the versatility to enhance contrast in multiple imaging modalities (MRI, CT,
ultrasound, and/or fluorescence imaging) would be beneficial for these new technologies.

Among these imaging modalities, ultrasound is perhaps the fastest, safest, and
least expensive way to obtain *in situ* images, as it requires only a few seconds of
preparation with ultrasound gel and produces no ionizing radiation. The drawback is that
the spatial resolution does not approach what is possible in CT or MRI at this time. In
this modality, a piezoelectric transducer produces sound at high frequencies (typically
between 2 and 15 MHz for clinical applications and up to 40 MHz or more for research
applications) and generates an image based on the timing of echoes returning to the
transducer. Echoes are generated when the propagated sound wave strikes an interface
between volumes with differing acoustic impedances (Z) and part of the sound wave
reflects back to the transducer. Acoustic impedance is defined as

$$Z = \rho c,$$

where ρ is the density and c is the speed of sound in the tissue[37]. At the interface between

two tissues with different mechanical properties, the normal incidence pressure reflection

coefficient (R) describes the fraction of sound energy that will be reflected back to the

transducer. The remaining fraction continues propagating deeper into the tissue where it

may strike another interface. R is related to the acoustic impedances of the two tissues at

the interface (Z_1 and Z_2) according to the equation

$$R = \frac{Z_2 - Z_1}{Z_2 + Z_1}.$$

These principles are applied to the generation of ultrasound images. In A-mode

imaging, one transducer is used to plot all the tissue boundaries along one axis as a

function of time. One application of A-mode imaging is tracking opening and closing of

heart valves or movement of a ventricle during the heart cycle in echocardiography. In

B-mode imaging, an array of transducers is coordinated to form a 2-D image. This may

be the most common way ultrasound is used, and includes fetal sonography among other

applications. Newer ultrasound systems are capable of Doppler mode, in which

frequency shifts in the sound wave are used to calculate blood flow through arteries, and

even 3-D ultrasound, in which the transducers are swept across many 2-D fields in rapid

succession to generate a 3-dimensional image[37].

Contrast echocardiography is a particular niche in the larger ultrasound imaging

modality, in which sound waves are transmitted through tissue and images are formed

based on the timing of echoes returning to the transducer. When imaging the heart in

echocardiography, contrast agents are used to highlight features when the patient presents

with obstacles to non-contrast echocardiography, such as obesity and lung disease. Three

echocardiography contrast agents are currently approved and used clinically (Table 2),

which consist of various polymers encapsulating high molecular weight gases[38]. These "microbubbles" have a dramatically slower speed of sound compared with soft tissue, giving rise to a greater contrast.

Table 2. Clinically available echocardiography contrast agents

Name	SonoVue®	Optison®	Definity®
Gas type	Sulphur hexafluoride	Perflutren	Octafluoropropane
Mean Diameter	2.5 µm	3.0-4.5 µm	1.1-3.3 µm
Shell	Surfactant/powder	Human albumin	Lipid

Commercial echocardiography contrast agents currently available are all 1-5 μm in diameter. These are sufficiently large that a relatively few particles accumulating in a given volume can alter the acoustic impedance to generate contrast. However, in certain applications, these materials can be too large. For example, many drug and contrast agents take advantage of the "leaky" nature of tumor vasculature, where gaps in the endothelium are typically between 400 and 800 nm[39]. In these instances, sub-micron ultrasound agents are being used experimentally. These agents tend to be in one of two categories: "nanobubbles," smaller versions of the lipid-encapsulated-gas microbubbles[40], and solid particles, such as silica nanobeads. Using agarose gel plates as phantoms, Casciaro et al measured the signal for silica concentrations up to 0.8 wt%. The particles could also be automatically detected using RF signal analysis[41]. Similarly, Milgroom et al used mesoporous silica nanoparticles as ultrasound contrast agents targeted to breast cancer cells *in vitro*.[42]

Two other papers show ultrasound contrast of injected stem cells labeled with metallic nanobeads. Bara et al used magnetic cell separation to isolate the CD34+/CD133+ population, now labeled with 50 nm dextran-coated iron beads, from bone marrow aspirates, then injected boluses of these cells into the myocardium of domestic pigs. Transesophageal echocardiography (TEE) was performed immediately before and after two injections were made. Injections of particles alone as well as unlabeled cells were made as controls. The TEE revealed good contrast originating from the dextran-iron beads[43]. Mallidi, et al, conjugated 50 nm gold nanoparticles to A431 cancer cells expressing high levels of epidermal growth factor receptor (EGFR) and imaged these cells using ultrasound and photoacoustic imaging (a combination of

ultrasound and laser optical microscopy). Various concentrations of labeled cells were suspended in gelatin phantoms and imaged, with contrast seen at 31,000 cells and $3.1*10^7$ nanoparticles per mL^{44}.

Ultrasound waves that strike small particles undergo Rayleigh scattering, causing local variations in detected amplitude (speckle) to vary following a probability density function $p(A) = \frac{2A}{A_{MS}} e^{\left(\frac{-A^2}{A_{MS}}\right)}$,

where p(A) is the probability of amplitude A, and A_{MS} is the mean of the squared amplitudes[45]. In other words, speckling caused by microscopic inhomogeneities in the medium adds noise with a range of amplitudes from bright to dark that imparts a grainy quality to the image. This principle is applied below to the analysis of ultrasound phantoms in agar.

Magnetic resonance imaging, cell tracking applications

While ultrasound is beneficial for real-time imaging applications, such as image-guided delivery of a catheter to the border zone of an MI, it suffers from poor spatial resolution and signal-to-noise ratios when compared with other modalities, such as MRI. Briefly, MRI uses small variations in the magnetic field arising from differing proton spin densities $\rho(x,y)$ in tissue to generate its images. The grayscale value at each pixel in a slice of an MR image is the 2-dimensional inverse Fourier transform of that slice's k-space, or frequency domain s(t). The radio frequency (RF) data encoded in the frequency domain is collected when small perturbations are made in the larger magnetic field of the MR scanner using smaller gradient coils that vary over time as $G_x(t)$ and $G_y(t)$. The general equations describing the signal are

$$s(t) = \int_{-\infty}^{\infty} \int_{-\infty}^{\infty} \rho(x,y) e^{-j2\pi[k_x(t)x + k_y(t)y]} dx dy,$$

where

$$k_x(t) = \int_0^t \frac{\gamma}{2\pi} G_x(\tau) d\tau, \text{ and}$$

$$k_y(t) = \int_0^t \frac{\gamma}{2\pi} G_y(\tau) d\tau.^{37}$$

The MR signal of a specific tissue can also be described by its parameters (T_1, T_2, T_2^* relaxation times) and the parameters of the scan (repetition time TR, echo time TE, and/or flip angle α). After a material is magnetized with a certain flip angle α, the magnetic field in the longitudinal axis M_z decays (relaxes) with time constant T_1, and varying the time between pulses (repetition time T_R), tissue with different T_1 relaxation times show up with different levels of intensity in the reconstructed image. This is known as a T_1-weighted image. In a T_2-weighted image, the echo time T_E (the time between the pulse and the midpoint of signal readout) is used to generate differing intensities between tissues of different T_2/T_2^* relaxation times (the time constant of relaxation or "de-phasing" in the transverse plane, or M_{xy})[37,46].

Weighting is controlled by the MRI operator typically by varying the echo time (T_E) or relaxation time (T_R); T_1-weighted scans typically have a short (<750 ms) T_R and short (<40 ms) T_E, while T_2-weighted scans have a longer (>1500 ms) T_R and longer (>75 ms) T_E. A third imaging strategy using long (>1500 ms) T_R and short (<40 ms) T_E minimizes T_1 and T_2 effects to generate an image based more on proton density. On the Varian® 4.7 T small animal scanner, we have optimized our scan parameters for proton density with slight T_1- and T_2-weighting; a typical T_1 weighted scan has a T_R of 800 ms and a T_E of 15 ms, while a typical T_2-weighted scan has a T_R of 2300 ms and a T_E of 15 ms. Using these parameters, the T2-weighted scan typically provides better anatomical details, while both T1- and T2-weighted scans are enhanced by contrast agents.

Besides varying T_R/T_E on the scanner to achieve the desired contrast, additional contrast can be achieved by using one of several contrast agents. MRI contrast agents are ferromagnetic, paramagnetic, or superparamagnetic materials which interact with the protons present in the surrounding medium, thereby altering the apparent T_1 or T_2 relaxation time. The effect of contrast agents on the observed T_1 or T_2 value is given by the equation

$$\frac{1}{T_{obs}} = \frac{1}{T_{tissue}} + r[contrast],$$

where T_{obs} is the observed T_1 or T_2 value, T_{tissue} is the actual T_1 or T_2 relaxation time of the tissue being scanned, r is the r_1 or r_2 relaxivity of the contrast agent, measured in $s^{-1} \cdot mM^{-1}$, and [contrast] is the molar concentration of the contrast agent[47]. The r_1 and r_2 relaxivities of many common contrast agents available at the time were measured at 0.47, 1.5, 3, and 4.7 T, with increasing field effects seen for both r_1 and r_2 as magnetic field increased[48]. One common contrast agent, superparamagnetic iron oxide nanoparticles (SPIONs)[49,50] have very high r_2 relaxivity values, but do little to alter T_1 relaxation.

Many clinical contrast agents are based on chelated gadolinium ions (Gd^{3+}); with 7 unpaired electrons in its outer shell available to interact with protons, gadolinium is a potent contrast agent with a high r_1 relaxivity but a relatively low r_2[51]. Many contrast agents are now being studied which are based on gadolinium oxide (Gd_2O_3) nanoparticles; these have moderate values for both R_1 and R_2 and thus can provide contrast in T_1- and T_2-weighted MRI. Thus, gadolinium-based contrast agents are thought of primarily as T_1 contrast agents, though investigators are studying the T_2 effects of gadolinium in various applications. For example, Park et al found the r_1 and r_2 value of their 1 nm Gd_2O_3 nanoparticles to be 9.9 and 10.5 $s^{-1} \cdot mM^{-1}$, respectively[52]. Faucher, et

al synthesized poly(ethylene glycol) (PEG)-Gd_2O_3 nanoparticles with the Gd_2O_3 core

being 1.3 or 3 nm in diameter, and a hydrodynamic diameter after PEG addition of 9.1

nm. At magnetic fields ranging from 0.47 T to 11.7 T, the larger-cored particles had r_1

and r_2 values which ranged from 2.28 to 3.42 and 2.99 to 15.9 $s^{-1}\cdot mM^{-1}$, respectively, with

smaller r_1 and larger r_2 values at larger magnetic fields. The smaller-cored particles had

much larger r_1 and r_2 values which ranged from 10.4 to 16.2 and 15.9 to 17.7 $s^{-1}\cdot mM^{-1}$,

respectively[53]. Hedlund et al synthesized a Gd_2O_3 colloid (particle size not reported) and

exposed BaF3 and THP-1 cells to a range of concentrations of the colloid. The measured

r_1 and r_2 relaxivities of the labeled cells were 3.6–5.3 $s^{-1}\cdot mM^{-1}$ and 9.6–17.2 $s^{-1}\cdot mM^{-1}$,

respectively[54]. Lee, et al, found a T_2-shortening effect in phantom studies using two

different gadolinium chelates: Gd-DTPA (Bayer Magnevist®) and Gd-EOB-DTPA

(Bayer Primovist®) at 1.5 and 3 T[51].

Additional methodologies: x-ray computed tomography, positron emission

tomography, fluorescent microscopy

Unlike MRI in which the contrast is derived from magnetic properties of tissue,

CT images are essentially based on the density of the tissue in the path of the x-rays. In

summary, x-ray photons at a known energy are projected towards the patient and detected

on the other side. The simplified equation of intensity of the photons striking the detector

is given by the relationship

$$I(x) = I_0 e^{-\mu x},$$

where I_0 is the initial intensity and μ represents the attenuation coefficient of the material

(a function primarily of tissue density). In order to generate a multislice CT image, this

principle is expanded to a 2 dimensional detector which can be rotated around the body.

Many 2-D projections are compiled into a 3-D image according to the equation

$$P^{\theta k} = I_0 e^{-\Sigma_{ij} W_{ij}^{\theta k} \mu_{ij}},$$

where $P^{\theta k}$ is the projection data for detector position k and angle θ, $w_{ij}^{\theta k}$ is a weighting

value for position (i,j) on the detector at position k and angle θ, and μ_{ij} is the attenuation

of the material at position (i,j)[37].

In x-ray CT, contrast agents are effective if they have an ability to greatly change

the x-ray opacity of the tissue of interest. Therefore most of the early contrast agents

were based on heavy elements such as iodine and barium. Because of toxicity concerns,

these agents have evolved over time, and other contrast agents based on electron-dense

metals have also been studied, and are well reviewed by Yu/Watson[55]. Of the novel

heavy metal contrast agents, those based on gold, bismuth and gadolinium are the most

actively researched to date.

The use of metallic nanoparticles as a label for tracking cells in vivo using CT has

not been studied as extensively as MRI; nevertheless, a number of related reports have

been published. Hainfield, et al first injected mice subcutaneously with carcinoma cells,

then followed 10 days later with a tail vein injection of 1.9 nm gold nanoparticles at a

concentration of 2.7 mg of gold per gram of mouse weight. Using a mammography

scanner, the mice were scanned with a photon energy of 22 kVp for a duration of 0.4 s.

The nanoparticles enhanced the contrast in the vasculature, particularly highlighting areas

of higher blood flow (the subcutaneous tumors). After 60 minutes, the particles were

cleared by the kidneys in an equally efficient manner compared with commercially

available iodinated contrast agents[56]. A similar study by Rabin et al produced equally

promising results using 10-40 nm bismuth sulfide nanoparticles[57]. In order to improve

the contrast agent biocompatibility, Cormode et al synthesized high density lipoproteins

(HDLs) loaded with 5.6 nm gold nanoparticles and observed uptake by macrophages

followed by a significant increase in CT contrast compared with unlabeled cells *in*

vitro[58,59]. Thus, while CT is a viable approach for the intracellular labeling and tracking

of transplanted cells, it is still a less attractive option than ultrasound or MRI, due to the

exposure to ionizing radiation from the x-rays as well as toxicity concerns with many of

the contrast agents themselves.

Similarly, nuclear imaging, which includes both positron emission tomography

(PET) or single photon emission computed tomography (SPECT) exposes the patients to

a radioactive tracing agent. In addition, CT scans are typically the base image upon

which the PET/SPECT image is overlaid; thus the patient is exposed to ionizing radiation

from the scanner as well. In PET, a radionuclide (typically ^{18}F-radiolabeled

fluorodeoxyglucose, or ^{18}F-FDG) is injected intravenously. Radioactive decay produces

a positron which annihilates upon collision with an electron, releasing two gamma

particles in opposing directions, which strike a detector. The ^{18}F-FDG is taken up at

greater rates in areas of highest glucose consumption (i.e., metabolic activity)[37]. In this

way, rapidly dividing tumors appear as highly active regions throughout the body. A

typical radiation dose from ^{18}F-FDG is about 14 mSv; for comparison, the effective

exposure of a year in Denver, CO, is about 12 mSv and a full-body CT scan ranges from

6-30 mSv[60,61]. The biological half-life, describing the clearance rate by the kidneys and

not to be confused with the radioactive half-life, is typically about 2 hours.

In SPECT, the use of radionuclides and detection of emitted gamma rays are similar to that of PET, but the radionuclides involved do not have the intermediate step of positron emission. One commonly used radionuclide in SPECT is the metastable nuclear isomer of technetium-99 (^{99m}Tc), which can be covalently linked to nearly any molecule for tracing. Other SPECT radionuclides include ^{123}I, ^{131}I, and ^{111}In. These all have biological half-lives of about 1 day.

Most PET radionuclides have shorter radioactive half-lives than those used for SPECT: ^{18}F (110 minutes) is longer-lived than others which include ^{11}C (20 minutes), ^{13}N (10 minutes), ^{15}O (2 minutes), ^{82}Rb (1.3 minutes) and ^{68}Ga (67 minutes), but shorter-lived than ^{89}Zr (78 hours)[62]. The half-lives of SPECT radionuclides range from 6 hours for ^{99m}Tc, 13 hours for ^{123}I, 67 hours for ^{111}In, to 8 days for ^{131}I[63]. While the short half-lives are critical for reducing the patient's radiation dose, it presents two great difficulties. First, the radionuclides must be generated in a location adjacent to the PET/SPECT scanner on an as-needed basis. This, in addition to the expense of the scanners themselves, make PET/SPECT imaging very costly to perform. Secondly, the use of radionuclides as stem cell tracers is made less viable, as it may take up to 4 or more hours for stem cells to engulf the nuclides prior to injection, while after injection, the cells may only be traceable for a few days[64]. As an example, Kim et al radiolabeled rat ADSCs with ^{124}I-hexadecyl-4-iodobenzoate and ^{18}F-FDG and transplanted cells in a rat model for MI; while the immediate signal was very strong, only a trace signal from the ^{124}I was detectable 3 days after transplantation. In this study as well as a porcine study by Doyle et al, the signal from ^{18}F-FDG-labeled stem cells was only detectable for 2 hours[65,66].

Compared with the other imaging modalities, fluorescence is a much older and simpler form of imaging. Put simply, an electron in its ground state S_0 is excited to a higher state S_1 by a photon of a particular wavelength v_{ex}:

$$S_0 + hv_{ex} \rightarrow S_1,$$
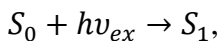
where h is Planck's constant. As the electron returns to its ground state, it emits a photon of a lower energy v_{em} (longer wavelength) and releases some energy in the form of heat:

$$S_1 \rightarrow S_0 + hv_{em} + heat.^{67}$$
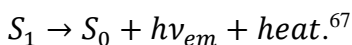
Fluorescence has been used in biology for tracing/reporting countless molecules and processes for decades through the use of organic fluorophores. Among the most popularly used organic fluorophores are 4',6-diamidino-2-phenylindole (DAPI; v_{ex} = 358 nm; v_{em} = 461 nm), green fluorescent protein (GFP; v_{ex} = 488 nm; v_{em} = 509 nm), fluorescein isothiocyanate (FITC; v_{ex} = 495 nm; v_{em} = 519 nm), and tetramethyl rhodamine isothiocyanate (TRITC; v_{ex} = 557 nm; v_{em} = 576 nm). While very useful in laboratory experiments involving cellular labeling, the clinical use of fluorescent dyes is limited to niche applications such as the tracing of lymphatic vessels to the sentinel lymph node during tumor resection[68-70]. More recently, quantum dots (QDs), nanoparticles of cadmium, cadmium selenite, and/or zinc sulfide, have emerged as alternatives to organic fluorophores. While they do possess very narrow excitation peaks related to their particle diameter, they cannot replace organic fluorophores in vivo due to the high toxicity of these heavy metals[71-75].

Innovation: multimodal nanoparticles

To summarize the problem, MI is a significant contributor to extended hospital stays in the U.S. While a number if innate pathways exist for cardiac regeneration, they

are insufficient to repair tissue as large as an infarction; thus, tissue engineering approaches are being tested which augment the endogenous supply of stem cells. However, guidance of these transplants is limited by current imaging approaches-the cells are not labeled internally and thus not tracked directly. In order to improve the quality of the cell transplant, image-based data before, during, and after the transplantation is needed.

Based on these needs, our lab has engineered a novel contrast agent that generates contrast in ultrasound and MRI, as well as fluorescent microscopy, particularly suited for applications such as stem cell tracking in MI[76-82]. Using an MSN at the core, the particle is further functionalized by incorporation of gadolinium oxide into the silica matrix for MRI contrast enhancement, and with perfluorocarbon functional groups on the large MSN surface area for ultrasound contrast enhancement. Using the following methodology, I propose the proof-of-concept of these particles in this specific medical application.

One of the focus areas of the Assouline lab is development of materials and techniques with clinical applications for non-invasive tracking of transplanted stem cells. As stem cell therapies become more prevalent in pre-clinical and clinical settings, the need for these techniques is also expanding. In my Master's research, my goals were to validate novel mesoporous silica nanoparticles (MSN) and europium-doped gadolinium nanoparticles as biocompatible, particularly with STRO-1$^+$ mesenchymal stem cells (MSCs), and as multifunctional, with respect to the imaging modalities in which they can be used. Several types of nanoparticles were discussed in my thesis, but each type was observed using a combination of two or more of the following modalities: magnetic

resonance imaging (MRI), x-ray/computed tomography (CT), and fluorescent

microscopy. We also began to evaluate these particles as contrast agents for

ultrasound/echocardiography applications. As a broad survey of materials and imaging

modalities, my M.S. thesis was intended to lay the groundwork for a Ph.D. project in

which I focus on just one type of particle and clinical application and take it as close as

possible to a finished product, to ultimately be tested in pre-clinical and clinical settings.

There are a myriad of novel stem cell therapies currently being studied, but one of the

most active areas of research is in regeneration of healthy heart tissue following

myocardial infarction (MI). One treatment being studied is to deliver a bolus of

autologous MSCs via catheter to the border zone of an MI so that the stem cells might

respond to microenvironmental cues and differentiate into mature myocardium, thus

reducing the infarct size. It is clear that positioning of the cell bolus at the border zone of

the infarct is critical to the success of the repair. Therefore, an image-guided delivery

strategy would be ideal for delivery of cells to the infarct border. The MSN we have

developed are an ideal candidate because they can be detected in 3 imaging modalities:

first, a fluorescent component can be used to visualize the cells in vitro; a second

component allows the cells to be visualized during delivery (in which ultrasound or

angiography techniques are used for rapid, real-time imaging); finally, a gadolinium

oxide component would allow visualization using MRI during follow-up visits.

Approach

To take the project through pre-clinical to clinical stages is far too large a scope

for one dissertation, but I propose to <u>prove the concept of a tissue engineering application</u>

<u>to reduce the damage following myocardial infarction (MI), involving development of</u>

cardiac stem cells as well as a multimodal contrast imaging agent to be used for delivery and monitoring of a stem cell transplant (Figure 2).

Phase 1: Evaluate the proliferative and differentiation capacity of stem cells derived from cardiac and bone marrow sources

Although the general consensus is that precise delivery of stem cells to the border zone of myocardial infarctions can improve patient outcome, there is little agreement at this time on the ideal methods, with respect to the cell type used, whether to use additional chemical stimuli, how long after the infarction to deliver the cells, and other variables. Transplant of autologous MSCs is the most rapid way to deliver large numbers of cells, but it relies on microenvironmental cues to trigger cardiac differentiation at the infarct site. It is well-known in literature, however, that treatment of mesenchymal stem cells with 5-azacytidine, a cytosine analogue and inhibitor of DNA methylation, triggers myocardial differentiation[83-88]. Alternatively, cardiac stem cells can be isolated from fetal sources. These cells are phenotypically the most closely related to mature cardiomyocytes, but have less capacity to divide, so it may be difficult to generate enough cells using this method. Culture of both will be performed to determine the ideal source for stem cell transplant based on the quantity of cells acquired, molecular biology, and electrophysiology.

As described above, no consensus has been established on the ideal conditions needed to culture cardiac progenitor cells. The first step in this project will be to isolate cells from various sources, culture them according to published methods, and evaluate their capacity for cardiac differentiation based on cell yield, electrophysiological activity, and expression of specific proteins measured by immunohistochemistry.

Establish cultures of cells capable of myocardial repair

The cells to be investigated in this step will either be of human or murine origin, and will consist of mesenchymal stem cells isolated from bone marrow aspiration, or cardiac progenitor cells isolated from enzymatic digestion of cardiac tissue. Murine cells will be acquired from sacrificed neonatal mice of collaborating labs, while human fetal cells will be acquired from abortuses; Dr. Assouline is properly credentialed by the IRB to handle human fetal tissues. While bone marrow aspiration is a straightforward process, there are differing protocols for dissociation of cardiac tissue. Some investigators prefer mechanical dissociation (cutting) followed by incubation with type II collagenase[89], which leaves non-collagenous proteins intact, while others use the more potent trypsin enzyme that cleaves all proteins indiscriminately[90]. I will evaluate these methods and choose the one most suited to our needs. Depending on the analysis to be performed, the cells will be cultured in tissue culture plastic or on glass coverslips; each surface will need a unique treatment to promote cell adhesion. The best candidate is likely type I collagen, as this is the primary component of cardiac extracellular matrix[91]. Alternative candidates include polylysine and fibronectin among others. A combination of research and experimentation will be needed to determine the optimal conditions.

Evaluate the stemness of cultured cardiac progenitor cells

After establishing culture conditions of isolated MSCs and cardiomyocytes, I will assess the "stemness" of the cells—whether they are undifferentiated mesenchymal stem cells, partially differentiated cardiac stem cells, or mature cardiomyocytes—by using immunohistochemical markers and electrophysiological signals. Specifically, α-actinin is a striated cytoskeletal protein which is not expressed in the mesenchymal stem cell, but

is expressed amorphously in immature cardiac stem cells and in a parallel pattern in mature cardiomyocytes[83,85,92-94]. Working with members of the cardiology lab (Internal Medicine, University of Iowa) Olha Koval and Yuejin Wu, whole cell patch clamping techniques will be used to measure electrophysiological changes in the cells, which also vary during the differentiation process[83,95,96].

Phase 2: Evaluate the biocompatible and multimodal potential of mesoporous silica nanoparticles in mesenchymal stem cells in vitro.

Ultrasound is a favorable imaging modality for certain applications because of its quick and easy image acquisition and because it does not produce ionizing radiation. In this proof-of-concept, our lab feels precise image-guided delivery to the infarct site is critical to the success of the transplant. Therefore, I wish to place a source of contrast within the cells for precise imaging and delivery. However, current commercially available contrast agents for ultrasound are micron-sized—too large for intracellular delivery. In general, the spatial resolution achieved in ultrasound is not enough to resolve sub-micron sized materials, but some investigators have demonstrated ultrasound contrast using nanoscale materials, such as 330 nm silica nanobeads[41], dextran-coated iron oxide[43], and 50 nm gold nanoparticles[44]. In preliminary data using agarose disc phantoms, we have found our multimodal MSN and europium-doped Gd_2O_3 nanoparticles to be echogenic at biologically significant concentrations using high resolution 30 MHz ultrasound, and we can further improve the signal of the MSN particles by addition of perfluorocarbon moieties to their surface. This additional functionalization should not come at a cost to the other modalities we have already validated (MRI, CT, and fluorescent microscopy); when these particles are completed, we

will test them against the previous generation of particles to look for changes in contrast across all modalities.

In my Master's thesis, I reported on our lab's development of an MSN particle which contains fluorescein isothiocyanate (FITC), a green fluorophore commonly used in fluorescent microscopy, and gadolinium oxide, for MRI contrast enhancement. Subsequently, we have found that these particles are also echogenic under high frequency (20-40 MHz) ultrasound. Using the functionalized nanoparticles provided by the lab, I will further refine and characterize our particle's design to improve upon its ultrasound signal through *in vitro* testing with agar phantoms. The new particles will also be re-tested in MRI and under fluorescent microscopy to ensure that these modalities are unaffected by the modifications.

Perfluorocarbon functionalization of Gd_2O_3-FITC-MSN

A straightforward and repeatable methodology for studying the echogenic effects of our particles begins with *in vitro* image acquisition involving agarose phantoms containing varying concentrations of particles. As described in the product packaging, commercially available Definity® is a perflutren lipid microsphere composed of octafluoropropane encapsulated in an outer lipid shell. The lipid shell is composed of hexadecanoic acid and organic salts. For proper use, Definity® requires activation by warming it to room temperature and shaking for 45 seconds using a Vialmix® device. Once mixed, 1 milliliter of Definity® contains about $1.2*10^{10}$ lipid microspheres and 1.1 mg octafluoropropane. After activation and intravenous injection, Definity® provides contrast enhancement of the endocardial borders during echocardiography.

Our preliminary data indicates that in agar, Definity® nearly saturates the transducer with maximum signal even at very low concentrations, but for biologically relevant concentrations, our current MSN particles produce nearly as intense a signal in these phantoms as Definity®. Based on these findings, we plan to develop new MSN particles, covalently bound with "nano-bubbles" of high molecular weight gas (perfluorocarbon) to further improve the signal. These particles (CF_3-Gd_2O_3-FITC-MSN) represent an improvement over the first generation of MSN particles.

The protocol used by chemists in our lab to synthesize the particles follows. The perfluorocarbon is covalently grafted onto the MSN surface using a straightforward method. MSNs containing gadolinium oxide and FITC, synthesized using previously reported methods[81,97], are refluxed with trimethoxy (3,3,3-trifluoropropyl) silane in toluene at 110°C for 2 hours. The particles are washed in methanol, then deionized water, and dried, at which point they can be resuspended in balanced salt solutions. The biocompatibility of this modification will be assessed by adding the particles to the MSCs described in specific aim 1 at a concentration of 125 µg/mL, and noting the change in cell viability relative to those labeled with unmodified MSNs as well as untreated cells.

Characterization of particles in ultrasound and magnetic resonance imaging

Synthesized F_3-Gd_2O_3-FITC-MSN will be mixed in various concentrations with 1.5% agar, poured in 60 mm Petri dishes, and allowed to set. At the ultrasound scanner, the agars will be carefully removed from the Petri dish to eliminate it as a source of image artifact, and scanned between layers of ultrasound gel at 40 MHz. Additional agars will be poured into 0.5 mL Eppendorf tubes and scanned in the 4.7 T Varian® small animal MRI scanner, using a T2*-weighted scanning strategy.

Acquired images will be analyzed using a combination of ImageJ and MIPAV to obtain relative grayscale intensity and volumetric information. Statistical comparisons will be made using the t-test for comparison of two means with independent samples and unequal variances:

$$t = \frac{(\bar{x}_1 - \bar{x}_2) - (\mu_1 - \mu_2)}{\sqrt{(s_1^2/n_1) + (s_2^2/n_2)}}; \quad \nu = \frac{\left[\frac{s_1^2}{n_1} + \frac{s_2^2}{n_2}\right]^2}{\left[\frac{(s_1^2/n_1)^2}{n_1 - 1} + \frac{(s_2^2/n_2)^2}{n_2 - 1}\right]}.$$

where n_1 and n_2 are the number of voxels in each VOI, s_1^2 and s_2^2 are their respective standard deviations, $\bar{x}_1$ and $\bar{x}_2$ are their means and ν is the degrees of freedom used in reference to the statistical lookup table.

Phase 3: Validate the nanoparticle system as a tool for stem cell tracking in myocardial infarction using animal models

In order to demonstrate proof-of-concept using our particles as tracing agents for stem cells, we have discussed murine models for MI with the lab of Dr. Robert Weiss. Their murine model involving coronary artery ligation is well-established[98-101]. However, we wish to demonstrate measurable reduction of MI size through the image-guided delivery of myocardial stem cells directly into the myocardial wall using minimally invasive techniques, such as catheterization. In a mouse, where the wall of the myocardium and most arteries are less than 1 mm across, it may not be possible to deliver the cells in this manner. To scale this experiment to a larger animal and gain ACURF approval will be a lengthy and expensive process. Therefore, to demonstrate the concept, I will complete the intermediate step of performing experiments on *ex-vivo* mouse heart phantoms.

<u>Fluorescent labeling of cardiac stem cells with modified mesoporous silica nanoparticles</u>

The first step in the proof-of-concept is to show that these cardiac progenitor cells can be labeled with MSN. Preliminary experiments, including those comprising my Master's thesis, show that MSCs readily take in MSN with little effect on cell metabolism or viability. An important consideration in these experiments is the balance between having enough cells labeled (efficiency) and having good cell viability. If necessary, some efficiency can be sacrificed to improve viability, if it can also be shown through another method, such as histopathology, that labeled and non-labeled cells have the same fate *in situ*. In this experiment, the cells cultured in specific aim 1 will be combined with the new MSN produced in specific aim 2. The labeling efficiency will be assessed using fluorescent microscopy and/or flow cytometry, while cell viability of labeled and non-labeled cells will be measured using a fluorescent plate reader and the commonly used MTT assay.

<u>Evaluation of tissue phantoms for ultrasound and magnetic resonance imaging</u>

While structurally simpler, agar has similar acoustic properties as most soft tissue[102-104]; therefore, a repeatable tissue analog will be created by embedding *ex-vivo* mouse heart in agar. This will provide an optically clear needle path with which to practice image-guided techniques. Using this method, labeled cells will be injected into the heart while the 40 MHz ultrasound signal arising from both the needle and the cells is recorded. Thus I will be able to demonstrate real-time detection of an image-guided delivery of labeled cells. Similarly, the heart injected with labeled cells will then be placed in the 4.7 T Varian® small animal MRI scanner and scanned using T1- or T2*-weighted strategies to demonstrate the feasibility of post-op follow ups using the same

MSN particles. These studies will provide our lab with the necessary data allowing us to proceed to larger animal models in which this can be done *in vivo*.
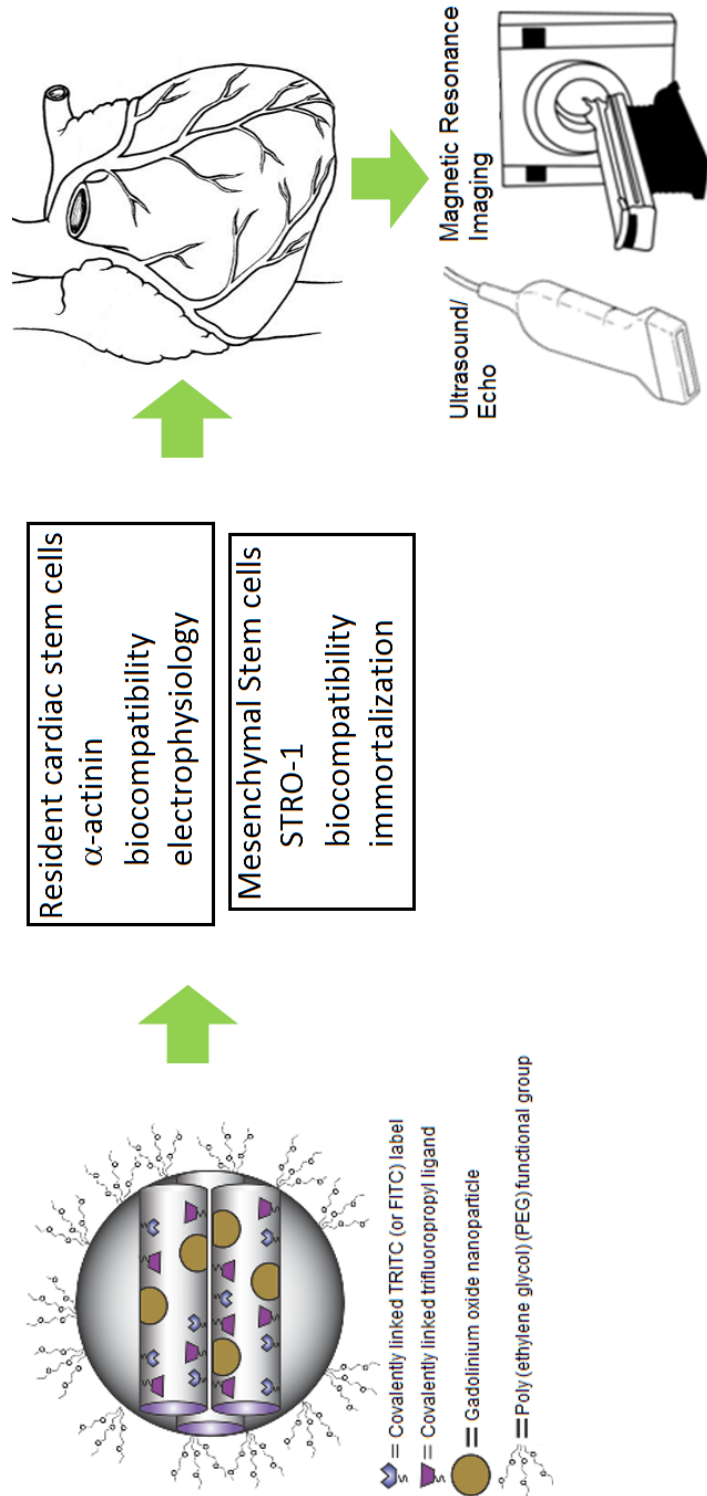
Figure 2. Illustration depicting the overall approach for this project.

CHAPTER 2: EVALUATION OF THE PROLIFERATIVE AND DIFFERENTIAL CAPACITY OF ISOLATED CARDIAC CELLS

Introduction

As discussed in Chapter 1, the research community has not yet arrived at a consensus with respect to the optimal transplant conditions to repair a myocardial infarct (MI), though it is known that mature cardiomyocytes have very little capacity for regeneration. A great deal of research has been undertaken to characterize the various cell types used in cardiac regeneration. Like all cell types, cardiac progenitors can be evaluated by their expression of cell surface markers, identified through immunohistochemical staining techniques. However, cardiac cells in culture also have the capacity to spontaneously contract, thus providing the investigator with the opportunity to evaluate the cells based on electrophysiological measurements as well. In this chapter, I discuss the scientific literature as it stands with respect to electrophysiological and immunohistochemical characterization of cardiac progenitors. Then, in order to address phase 1 of my project, I carry out cultures and characterization of the same cells in our lab. Not only is this necessary to establish a population of cells for subsequent experiments, but it ensures that the cells grown in our lab are consistent with those of other labs and are grown in a reliable, reproducible manner.

Immunohistochemical characterization of cardiac progenitors

When approaching any tissue engineering problem, understanding the embryogenesis of a tissue/organ is key to understanding how to go about repairing it, and when discussing the development of the heart, one of the most critical molecules to understand is Islet-1 (ISL1). The review "Multipotent Islet-1 cardiovascular progenitors

in development and disease" by Nakano, et al, discusses in great detail the involvement of this molecule in the development in the heart[105]. Briefly, the earliest cardiac precursors are part of the primitive streak shortly after gastrulation, with endocardial tubes contained within a pair of cardiac crescents forming shortly thereafter. This region has been named the primary heart field, or first heart field upon discovery of a secondary heart field (SHF) in the dorsomedial mesoderm adjacent to the crescents. Islet-1 was subsequently found to be a strong identifier of the entire SHF, while other markers such as FGF8/10, Wnt11, and a specific Mef2c enhancer identify the anterior subset of the SHF, which eventually becomes the outflow tracts (ventricles and arteries) in the mature heart[105,106]. The posterior subset of the SHF contributes to the atria and inflow tracts, and the primary heart field mainly contributes to the myocardium of the left ventricle. Garry and Olson characterize a subset of embryonic progenitor cell, the cardiovascular colony-forming cell (CV-CFC), which is positive for a marker called Brachyury (Bry) and later Flk, also known as Kdr[107]. The Flk$^+$/Bry$^+$ cell is capable of giving rise to all subsets of cells in the primitive heart as well as blood cells (Figure 3).
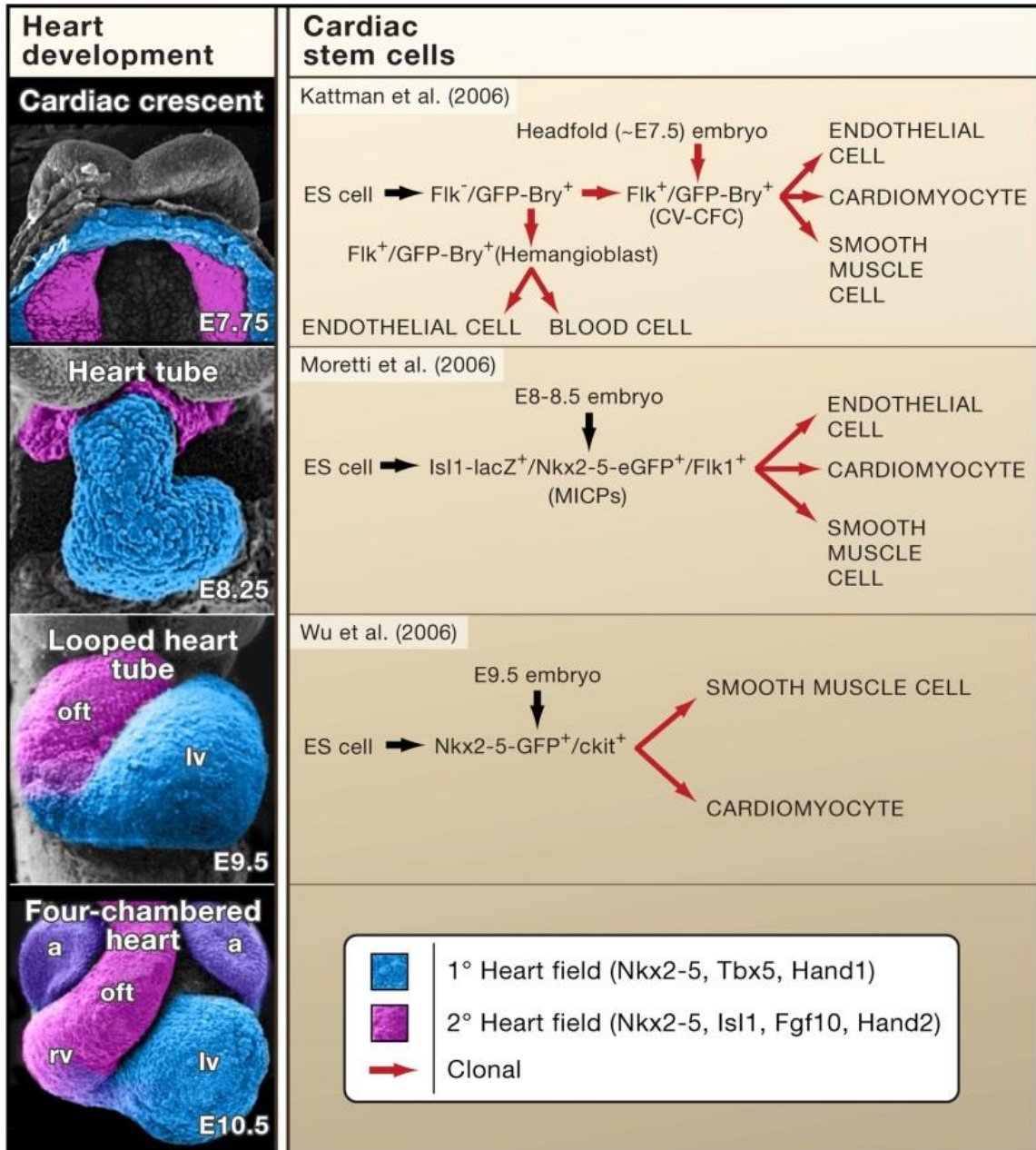
Figure 3. False-color SEM of developing mouse heart indicating primary and secondary heart fields from 7.5 to 9.5 days gestation. The right column indicates potential markers of various intermediate cell types. Reproduced from Garry and Olson[107].

Islet-1 is a transcription factor in the LIM homeodomain family, and its expression is observed in mouse embryos of day 7.5-9.5, and has been observed from 11 to 18 weeks in the human fetus. Using antibodies for immunostaining, cells positively expressed ISL1 in the walls of both atria, the superior vena cava, aorta and pulmonary artery at 11 weeks' gestation. By 18 weeks, expression is reduced considerably, with ISL1^{+} cells being retained in small clusters in the right atrium. Cells positive for ISL1 showed a nuclear pattern of expression[107].

In another example from literature, Moretti et al first isolated cardiomyocytes from 1-5 day-old mouse pups which were double heterozygous for Isl1-mER-Cre-mER and R26R. After administering an intraperitoneal injection of tamoxifen to the pregnant mothers, the pup cardiomyocytes expressing ISL1 at the time of tamoxifen exposure have detectable β-galactosidase (β-gal) activity, particularly in the sinoatrial node and outflow tract, as shown by immunohistochemistry. Cardiomyocytes were also dissociated by exposure to 0.5 mg/mL trypsin overnight at 4°C, followed by 40 minutes total in type II collagenase at 37°C. Progenitor cells positive for β-gal were preferentially attached to culture plastic using DMEM/M199 in a 4:1 ratio, with 10% horse serum/5% fetal bovine serum, and two rounds of removing non-adherent, β-gal^{-} cells after one hour[108]. These cells were given another dose of tamoxifen (1 μM) one day after plating and maintained in culture thereafter (method fully described by Laugwitz et al[109]).

In culture, these dissociated ISL1^{+} cardiac precursors were shown to contribute to populations of both endothelial (ECs) and smooth muscle cells (SMCs), using VE-cadherin and smooth muscle myosin heavy chain, respectively. Further investigation confirmed that, regardless of the presence or absence of a feeder layer, some of the ISL1^{+}

cells spontaneously matured into SMCs, while others did not[110]. The mature SMCs

responded to an angiotensin stiumuli by increasing their Ca^{2+} permeability compared to

non-SMC phenotypes (Figure 4).
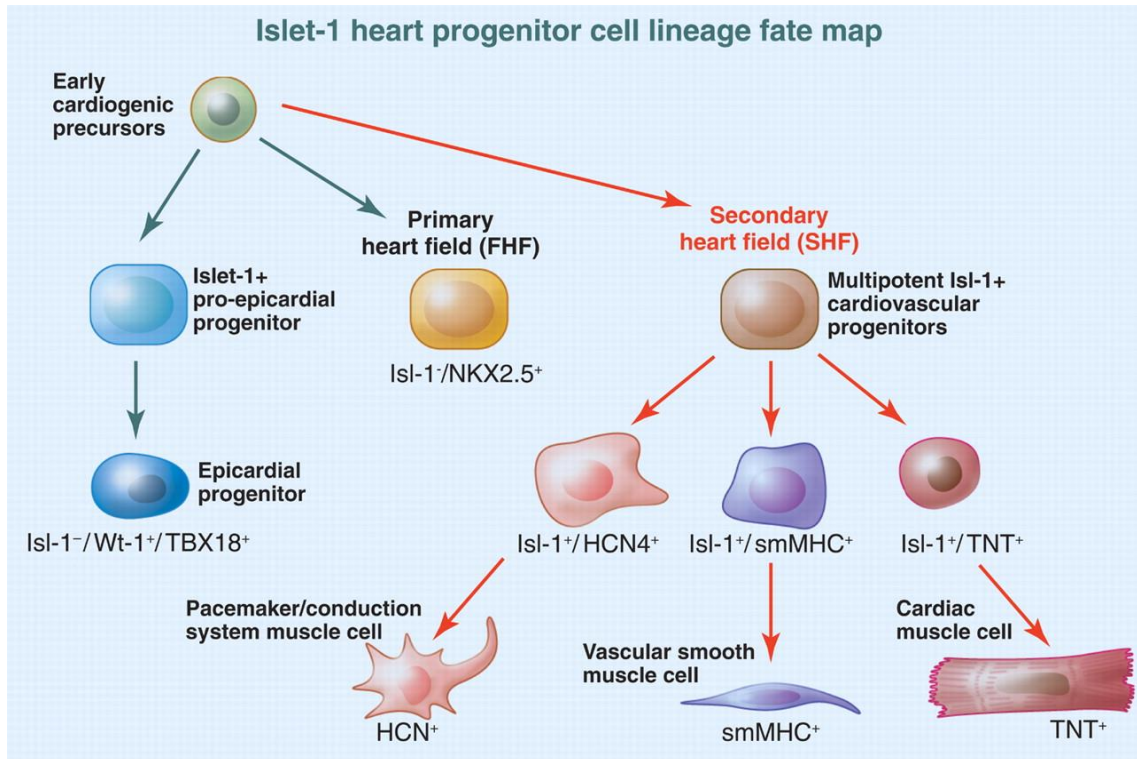
Figure 4. Summary of lineages of the resident cardiac stem cells, including specific markers of each cell type. Note the markers that are in common with those of the developing heart (ISL1, Nkx2.5), and the presence of an ISL1+ cell capable of giving rise to all 3 major tissues of the heart: pacemaker cell, vascular smooth muscle cell, and mature cardiomyocyte (reproduced from Chien, et al[110]).

In addition to ISL1, another critical protein often used to identify progenitor and mature cardiomyocytes is the muscle filament α-actinin. In non-muscle cells, α-actinin acts to anchor cytoskeletal proteins (i.e., microfilaments) to the cell membrane[111-113]. In muscle cells, α-actinin anchors actin filaments to the Z-disc, providing a stationary platform against which myosin filaments exert force and slide past during muscle contraction[114-116]. As a result of its involvement in this process, α-actinin is commonly used as a target for immunohistochemical analysis of muscle cells[93,94,117-119]. In cardiac progenitors, actin-myosin filaments are present, as confirmed by the capacity of the cells to spontaneously contract in culture. However, the cell and filaments within are irregularly shaped, thus the α-actinin staining takes on an amorphous pattern[94]. In mature cardiomyocytes, the cell is essentially rectangular, and the muscle filaments are all arranged with the same orientation to ensure maximum efficiency in contraction[93,117].

Based on lengthy reviews of the literature, ISL1 and α-actinin appear to be optimal candidates for immunohistochemical staining. Both give clear indications as to what stage of differentiation the respective cells are currently in. In preliminary trials with ISL1, results confirmed those of literature, in that ISL1 expression drops off considerably after early fetal development. Therefore, I chose to use α-actinin as the optimal candidate for determining cardiac cell phenotype immunohistochemically. However, a more straightforward method to visualize cardiac differentiated cells is to simply observe spontaneous contraction *in vitro*, or to measure action potentials.

Electrophysiological properties of cardiac progenitors

The contraction of a heart is the result of countless molecular contractions between actin and myosin filaments, they themselves the result of flows of ions through

transmembrane channels, generating a measureable electric current[120]. Starting in the

sinoatrial (SA) node, also known as the pacemaker, a membrane potential of about -40

mV causes the opening of T-type voltage-gated calcium channels, generating an inward

Ca^{2+} current and rapid depolarization of the cell membrane to about +10 mV. During

repolarization, the T-type voltage-gated calcium channels close and voltage-gated

potassium channels open. The outward K^+ current exceeds the inward Ca^{2+} current and

the membrane voltage decreases to about -60 mV. Next, pacemaker sodium channels

open, slowly depolarizing the cell with inward Na^+ current until it reaches the threshold

for the T-type voltage-gated calcium channels to reopen, beginning the next action

potential[120]. As oxygen demands in the body change, heart rate is altered by

neurotransmitters that alter the inward Na^+ current: the sympathetic nervous system

releases norepinephrine which stimulates β1 receptors to increase inward Na^+ current,

shortening depolarization time and increasing heart rate; conversely the parasympathetic

nervous system releases acetylcholine which stimulates muscarinic receptors to decrease

the inward Na^+ current, slowing depolarization and reducing heart rate[121].

The SA node action potential propagates quickly through fibrous bundles of

modified myocardium, connected by gap junctions, to cause the atria to contract first.

When the action potential reaches the atrioventricular (AV) node, a reduction in

conductivity slows it somewhat, allowing the ventricles to fill, before rapidly propagating

again via the bundle of His. Purkinje fibers branch around the ventricular myocardium,

ensuring a well-coordinated and efficient contraction of the ventricles[120].

The action potential of ventricular cells differs considerably from that of the nodal

and atrial cells, starting with a resting membrane potential of about -90 mV. Rectifier

potassium channels are open at rest, close during the depolarization phase and reopen during repolarization. The incoming action potential activates voltage gated sodium channels and the inward Na^+ current depolarizes the membrane to about +10 mV. Initial repolarization occurs when voltage-gated Na^+ channels close and rectifier K^+ channels open, creating a net outflow of K^+ ions, and a membrane potential near zero. Here, L-type voltage-gated Ca^{2+} channels open, creating an inward Ca^{2+} current that balances the outward K^+ current, briefly plateauing the membrane potential. Repolarization resumes when inward Ca^{2+} current induces the release of additional Ca^{2+} from the sarcoplasmic reticulum. The L-type voltage-gated Ca^{2+} channels close, additional K^+ channels open, and the membrane becomes fully repolarized to its resting potential[120].

Thus, in addition to using immunohistochemistry to identify cell surface markers (i.e., ion channels) in cardiomyocytes, they can also be identified by their electrophysiological properties. If the action potential has a relatively high resting potential and a fast repolarization phase without a plateau, it is closer to a nodal or atrial cell, while cells that have action potentials with low resting potentials and plateaus in the middle of the repolarization phase, they are more closely related to ventricular cells.

Although cultures of dissociated neonatal mouse ventricles have yielded successful results in literature including spontaneously contracting cells[122-124], results using human fetal hearts as a tissue source have been mixed. Two features of cultures that vary are the enzymes used to dissociate the heart, and the surface on which the cells are grown. In literature, there are very few studies in which spontaneously contracting human fetal cardiomyocytes are cultured. Mummery et al isolated human fetal cardiomyocytes in cell culture for immunohistochemical, and electrophysiological

comparison with cultured human embryonic stem cells[125]. In papers describing murine cardiomyocyte cell culture, a popular plate of choice is the Mat-Tek® plate, a 35 mm dish with a 12 mm Type I collagen-coated glass coverslip in a shallow well at the center. The cardiovascular lab with whom we collaborate elects to coat their Mat-Tek® plates in 200 µL fibronectin for 1 hour prior to culture. Mummery, et al (2002) states that fetal cardiomyocytes were cultured directly on glass coverslips. The following method is based on those seen in literature and provided to us by collaborators, with some variable treatments to the dishes tested to determine optimal adhesion and growth.

Methods

Isolation and immunohistochemistry of murine and human fetal cardiomyocytes

The heart of a human fetal abortus (15 weeks gestation as measured by foot length) was collected in cold PBS and transported to the lab for dissection within approximately 5 hours of the elective abortion. The use of discarded human fetal tissue for biomedical research application was reviewed and approved by the University of Iowa Institutional Review Board (IRB # 199008391; continuously approved from September 22, 2005 – August 31, 2015). Similarly, hearts of adult mice were excised immediately following sacrifice. All hearts were cut in half approximately along the mid-frontal plane, dividing the heart into anterior and posterior halves both containing tissue from all 4 chambers. From the anterior portion, small pieces of tissue were set aside for later RNA/protein analyses. The posterior portion was placed in 4% paraformaldehyde (PFA) at 4°C overnight, then moved to a sucrose gradient (first stage, a 2:1 ratio of 0.16 M sucrose in PBS and 4% PFA; second stage, a 4:1 ratio of 0.32 M sucrose in PBS and 4%

PFA; third stage, 0.5 M sucrose in PBS) for 4 days at 4°C. The tissue was then embedded in OCT medium and stored at -80°C until 8 μm-thick cryosections were made.

The 8 μm sections were mounted on slides and stored at -20°C until labeling. One mid-frontal slide contained 2 sections and was stained with H&E. In addition, isolated cardiomyocytes were cultured on 12 mm round glass coverslips coated with fibronectin, using the same methods for isolation and culture as the cells grown on tissue culture plastic. The primary antibody mouse-anti-α-actinin, an IgG2b class antibody, was obtained. A slide containing adjacent sections to the H&E-stained sections were selected, and given 100 μL of a blocking compound containing 3% fish gelatin and 0.75% Triton X-100. This was left on the sections for 30 minutes. Based on the validation results, 200 μL each of concentrations of 1.5 and 5 μg/mL were prepared for use as primary antibodies on 2 of the sections. The third section on the slide was given Sedi-Stain for comparison. The 2 concentrations of primary antibodies were added and left overnight at 4°C to allow full penetration into the tissue. The secondary antibody, donkey-anti-mouse IgG-488 was used at a concentration of 1:1000, and left on the sections for 90 minutes. Between each stage of staining, 3 sets of 5 minute rinses in PBS were performed.

About 200 μL Vectashield® mounting medium containing To-Pro® nuclear stain was used on the slide, to which a coverslip added. Clear nail polish was used to seal the slide, which upon curing was immediately taken for fluorescence microscopy. Several images were taken, followed by wrapping the slide in aluminum foil and storing it at -20°C for two days until confocal microscopy could be done. Several images and 2 50 slice Z-stacks were done at regions of interest using the FITC narrow band filter set.

Electrophysiological identification of cultured cardiomyocytes

The heart from a human fetal specimen of 16 weeks' gestation was collected, stored in a 15 mL tube containing 5 mL DMEM/10% fbs and transported to the lab as quickly as possible. The use of discarded human fetal tissue for biomedical research application was reviewed and approved by the University of Iowa Institutional Review Board (IRB # 199008391; continuously approved from September 22, 2005 – August 31, 2015). After using ethanol-sterilized forceps to tease away the pericardium and epicardium as much as possible, the left ventricle (LV) and right atrium (RA) were identified and dissected from the rest of the heart. The LV and RA were minced separately using a scalpel until pieces were smaller than 1 mm, then immersed in Eppendorf tubes containing collagenase at an approximate ratio of 3 parts collagenase for every one part tissue. The tubes were incubated at 37°C for about 40 minutes, then passed about 20 times through a 1 mL pipet tip in which the final few millimeters of the tip were cut off to make it wider. The tissues were returned to the incubator for about 20 more minutes, then passed 20 times through an uncut pipet tip. Finally, the cells were centrifuged for 5 minutes at 1000 RPM to remove the collagenase, the pellet was resuspended in about 6 mL DMEM/F12 medium containing 10% serum, and placed in an untreated 100 mm dish for 5 hours of preplating, designed to purify the culture of any remaining fibroblasts. During the preplating period, a 6 well plate was prepared with varying surface treatments (Table 3).

Table 3. Surface treatments for the culture of isolated cardiomyocytes

	Collagen (5 hour wet treatment)	Collagen (1 hour wet, 4 hour dry treatment)	Collagen (wet treatment) + Fibronectin
Right Atrium	Well A-1	Well A-2	Well A-3
Left Ventricle	Well B-1	Well B-2	Well B-3

For wet collagen, a preparation of 10 mL collagen in acetic acid, 2 mL DMEM/10%, and sufficient 1N NaOH to neutralize the pH was added to the wells and left for the entire 5 hour preplating period. For dry collagen, this same mixture was left on the wells for 1 hour, then removed so the wells could dry for the final 4 hours. For the collagen/fibronectin wells, collagen was added for 4 hours, then the excess was removed and the wells were coated with fibronectin for the final hour. A fourth condition of a 1 hour fibronectin treatment was done on one 35 mm Petri dish. All the surfaces were very gently rinsed with PBS immediately prior to final plating. From the preplating dish, the unbound cells were collected and split evenly among the wells: the RA was split into thirds on the 6 well plate, and the LV was split into fourths on the 6 well plate as well as the fibronectin-treated 35 mm dish.

These cells were left undisturbed in the incubator for 3.5 days *in vitro* then given a half-medium change of fresh DMEM/F12/10% serum, micrographs were taken of each condition, and contracting cells were observed only in the collagen/fibronectin wells of both LV and RA. Three days later, contractions were still observed only in the LV well. The regions of contracting cells were marked on the bottom of the well with a Sharpie marker and contractions recorded with a cell phone camcorder. The specimen was transported to the lab of our colleagues, where at 10 days in vitro, electrophysiological recordings were made on the marked contracting cells (Olha Koval and Yuejin Wu). Whole cell patch clamp techniques were used, in which the glass electrode is attached to the cell, and suction is applied to make a small hole in the membrane, giving the electrode access to the cytoplasm, where intracellular voltage is recorded with respect to the reference electrode. For the duration of the study, the cells are bathed in a balanced salt

solution. The recordings were provided to me for analysis, for which several parameters (upstroke velocity, overshoot, amplitude, resting potential, and frequency) were measured.

Results

Colonies of fibroblast-like cells were identified and average colony diameter was used to quantify cell growth. One day after plating, the right atrial and left ventricular cell suspensions on the different tissue culture plastic treatments, little difference is observed between the cultures (Figure 5), though the initial plating density appears to be slightly higher for the ventricular cells. This is simply a function of starting with more ventricular tissue than atrial tissue, because of their relative size differences. When dissociating and plating fresh tissues, a number of large, multicellular tissues would indicate insufficient dissociation, while an excessive amount of cell debris would indicate excessive dissociation; here the majority of the cells are observed as individual or small groups of cells, and debris is minimal, indicating a proper dissociation. Initially there does not seem to be a significant difference in adhesion or cell morphology between the culture surface treatments, and spontaneous contraction is not observed in any of the cells.

After 2-3 days *in vitro*, the cells plated on collagen had become detached from the matrix, and in some wells, the collagen surface itself had detached from the surface of the well. Observation of the cells continued, though after the majority rejected the collagen surface, only a sparse few cells remained attached and neither carried out mitosis nor began spontaneous contraction. Thus, the remaining data was observed in fibronectin-treated and untreated dishes.

Right Atrium, Collagen-Treated	Left Ventricle, Collagen-Treated
Right Atrium, Fibronectin-treated	Left Ventricle, Fibronectin-treated
Right Atrium, untreated	Left Ventricle, untreated

Figure 5. Human fetal cardiomyocytes, isolated from right atrium or left ventricle as indicated, 24 hours after plating on untreated tissue culture plastic, or treated with collagen or fibronectin. Scale bars represent 50 μm.

From 4-10 days *in vitro*, a greater difference is observed between cells cultured on fibronectin and those cultured on untreated plastic (Figure 6). The cells grown on fibronectin grow faster, and in a more consistent monolayer across the dish, while the cells grown on untreated plastic form small colonies distinct from one another. Beginning at 4 days *in vitro*, colonies of up to 10 spontaneously contracting cells are observed scattered in the fibronectin-treated wells; the colonies are not interconnected, however, and contractions are independent of one another, occurring at different frequencies. In addition, several 3-dimensional spheroidal bodies of differing sizes, from a few tens of microns to nearly 1 mm in diameter, grow in the fibronectin-treated wells. Examples of these can be seen in the figures (Figure 6, asterisks); some of these bodies undergo spontaneous contraction as well. Though the microscope and camera used did not possess the capacity for shooting video directly, short videos of the spontaneous contractions were acquired by directing a handheld camera at the computer monitor while it was showing a live preview of the microscope.

RA, 4 days in vitro (Fibronectin)	RA, 4 days in vitro (untreated)
RA, 6 days in vitro (Fibronectin)	RA, 6 days in vitro (untreated)
RA, 10 days in vitro (Fibronectin)	RA, 10 days in vitro (untreated)

Figure 6. Human RA specimens 4-10 days after plating on untreated tissue culture plastic, or treated with collagen or fibronectin. Scale bars represent 50 μm (*-large spheroid cell masses observed beginning day 6).

Much like the RA cells, from 4-10 days *in vitro*, the LV cells began to present a different morphology in the fibronectin-treated wells relative to the untreated wells (Figure 7). Unlike the RA cells, however, the LV cells did not continue growing to form a monolayer, regardless of surface treatment. In the untreated wells, the cell density reached a peak at 4 days *in vitro*; by 6-10 days, the numbers had declined and the cells that remained had taken on more of a fibroblast-like morphology, suggesting that the initial prep may have contained traces of pericardium or epicardium, both sources of fibroblasts which grow rapidly in culture. In comparison, the fibronectin-treated wells grew well until 6 days *in vitro*, forming dense colonies as shown in the figure; however, these ultimately degraded again by 10 days *in vitro*.

The poor growth of LV tissue relative to RA tissue is not surprising, given that even in very young hearts, the ventricles are already contracting at a highly efficient rate to circulate blood. By definition, the ventricles must be made largely of mature cardiomyocytes with a low capacity for cell division/differentiation *in vitro*.

LV, 4 days in vitro (Fibronectin)	LV, 4 days in vitro (Untreated)
LV, 6 days in vitro (Fibronectin)	LV, 6 days in vitro (Untreated)
LV, 10 days in vitro (Fibronectin)	LV, 10 days in vitro (Untreated)

Figure 7. Human LV specimens 4-10 days after plating on untreated tissue culture plastic, or treated with collagen or fibronectin. Scale bars represent 50 μm (*-large spheroid cell masses observed beginning day 6).

Staining isolated cardiomyocytes for α-actinin showed morphologies consistent with published works[118,119]. Left ventricular cells showed striations, all aligned perpendicularly to the length of the cell, much like fully formed cardiomyoctes (Figure 8A-B). As previously indicated, α-actinin anchors the actin filaments to the Z-band of the sarcomere; thus, the distance between striations in α-actinin staining gives the sarcomere length. Using ImageJ to measure the striations in the micrographs, the sarcomere length of 2 μm is consistent with published results[126].

Unlike the left ventricular cells, the right atrial cells have a much more "stem-like" morphology, with filaments following the contours of the cell, rather than aligning in a parallel fashion (Figure 8C-D). This, too, is consistent with published works. Examples of varying expression are shown. In one panel, two largely bipolar cells have α-actinin expression along filaments of the cytoskeleton (Figure 8C). The nucleus of one cell is visible, while the other is obstructed somewhat by non-specific binding. The digital merging of the two fluorophores (green FITC and red To-Pro) is less balanced than the second panel, in which the red nuclei are more visible (Figure 8D). In this panel, one stellate cell has well-resolved α-actinin staining as well as non-specific binding. A second adjacent cell contains almost no α-actinin staining. Based on its broad shape and large nuclear-to-cytoplasmic ratio, this cell appears to have been non-viable prior to the staining procedure.
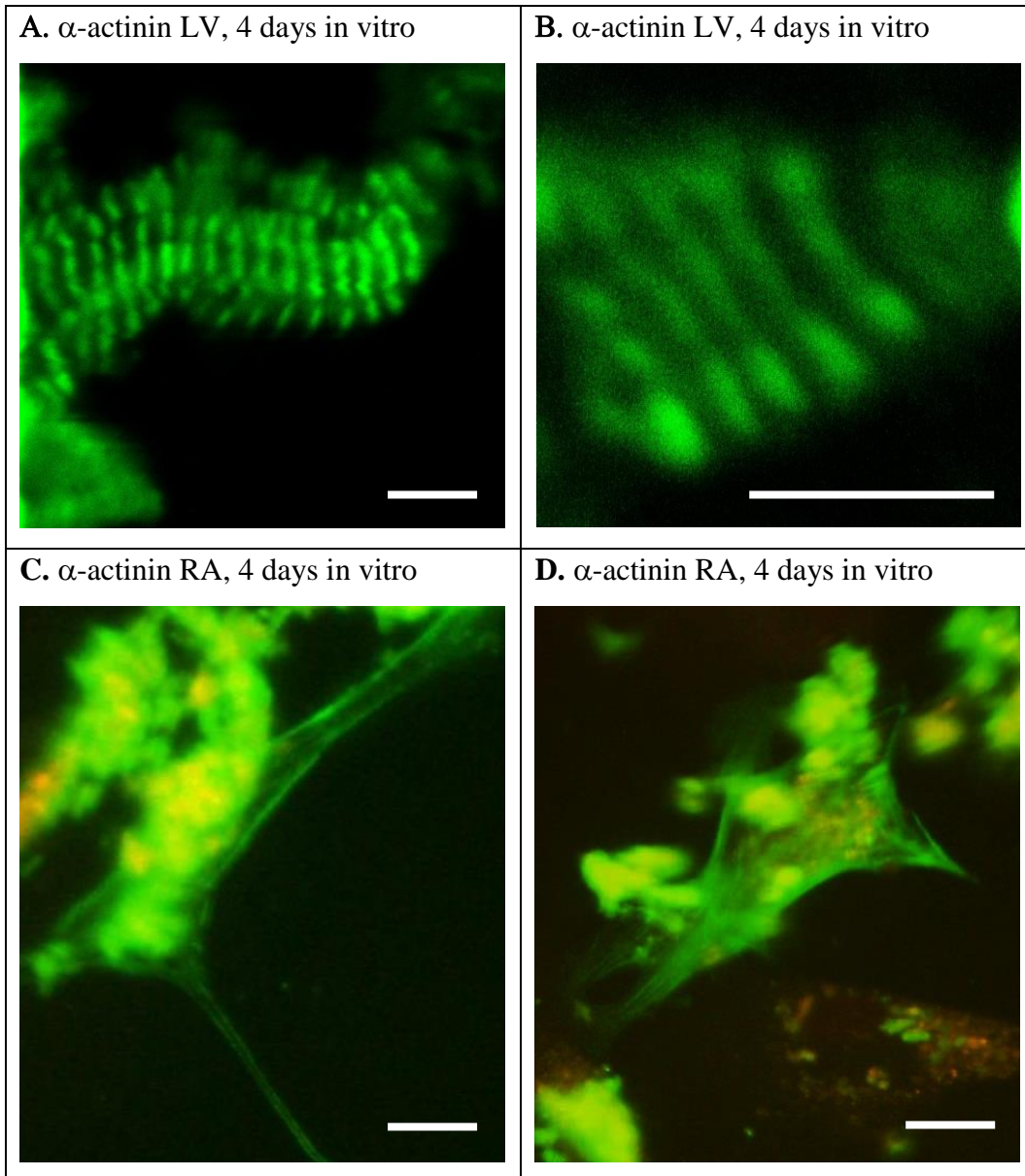
Figure 8. α-actinin immunolabeling. Human cardiomyocytes, 4 days after plating on glass coverslips treated with fibronectin. (A, B) Low (A) and high (B) magnification of left ventricular cells. (C,D) Right atrial cells. Primary antibody: mouse anti-α-actinin; secondary antibody: goat-anti-mouse IgG FITC (green); To-Pro nuclear stain (red). Scale bars represent 10 mm.

After 10 days *in vitro*, the cells cultured as shown (Figure 6-7) were gently removed from the tissue culture plastic using EDTA and transferred to glass coverslips within wells of tissue culture clusters for electrophysiology. Again, multiple surface treatments were employed: "wet" collagen, in which the collagen was applied to the glass and immediately immersed in growth medium without drying; "dry" collagen, in which the coverslips were coated in collagen for 1 hour, then allowed to air dry for 4 hours; and a mixture of 4 hours "wet" collagen treatment followed by 1 hour fibronectin treatment (Figure 9). Like the first passage, this subculture of cells was separated by left ventricular and right atrial cells; here, the majority of the atrial cells formed monolayers, while many of the ventricular cells form microspheres. Spontaneously contracting cells are observed in both atrial and ventricular cultures and in all surface treatments (Figure 9, asterisks). The largest proportion of contracting cells, as well as the cells with the best binding to the coverslips is of the collagen/fibronectin treatment. Therefore these cells are used for the subsequent patch clamping experiment.
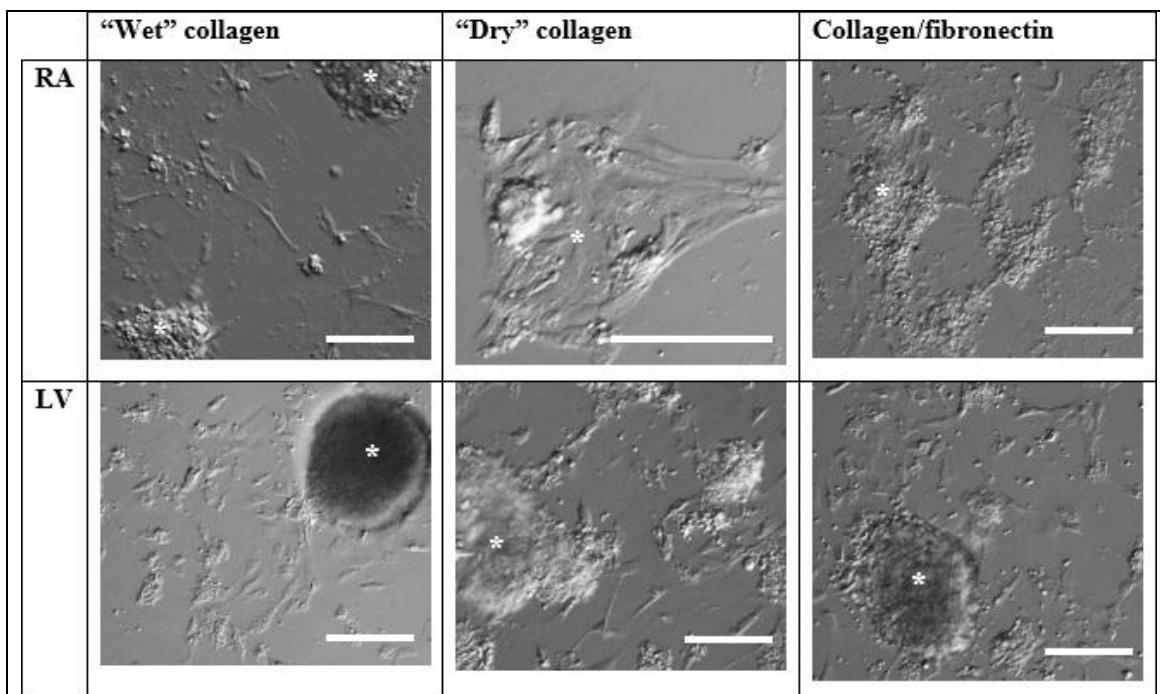
Figure 9. Isolation of human fetal cardiomyocytes on various glass coverslip surface treatments prior to patch clamping. Using the same treatments as shown in Table 3, cells of the right atrium (RA) and left ventricle (LV) were transferred to glass coverslips on day 10 *in vitro* for whole cell patch clamping. Spontaneous contractions were observed in clusters of cells in each well (indicated by asterisks). The cells were most strongly adherent to the collagen/fibronectin treatment; therefore, these were the cells analyzed by patch clamp. Scale bars represent 50 μm.

Three sets of representative electrophysiological recordings are shown (Figure 10) in addition to calculated values for these recordings (Table 4), compared with published values for similarly prepared cells[125]. The upstroke velocity, defined as the average slope of the depolarization phase, was calculated to be 22.6, 16.6, and 2.3 V/s for figure 10A, B, and C, respectively. By comparison, values published by Mummery et al range from 2.6 to 8.9 V/s average velocity, with maximum velocities of 20.0 and 26.7 V/s for ventricular cells. The overshoot, defined as the maximum voltage at the end of depolarization, was 37.3, 19.6, and 38.7 mV for figure 10A, B, and C, respectively. By comparison, the published values range from 16.6 to 26 mV. The amplitude, defined as the voltage difference between maximum hyperpolarization and the maximum at depolarization phase, was 109, 86.3, and 90.8 mV for figure 10A, B, and C, respectively. Published values range from 32.0 to 80.0 mV. The resting potential, i.e., the average voltage between the end of one repolarization phase and the beginning of the next depolarization, was -71.7, -66.7, and -52.1 mV for figure 10A, B, and C, respectively. Published values range from -48.0 to -20.8. Lastly, the frequency, or the inverse of the time between subsequent depolarizations, is 1.58, 3.26, and 0.731 Hz, for Figure 10A, B, and C, respectively. Published values range from 0.6 to 1.5 Hz.

A. Ventricular cell **B. Atrial cell** **C. Isolated Ca2+ current**
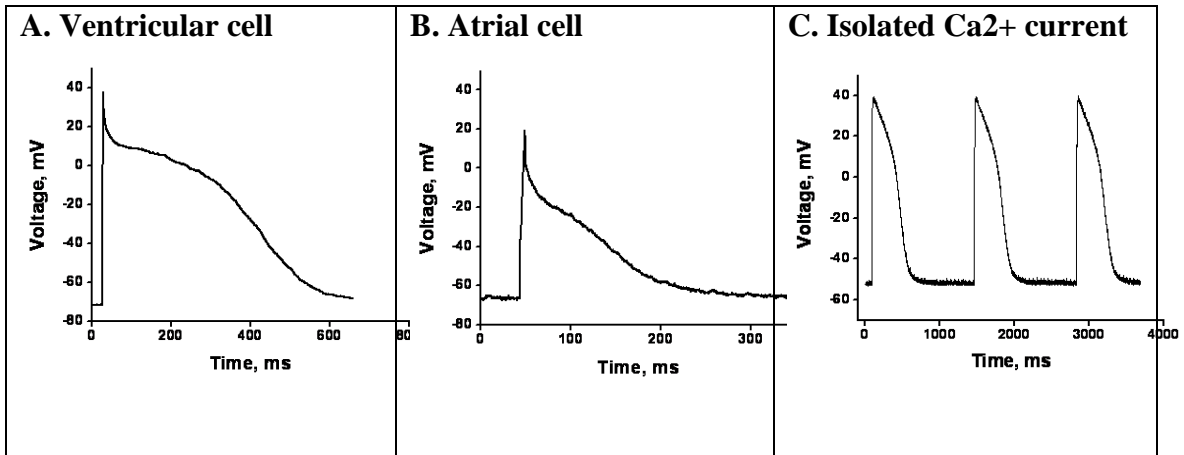
Figure 10. Action potentials recorded on 3 different regions of spontaneously contracting cardiomyocytes. Isolated cardiomyocytes were grown on collagen/fibronectin tissue culture plastic for 10 days, then transferred to collagen/fibronectin-coated glass coverslips prior to patch clamping. (A) With a faster depolarization and longer plateau phase, this is characteristic of a ventricular cell. (B) With a slower depolarization and little to no plateau, this is characteristic of an atrial cell. (C) With a resting potential of -50 mV, this action potential was determined to be characteristic of an isolated Ca2+ channel, rather than a whole cell patch clamp.

Table 4. Key measures of action potentials of human fetal cardiomyocytes,

compared with published values for fetal and human embryonic stem (hES) cells[125].

	n	Upstroke Velocity (V/s)	Overshoot (mV)	Amplitude (mV)	Resting Potential (mV)	Frequency (Hz)
Pacemaker hES cells[125]	1	2.6	18.0	32.0	-20.8	1.2
Atrium-like hES cells[125]	2	8.5±0.4	26.0±1.0	60.8±3.2	-38.7±0.6	1.5±0.1
Fetal Atrial Cells[125]	8	1.2±0.3	16.6±3.8	57.2±5.0	-34.9±1.6	1.0±0.1
Ventricle-like hES cells[125]	28	7.0±0.8*	24.0±1.9	80.0±3.5	-48.0±1.7	0.6±0.1
Fetal Ventricular Cells[125]	6	8.9±4.3†	23.6±3.5	69.0±9.1	-38.5±1.6	0.8±0.1
Figure 10A (Ventricular)	1	22.6	37.3	109	-71.7	1.58
Figure 10B (Atrial cells)	1	16.6	19.6	86.3	-66.7	3.26
Figure 10C (Ca2+ current)	1	2.3	38.7	90.8	-52.1	0.731
*Measured Maximum 20.0 V/s †Measured Maximum 26.7 V/s						

Summary

An iterative process was used to arrive at the final isolation method as described above. These fibroblast-like cells, though not yet characterized as precursors to cardiomyocytes, have desirable properties. They readily adhere not only to fibronectin, but normal tissue culture plastic as well. Comparatively, very little adhesion to either poly-L-lysine or collagen type I was seen. Once adherent, the cells migrate outward from larger spheroids to form a monolayer colony. Several of these colonies could be seen in each dish of cells.

Using all the micrographs taken, the proliferation of the cells was quantified by estimating the mean diameter of each colony. Though it appears growth has taken place, the low numbers and large deviation in the size of individual colonies made it impossible to draw any statistically significant conclusions. Furthermore, this technique doesn't account for changes in cell density as the colony grows. Qualitatively, it appears the center of the colony becomes more densely populated with cells as they continue to disperse from the center.

Prior to proceeding with any *in-vivo* or co-cultivation experiments, the monolayer cells were further characterized through the use of immunofluorescence for markers associated with early and mature cardiomyocytes (α-actinin), as well as the presence of electrically coupled cells. Ideally, these cells should be electrically coupled and capable of spontaneous contraction once properly organized. The earliest this has been observed in culture is 6 days after isolation. Although the number of spontaneously contracting cells increased from 6-10 days in vitro, they still made up a small fraction of the total

monolayer grown in culture. In most instances, clusters of 10 or fewer cells contracted in unison, indicating good electrical coupling.

In addition, high levels of attachment took place on this culture for all conditions, with the most confluency seen in the collagen/fibronectin dishes. The tissues were dissociated into some individual cells as well as larger spheres of cells, which were observed to attach to the surface of the dish and spread out over the course of several days. Many of these spheroids were the sites of spontaneous contraction; by 10 days, some of these had reached up to 1 mm in diameter and could be seen with the naked eye. A careful review of the literature has not shown precedent for such large, spontaneously contracting spheroids in culture. In addition to making basic observations of these spheroids, several attempts were made to isolate, dissociate, and re-plate these cells to form an entire monolayer of electrically coupled cells. Unfortunately, once dissociated, the cells lost their ability to electrically couple, thus rendering further investigation into their potential favorable properties impossible.

By the fourth day *in vitro*, there are cells binding to fibronectin-coated tissue culture clusters as well as glass coverslips. More early adhesion was observed on the atrial cells than the ventricular cells. As previously introduced, this is likely a function of ventricular cells being closer to mature cardiomyocytes, even in growing hearts, as the left ventricle has the job of circulating blood through the early vasculature. An improvement in cell adhesion would be desirable for both immunolabeling and co-cultivation experiments in the future, particularly on the LV coverslips. It was observed that the cell attachment to the surface of the Petri dishes was not remarkably better or worse than that on the coverslips themselves. The images used above as examples of

cardiomyocytes on 4 days *in vitro* are from the very same coverslips used for the immunohistochemistry of α-actinin.

The purpose of this experiment was to identify the patterns of α-actinin within the cardiomyocytes cultured from human fetal hearts. Immunofluorescent staining can be a fickle technique requiring a great deal of practice for optimal results. Early trials revealed the labeling of cell debris but few intact cells. There were very few regions where the To-Pro (labeling nuclei with an excitation wavelength of 633 nm) was more intense than the background, leading to the conclusion that intact cells were either washed from the slide or destroyed. Subsequently, with improved binding of cells to the coverslips, fewer cells were lost or damaged. The above fluorescence pictures were taken to show that an α-actinin banding pattern could be observed consistent with expectant results and showing positive binding, though considerable non-specific binding was observed in some images.

The timing of immunofluorescence was such that it was done as soon as possible after the cells were cultured, in order to characterize the cells as they were *in situ*. Indeed, the optimal time window turned out to be approximately 5 days in vitro, to allow for sufficient binding of cells but before many of the cells begin transforming. Cells that were cultured for 11-12 days *in vitro* were observed to be flattening out and taking a more senescent appearance without α-actinin banding.

Figure 8 shows green + red merged images for ventricular (Figure 8A,B) and atrial cells (Figure 8C,D) after optimization of immunofluorescence methods. Here, the green fluorescence is clearly labeling cytoskeletal structures within the cells. Ventricular cells were observed with a very regular, striated pattern, indicative of Z-bands of mature

cardiomyocytes, with a space between striations of 2 μm, consistent with measurements

of sarcomere length *in vitro*.[126] Atrial cells were observed with an amorphous pattern of

expression along the cytoskeleton following the contours of the cell body, consistent of

more stem-like cells. Together, the immunofluorescence and cell culture observations are

consistent with published literature, which showed that atrial (i.e., outflow tract) cells are

at a more immature stage than cells of the ventricles[84,93,94,105-107,110].

In addition to staining for α-actinin, the isolated cells were stained for ISL1, the

fetal marker for primitive outflow tract cells. However, no positive expression was

observed in culture. As described in the literature cited above, ISL1 expression decreases

rapidly in human fetal specimen between 11 and 18 weeks gestation, and further after

several days in culture[107,110]. If in future experiments a specimen is obtained which is

shorter in gestation, further work can be performed to identify the remaining sub-

population of ISL1^{+} cells in the heart.

After 10 days *in vitro*, prior to electrophysiological measurements, the cells were

transferred from tissue culture plastic to a glass coverslip. The cells of interest were

gently released and reattached to a coated coverslip, a patch clamp applied and whole cell

transmembrane voltage recordings taken (Figure 10, Table 4). Figure 10A is consistent

with the prototypical action potential of a ventricular cardiomyocyte, with a rapid

depolarization, plateau, and repolarization. The action potential in 10B is more consistent

with atrial cells, with a slower depolarization and less of a plateau.

The calculated values for upstroke velocity vary from those of Mummery et al[125].

Specifically, the calculated velocities fall between the published average and maximum

velocities. The reason for this is typically attributed to variables in the quality of

recording. Temperature, ionic concentration of the bath, and electrode characteristics and placement all effect whole cell patch clamp measurement. The upstroke velocity is primarily a measure of Na+ channel current, and measurement of this parameter in particular is susceptible to small leakage currents around the edges of the electrode[127]. More important is the observation that the upstroke velocity for atrial cells is slower than that of ventricular cells. This is consistent with what is known about the propagation of action potentials in the heart. The depolarization of AV nodal and atrial cells is slowed relative to the SA node and ventricular cells to allow a delay for the ventricles to fill prior to systole.

The overshoot voltage, i.e., the maximum voltage at the end of depolarization, as well as the amplitude, i.e., the difference between maximum depolarization and maximum hyperpolarization, is somewhat higher for our isolated cells compared with the published work of Mummery et al[125]. Further, the resting potential is somewhat lower (more negative). These numbers are all interrelated and a product of relative amounts of sodium, potassium and calcium channels. In this case, the electrophysiological characteristics observed for figure 10A and B more closely resemble those of mature ventricular and atrial cells, respectively, relative to the embryonic and fetal cells reported[120]. The embryonic/fetal action potentials have resting potentials between -20 and -40 mV, overshoots between 16.6 and 26.0 mV, as well as clear hyperpolarizations, which increase the amplitude voltage with respect to the resting potential. Mature cardiomyocytes are typically thought to have a resting potential of -80 to -90 mV and an overshoot of about 35 mV, with very little hyperpolarization, as is observed in our action potentials[120].

59

The third panel (Figure 10C) shows a much different characteristic action potential than in 10A or B. Whereas the ventricular and atrial resting potentials are approximately -70 mV, the resting potential is nearer to -50 mV. Additionally, no plateauing of the repolarization as a result of the measured potassium and calcium currents balancing is observed. Based on literature and affirmed by our colleagues, this action potential, rather than a whole cell membrane potential, is depicting primarily Ca^{2+} ion currents rather than sodium currents, as most voltage gated sodium channels are depolarized at a lower (more negative) resting potential than -50 mV[120].

In pursuit of the first phase of this project, this portion of the research provided positive results. A number of cardiomyocyte isolations were carried out, resulting in α-actinin+ cells with action potentials. Most importantly, spontaneously contracting cells were observed. These cells, if collected and implanted in an animal model for MI, would have the potential to improve cardiac repair.

Based on the accumulation of cell culture, immunohistochemical and electrophysiological findings, each cardiac isolation produced a widely heterogeneous mixture of atrial-like and ventricular-like cells with a range of "stemness" from immature CDCs to terminally differentiated cardiomyocytes. Future work to be pursued may include efforts to improve the isolation in order to obtain a more homogeneous cell population, with a greater ratio of stem cells to mature cardiomyocytes, and with a greater proportion of spontaneously contracting cells. For now, that work would fall outside the scope of this dissertation, which is primarily concerned with the proof-of-concept of a novel tracking system, into the realm of a molecular biology project.

In addition to the observed heterogeneity of the isolated cells, the cell yield, particularly of spontaneously contracting cells, is disproportionally low compared to the amount of effort required to obtain them. For this proof-of-concept, a need exists for a cell line which can be grown easily with a high yield of homogeneous cells, to allow for a variety of *in vitro* and *ex vivo* experiments. Thus, subsequent chapters herein present data using human bone marrow-derived mesenchymal stem cells, which are easily isolated from whole bone marrow specimens by their adhesion to tissue culture plastic, and which grow rapidly in culture, and are thus much more practical for our needs. The scientific community at large has not yet reached a consensus on the merits of CDCs versus hMSCs; as introduced in chapter 1, hMSCs are capable of differentiation to myocardial lineages, and many reports indicate a positive reaction to hMSCs following myocardial infarction. Conversely, while the hMSCs are shown to have immunomodulatory properties, some reports do indicate an immune response upon injection in MIs. Even with improvements to cell yield, reliance on a constant supply of hMSCs is a challenge, both in terms of lab time and IRB compliance required. Thus, we established a line of immortalized hMSCs which retain stem cell properties yet grow indefinitely, to be used as a model for primary hMSCs in these preliminary experiments. The following chapter is a record of this process.

CHAPTER 3: EVALUATION OF THE PROLIFERATIVE CAPACITY OF HUMAN FETAL MESENCHYMAL STEM CELLS

Introduction

In the previous chapter, human fetal and murine cardiac stem cells were isolated from hearts and cultured, with mixed results. While cardiac stem cells were clearly observed as shown by spontaneous contractions, α-actinin expression and electrophysiology, the cell yield was quite low, particularly the availability of spontaneously contracting cells. Additionally, many efforts to manipulate the cells, such as passaging to attach them to new surfaces, led to adverse changes in the cell phenotypes. Many contracting cells ceased contraction, or became non-viable altogether. Thus it became clear that a better source of stem cells would be required for the proof of concept of a stem cell tracking system.

As discussed in chapter 1, human mesenchymal stem cells (hMSCs) derived from bone marrow are readily adapted to cell culture. They can be easily isolated from other cells of the bone marrow by virtue of their adherence to tissue culture plastic. Once they adhere, they grow rapidly, doubling every 1-2 days. hMSCs stimulated with the de-methylating agent 5-azacytidine are commonly shown to differentiate into cardiac lineages, and studies have shown decreased myocardial infarcts following treatment with stimulated hMSCs[83-88].

Primary hMSCs proliferate rapidly in culture for typically 3-4 weeks and endure 3-4 passages with trypsin before they become senescent and eventually stop proliferating altogether. In addition, the bone marrow specimens needed for acquisition of primary cells can occur irregularly, with long waiting periods in between specimens. Thus, we

carried out an immortalization of hMSCs in order to develop an indefinite source of cells that can model the stimulated hMSCs *in vivo* and *ex vivo.*

Immortalization of primary cells for use in culture is a relatively common practice. Typically the cell is transfected with a gene that confers immortality by impeding cell processes such as telomere shortening and senescence/apoptosis. A wide range of genes are used; here, we selected the gene encoding for human papilloma virus E6/E7 oncoproteins, which have been shown to activate telomerase by upregulating expression of human telomerase reverse transcriptase (hTERT) expression[128-131]. Additional hTERT is commonly transduced into the cells as well[132]. By preventing telomere shortening, the life of the cell is increased considerably. The E6/E7 proteins have been implicated in a number of other oncogenic pathways, particularly in cervical cancer[130,131]. However, *in vitro*, the proteins seem to have a limited effect on the cell phenotype[129], making them an ideal candidate for use in our stem cell applications.

After exhaustive searches of the literature, to the best of my knowledge, this report represents the first case of an immortalized hMSC cell line. The implications of an immortalized stem cell line mean the dependence on a constant source of primary cells is reduced, and a number of preliminary proof-of-concept experiments can be carried out by growing these lines.

Materials/Methods

Human papilloma virus (HPV)-16 expressing E6/E7-LXSN and hTERT-LXSN were generously provided by Prof. Al Klingelhutz (Department of Microbiology, University of Iowa). Transfection of cells was carried out by Prof. Assouline according to previously described methods[128,129,132]. A 17 week-old fetal bone marrow specimen

identified as F015 was prepared according to the standard protocol: the cells of the specimen were seeded onto 3-60 mm tissue culture dishes and the following day, all non-adherent cells were removed by rinsing the dish with PBS. Half medium changes were performed every 2-3 days, using DMEM + 10% fbs. The remaining, adherent cells were confirmed as stromal cells on the fifth day of culture by immunolabeling with STRO-1 antibody according to established protocols. The use of discarded human fetal tissue for biomedical research application was reviewed and approved by the University of Iowa Institutional Review Board (IRB # 199008391; continuously approved from September 22, 2005 – August 31, 2015).

STRO-1 immunolabeling was carried out by Prof. Assouline. Mouse anti-human STRO-1 was produced as hybridoma cell lines grown in serum-free medium and RPMI medium with 10% fetal bovine serum (Developmental Studies Hybridoma Bank, University of Iowa). hMSCs grown on poly-l-lysine-treated glass coverslips were exposed to 100 μL of a blocking compound containing 3% fish gelatin and 0.75% Triton X-100. This was left on the sections for 30 minutes. Based on the validation results indicating 24 μg/mL of IgG in the hybridoma supernatant, 200 μL each of concentrations of 1.5 and 5 μg/mL were prepared for use as primary antibodies on 2 of the coverslips. The 2 concentrations of primary antibodies were added and left overnight at 4°C to allow full penetration into the tissue. The secondary antibody, donkey-anti-mouse IgG-488 was used at a concentration of 1:1000, and left on the sections for 90 minutes. Between each stage of staining, 3 sets of 5 minute rinses in PBS were performed. The coverslips were mounted on glass slides, sealed with clear nail polish, and immediately used in fluorescent microscopy, with a series of FITC images acquired.

The immortalization procedure begins with cells at 30-40% confluence, on the fifth day in culture. One 60 mm dish was given a media cocktail of 2.5 mL DMEM+10% fbs, 1 mL (HPV)-16 E6/E7-LXSN -expressing retrovirus, 1 mL hTERT-LXSN- expressing retrovirus, and 10 µL Polybrene, a polycationic supplement that improves viral transfection. The control dish was given only 1 mL E6/E7-hTERT, and a third dish was untreated. All 3 dishes were incubated overnight. The following day, the virus-containing medium was removed, and the dishes were rinsed once with PBS. Fresh medium was added, and over subsequent days, half-medium changes and trypsinizations were performed as necessary. In order to plot cell growth without detaching the cells for a true cell count each day, a value defined as the passage number plus the current confluence level was used. For example, cells of the primary plating at 70% confluence have a value of 0.7, cells of passage 1 at 50% confluence have a value of 1.5.

Results

The group led by Beverly Torok-Storb was the first to report on the cell marker STRO-1, and the capacity of STRO-1$^+$ cells to differentiate along multiple lineages, including bone, cartilage, and adipose tissue[13]. In that report, the expression pattern of STRO-1 is punctiform, located throughout most of the cytoplasm. The STRO-1 expression pattern we observed was identical (Figure 11). Multiple colonies of cells were observed in each coverslip with the same pattern of expression. Additionally, an irrelevant cell line known to be STRO-1$^-$ was similarly assayed and found not to have any specific STRO-1 binding, thus confirming that the cells are STRO-1$^+$ at the time of the start of immortalization.

In some cases, the presence of serum can adversely affect the quality of the immunolabeling; conversely, the absence of serum can adversely affect the growth of the hybridoma cell line, resulting in a lower yield of primary antibody. Therefore it was initially unclear which approach to use for our specific experiment, and we chose to implement both. The STRO-1 yield measured by HPLC and reported by the DHSB was identical for both hybridoma conditions (24 μg/mL). After immunolabeling, good results were obtained with both approaches, though a slightly higher degree of non-specific binding was observed in the antibody grown in serum free medium. Based on the reported value, the highest quality labeling was observed when using a primary antibody concentration of 5 μg/mL, with staining overnight at 4°C.
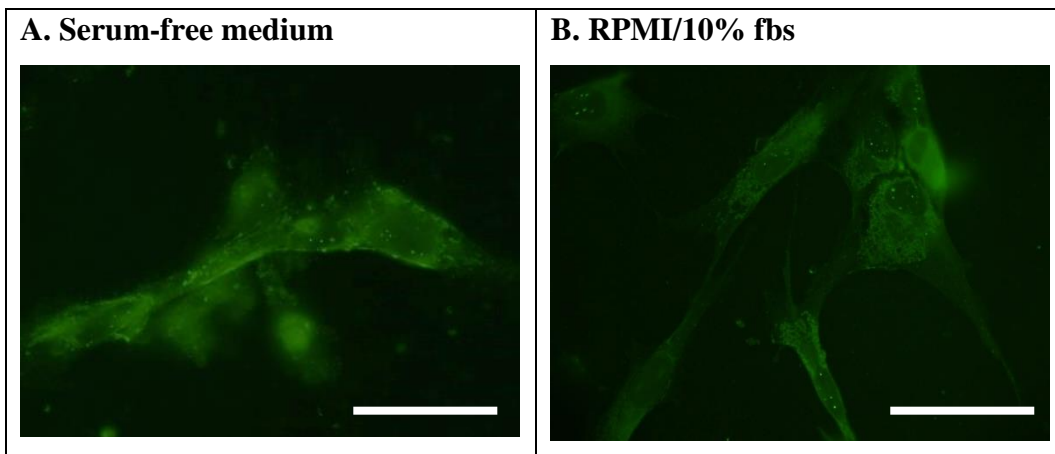
Figure 11. STRO-1 immunolabeling of primary human bone marrow-derived mesenchymal stem cells (hMSCs). hMSC specimen F015-P1, after 5 days in culture, testing two different hybridoma-produced primary antibodies. A shows the primary antibody cultured in serum-free CD medium, while B shows the antibody grown in RPMI/10% serum. The perinuclear, punctiform morphology of labeling is consistent with results reported in literature. Scale bars represent 10 μm.

The regular observations made to the non-infected and infected cell cultures are shown (Appendix, Table A1), in addition to the plot of daily observations quantified as passage number plus current confluence (Figure 12). Beginning on day 5 in culture, one 60 mm dish of cells was exposed to both the E6/E7-LXSN and hTERT-LXSN transduction vectors, while a second dish was left untreated. A third dish contained the coverslips used for the STRO-1 immunolabeling experiment; after the coverslips were used, the cells that remained were exposed to E6/E7-LXSN alone and observed. The time required for the cells to grow to full confluence was similar for all 3 dishes (15 days). Thus, all three dishes were passaged on day 15 and seeded onto larger 100 mm dishes.

At the start of the new passage, the non-infected cells began growing somewhat faster than the infected cells, reaching full confluence in 7 days (day 22 in culture). The infected cells, appearing to flatten/senesce slightly, were passaged 3 days later (day 25), despite only being 50% confluent, with the intent of stimulating new growth.

During the third and final passage for the non-infected cells, they quickly became fully senescent, with blebbing (apoptotic bodies) observed in a large proportion of the cells. Ultimately, the non-infected cells were discontinued on day 7 of their third passage (day 29 overall). Five days later, the cells exposed to E6/E7-LXSN alone had completely detached from the culture surface and were discontinued. The infected cells continued growing, slowly at first, so the growth medium was supplemented with MesenCult® mesenchymal stem cell growth factor cocktail. Soon the cells began dividing more rapidly, eventually approaching the doubling time (1-2 days) of primary hMSC cultures. To date, the cells have been repeatedly grown to confluence in 75 cm^2 flasks and passaged 27 times.
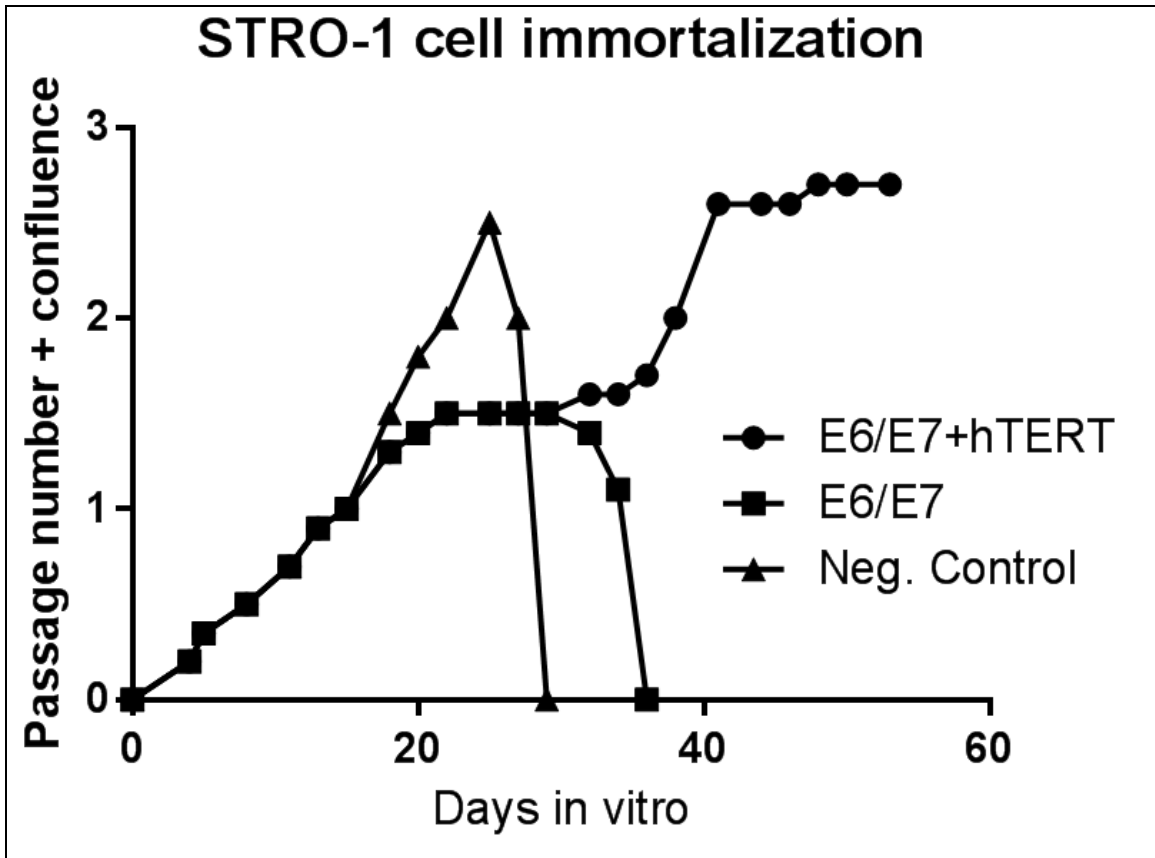
Figure 12. Immortalization of STRO-1+ human mesenchymal stem cells (hMSCs). STRO-1+ hMSCs were transduced with virus expressing E6E7-LxSN and hTERT-LxSN, E6/E7-LxSN alone, or left untreated. The non-infected cells grew faster after the first and second passage but became senescent by day 27 in culture. The cells infected with E6/E7 alone looked identical to the cells infected with E6/E7 and hTERT until day 32 when they too became senescent and detached from the culture surface. The cells infected with both E6/E7 and hTERT have continued to grow; to date, the cells have been grown to confluence and passaged 27 times.

Summary

In this chapter, I report on the successful immortalization of hMSCs via transduction of LxSN (HPV) E6/E7 and hTERT genes. Additionally, to the best of our knowledge, this is the first report of immortalized hMSCs. Using immunolabeling, the cells were confirmed STRO-1$^+$ at the time of the immortalization. Subsequent follow-up immunolabeling showed the cells had changed to STRO-1$^-$ phenotype during immortalization. However, it is known that non-immortalized primary hMSCs typically lose their STRO-1 expression in 10-15 days as well. Thus, while the STRO-1 expression is consistent with non-immortalized cultured cells, the precise characterization of the "stemness" of the cells should be addressed prior to any *in vivo* animal studies, via stimulation in culture with appropriate stimulatory growth factors for the various lineages (bone, cartilage, adipose tissue, and myocardium).

Nevertheless, the implications of having a constant supply of hMSCs to use as a model for *ex vivo* labeling and imaging studies is significant. To date, the immortalized hMSCs have outlasted their control counterparts by many passages, yet continue to have growth and morphology characteristics consistent with STRO-1$^+$ hMSCs. In subsequent chapters, I present data using these cells to prove the concept of stem cell tracking using our novel engineered nanomaterials.

CHAPTER 4: MESOPOROUS SILICA NANOPARTICLES FOR THE NON-INVASIVE TRACKING AND FATE DETERMINATION OF CARDIAC PROGENITOR CELLS

Introduction

Selection of a model stem cell tracking system

As stated in chapter 1, the scientific community has yet to agree upon a standard regenerative therapy that uses stem cells to repair/restore a myocardial infarct. In part, this is due to limitations in animal modeling. Up to this point in time, the majority of hMSC experiments have occurred entirely *in-vitro*, or in some cases, using nude mice as an *in-vivo* model. In the latter cases, cells are typically injected, then immunolabeled upon the sacrifice of the animal, using a subset of the previously described markers. At present, a substantial hurdle is being able to follow the migration and *in-situ* differentiation of these cells in the living animal. Several groups are currently labeling hMSCs with superparamagnetic iron oxide (SPIO) particles in order to enhance contrast for magnetic resonance (MR) imaging, with promising results[46-48].

To that end, we have developed a mesoporous silicate nanoparticle (MSN) loaded with a reagent of interest by simple diffusion, and capped using SPIOs. Once internalized, application of a disulfide-reducing agent, such as dihydrolipoic acid (DHLA) uncaps the particles, allowing the controlled release of the product contained therein. The concept was shown by our collaborators at Iowa State (the lab of the late Prof. Victor S.Y. Lin) using fluorescein-containing MSNs capped and endocytosed into HeLa cells[77], followed by cytochrome c (also using HeLa cells)[79] as well as vancomycin/ATP into astrocytes[76]. While our collaborators continued to work with

delivery of reagents *in vitro*, we chose to broaden the technology to include imaging
applications.

In order to track implanted MSCs *in vivo*, a non-invasive imaging modality is
needed. When determining which modality to use, it is important to consider the spatial
resolution needed and whether or not the modality produces ionizing radiation in tissue.
Magnetic resonance imaging is capable of producing high spatial resolution without
ionizing radiation; however, it is one of the more expensive modalities to operate, and
scans can be slow and susceptible to motion artifact from the subject.

MRI and contrast enhancement

As discussed in chapter 1, MRI utilizes small perturbations in the magnetic field
arising from differing proton spin densities $\rho(x,y)$ in tissue to generate its images. The
MR signal of a specific tissue can also be described by its T_1, T_2, or T_2* relaxation times,
and the scan itself can be described by its parameters (repetition time T_R, echo time T_E,
and/or flip angle α)[37]. After a material is magnetized with a certain flip angle α, the
magnetic field in the longitudinal axis M_z decays (relaxes) with time constant T_1, and by
varying the time between pulses (repetition time T_R), tissue with different T_1 relaxation
times show up with different levels of intensity in the reconstructed image. This is
known as a T_1-weighted image. In a T_2-weighted image, the echo time T_E (the time
between the pulse and the midpoint of signal readout) is used to generate differing
intensities between tissues of different T_2/T_2* relaxation times (the time constant of
relaxation or "de-phasing" in the transverse plane, or M_{xy}). T_1-, T_2- or T_2*-weighting is
controlled by the MRI operator by varying T_R/T_E on the scanner to achieve the desired
contrast[46]. T_1-weighted scans have relatively short T_R/T_E values, while T_2- and T_2*-

weighted scans have larger values for both T_R/T_E, and proton density scans have long T_R and short T_E. On the Varian® 4.7 T small animal scanner, I have optimized our scan parameters for proton density with slight T_1- and T_2-weighting; a typical T_1 weighted scan has a T_R of 800 ms and a T_E of 15 ms, while a typical T_2-weighted scan has a T_R of 2300 ms and a T_E of 15 ms. Using these parameters, the T_2-weighted scan typically provides better anatomical details, while both T_1- and T_2-weighted scans are enhanced by contrast agents.

Also as mentioned in chapter 1, additional contrast can be achieved by using one of several contrast agents which alter the apparent T_1 or T_2 relaxation time. Of these, the most popular are the relatively well-tested ferromagnetic (iron-containing) agents and the somewhat more novel gadolinium agents. Most ferromagnetic contrast agents involve the use of superparamagnetic iron oxide (SPIO), which perturb the tissue's local magnetic field, causing a change in T_2 or T_2^* relaxation time[49,50].

While ferromagnetic iron oxide and superparamagnetic iron oxide nanoparticles have been widely used as a clinical magnetic resonance contrast agent for some time, gadolinium compounds have been used more recently. The commercially available Magnevist® and Gadovist® are gadolinium chelating agents. That is, they are made up of relatively large, branched polymers called dendrimers which trap one or more ions of gadolinium within their structure. Recently, recalls over toxicity concerns have arisen with gadolinium MRI contrast agents, in which the chelating molecule releases freely-floating ions of gadolinium into the bloodstream, causing renal failure, a condition known as nephrogenic systemic fibrosis[133-135]. As a reaction, these agents have been contraindicated in patients with already poor kidney function. For the rest of the

population, the contrast agents have been deemed safe. In the meantime, new dendrimers are being developed which have a higher affinity for gadolinium ions, and thus are less likely to release the ions into the bloodstream.

In addition, other groups are working on various forms of gadolinium oxide nanoparticles, and additional work has been done in generating a particle capable of both MR contrast fluorescent labeling using rare-earth elements, such as Europium [136]. These particles have the advantage of being traceable either *in vivo*, using MR, or *ex vivo*, using fluorescent or confocal histology. Europium typically has broad excitation in the ultraviolet (250-350 nm wavelength) spectrum and sharper emission wavelengths at 615 nm, When combined with a development agent can be used in time resolved fluorescence (TRF) assays, or by simply blotting a solution on paper and exposing it to a 254 nm black light [137].

Several groups have previously demonstrated the use of SPIO nanoparticles as a label for certain cells. Daldrup-Link, et al, compared hematopoietic progenitor cells labeled with 4 different SPIO-derived particles, including 120-180 nm ferumoxides and 20-50 nm ferumoxtran, both dextran-coated iron oxides, 50 nm iron oxide/dextran particles bound to transferrin for receptor mediated endocytosis, and 100-200 nm liposomes loaded with 20-50 nm iron oxide particles coated in an anionic dextran derivative. When loaded into cells and pelleted in a microcentrifuge tube, contrast was strong for all 4 particle types with a variety of scanning parameters[138]. In a follow-up, the same group injected $1*10^7$, $2*10^7$ or $3*10^7$ ferumoxide-labeled, human CD34+ hematopoietic stem cells into the tail vein of mice and performed T2*-weighted MR scans at differing times. Results showed that at 24 hours, many cells were cleared by the

liver and spleen, but that some had also arrived at the bone marrow as indicated by a loss of signal (darkening pixels). Histology confirmed that the cells were intact, expressed human CD34, and still contained the contrast agent[139,140]. Several studies have similarly shown that when cells are injected into the circulation, a great majority is cleared by the blood-filtering organs (liver, spleen, or kidney) before reaching the desired destination.

When feasible, a more appropriate method is to inject the labeled cells directly into the tissue of interest. As an example of this, Jendelová et al injected SPIO-labeled bone marrow stem cells or embryonic stem cells of mice into the brains of other mice with brain or spinal cord lesions. Five weeks after the injections, hypointense (dark) regions could be seen at the lesion sites, with the presence of labeled stem cells confirmed by histology[141].

While iron-based contrast agents have a very high r_2 relaxivity (100-200 $s^{-1} \cdot mM^{-1}$), making them useful for T_2-weighted MRI, they are not as useful for T_1-weighted imaging. Conversely, chelated gadolinium, with 7 unpaired electrons, and gadolinium oxide nanoparticles are most often used pre-clinically and clinically as T_1 contrast agents. However, with moderate values for both r_1 and r_2, Gd_2O_3 nanoparticles have been shown to have effects in both T_1 and T_2 imaging (causing a hyperintensity/brightening of tissue in T_1, and a hypointensity/darkening of tissue in T_2) that increase with a concomitant increase in magnetic field of the scanner[52-54].

In my Master's thesis, I presented data characterizing the MRI relaxivity of various formulations of our lab's MSN particles (Fe_3O_4-FITC-MSN and Gd_2O_3-FITC-MSN), as well as its uptake and viability in culture with hMSCs. My Master's research concluded with the measurement of boluses of hMSCs labeled with Fe_3O_4-FITC-MSN,

injected into the myocardium of *ex vivo* mouse hearts and scanned with T2*-weighted MRI. In this chapter, I report on the further testing of MRI using *ex vivo* hearts, injected with Gd_2O_3-FITC-MSN and scanned with T1- and T2-weighted MRI. In addition, the Assouline lab further functionalized the MSN particles for use in ultrasound applications; herein I present data characterizing the particles in real-time with ultrasound, first using agar phantoms, then proceeding to *ex vivo* imaging using excised mouse hearts mounted in agar, and finally near-*in vivo* conditions in which a freshly sacrifice mouse heart is injected *in situ*.

Materials/Methods

Reagents

Gadolinium (III) chloride hexahydrate ($GdCl_3 \cdot 6H_2O$), cetyltrimethylammonium bromide (CTAB, $CH_3(CH_2)_{15}N(CH_3)_3Br$), diethylene glycol, tetraethoxysilane (TEOS), and (3-aminopropyl)trimethoxysilane (APTMS) were purchased from Alfa Aesar (Ward Hill, MA). Sodium hydroxide (NaOH) was purchased from VWR (Radnor, PA). Methanol, dimethyl sulfoxide (DMSO), and toluene were purchased from Fisher Scientific (Pittsburgh, PA). Tetramethylrhodamine isothiocyanate (TRITC) was purchased from Sigma-Aldrich (St. Louis, MO). 2-[Methoxy(polyethyleneoxy)propyl]trimethoxysilane and trifluoropropyl trimethoxysilane were purchased from Gelest (Morrisville, PA). Dulbecco's modified eagle medium (DMEM), fetal bovine serum (FBS), and penicillin-streptomycin (pen-strep) were purchased from Life Technologies (Grand Island, NY).

Particle synthesis/characterization

Particle synthesis was initially carried out by chemists in the Assouline lab; I assisted with final functionalization and characterization prior to carrying out *in vitro* and *in vivo* experiments. First, a gadolinium oxide colloid was obtained following the previously reported synthesis[142]: $GdCl_3 \cdot 6H_2O$ (11.53 g) was dissolved in 200 mL of diethylene glycol at 60°C overnight under vigorous stirring. Aqueous NaOH (7.5 mL, 3M) was added and the solution was heated at 140°C for 1 hour and then at 180°C for 4 hours. The obtained transparent colloid of gadolinium oxide nanoparticles was stored at room temperature. CTAB (1.0 g, 2.745 mmol) was dissolved in nanopure water (480 g, 26.67 mol), followed by the addition of NaOH solution (2.0 M, 3.5 mL, 7.0 mmol). The mixture was heated to 80°C for one hour. To this clear solution, TEOS (4.7 g, 22.56 mmol) was added drop wise, followed by immediate addition of 1 mL of the gadolinium oxide colloid. The reaction was stirred vigorously at 80°C for 2 hours and then the solution was filtered and washed with copious amount of water and methanol and dried under vacuum. The CTAB surfactant was removed by Soxhlet extraction with methanol for 24 hours and then dried under vacuum to obtain gadolinium oxide functionalized mesoporous silica nanoparticles (Gd_2O_3-MSN).

Fluorophores (TRITC or FITC) were reacted with APTMS (2.2345 μL, 0.0128 mmol) in DMSO for 2 hours, and TRITC-Gd_2O_3-MSN or FITC-Gd_2O_3 MSN was prepared by grafting 0.05 mL of the resulting product on the previously synthesized Gd_2O_3-MSN (100 mg) in toluene under reflux for 24 hours. The resulting solution was filtered and the obtained pink solid was washed with copious amount of methanol and then dried under vacuum. Finally, the particles were further functionalized with

poly(ethylene glycol) (PEG) and trifluoropropyl moieties by grafting 2-[Methoxy(polyethyleneoxy)propyl] trimethoxysilane (0.2mmol), followed by trifluoropropyl trimethoxysilane on TRITC-Gd_2O_3-MSN or FITC-Gd_2O_3-MSN (100 mg) in toluene under reflux for 24 hours. The resulting solution (PEG-CF_3-FITC-Gd_2O_3-MSN or PEG-CF_3-TRITC-Gd_2O_3-MSN) was filtered and the obtained pink or yellow solids were washed with copious amounts of methanol and then dried under vacuum.

Our chemists characterized the particles by X-ray diffraction, using a Rigaku Ultima IV diffractometer, and nitrogen sorption analysis in a Micromeritics ASAP 2020 surface area and porosity analyzer using the Brunauer-Emmett-Teller equation to calculate surface area and pore volume and the Barrett-Joyner-Halenda equation to calculate the pore size distribution. The materials were also visualized by transmission electron microscopy (TEM) by supporting samples on copper grids in a Tecnai G2 F20 microscope operating at 200 kV. I used dynamic light scattering (DLS) to obtain particle size distribution and zeta potential data, using the Malvern Zetasizer Nano ZS instrument.

To remove any freely floating FITC or TRITC fluorophore, I repeatedly centrifuged, resuspended, and rinsed the particles with copious amounts of phosphate buffered saline (PBS). After each centrifugation, the supernatant was collected and measured on a fluorimetric plate reader until no fluorophore was detected.

Cell culture/labeling

Human fetal mesenchymal stem cells (hMSC line F015, described in chapter 3) were grown in DMEM supplemented with 10% fetal bovine serum. Cells at 80% confluence were exposed to 125 µg/mL of PEG-CF_3-FITC-Gd_2O_3-MSN or PEG-CF_3-TRITC-Gd_2O_3-MSN for 24 hours. Unbound particles were removed by discarding the

growth medium and rinsing the culture with PBS. The cells were passaged with trypsin, centrifuged, and counted for number and viability using a hemacytometer and trypan blue exclusion dye. For *ex vivo* studies, cells were fixed by resuspension in 4% PFA and stored at 4°C until use.

MRI

An adult male mouse (age 8 months, strain IL10$^{-/-}$ x IL10$^{-/-}$) was heparinized via an intraperitoneal injection of about 0.1 mL, then anesthetized in a container of isofluorane until unconscious (about 1 minute). Full anesthesia was confirmed by a lack of response to tail pinch with forceps. After opening the chest cavity, the inferior vena cava was severed and saline delivered via a 22 ga. needle through the left ventricle near the apex of the heart using a gravity-fed apparatus with a hydrostatic pressure of about 10 kPa or about 75 mmHg. After the blood was cleared, a 4% PFA solution was delivered through the same needle at the same pressure for about 10 minutes. After perfusion fixation, injections were typically made in the wall of the left ventricle in an anterior location to the perfusion needle, and the heart was dissected and stored in 4% PFA at 4°C until scanning.

The Varian® 4.7T magnetic resonance scanner was used to scan the heart. After discussion of the parameters of the scan with Dan Thedens (Department of Radiology, University of Iowa), he carried out the scans and the raw data was given to me for processing and analysis. Proton density MRI scans with T_1- and T_2-weighting were acquired using a fast spin echo multislice (FSEMS) pulse sequence, with a typical in-plane resolution of 50 x 50 μm in plane and a slice thickness of 100 μm. Typical scan parameters are T_R=800 ms/T_E=15 ms for T_1-weighting, and T_R=2300 ms/T_E=15 ms for

T$_2$-weighting. The echo train length used was typically 8, and the number of scans averaged to obtain an image ranged from 4 to 12 based on time constraints. The raw image in DICOM format was opened in ImageJ, converted to NIFTI format, and placed through an automated pre-processing routine in MATLAB that involves background subtraction and partial volume correction by reverse diffusion[143,144]. The processed image was then opened in MIPAV, where additional segmentation, if needed, was performed manually. The background was masked using manual segmentation, tracing the outline of the heart for each slice.

Following background removal, the heart could be visualized in a 3D rendering or quantitatively analyzed for evidence of intensity changes. After exploring the 3D rendering to confirm the locations of the injections, a volume of interest (VOI) for each injection site was selected using MIPAVs isolevel VOI selection tool and statistics generator. A third VOI was selected from the surrounding PFA as a control for low intensity regions in the image. Statistical significance was computed in a pairwise fashion using the comparison of two means test statistic for independent samples with unequal variances:

$$t = \frac{(\bar{x}_1 - \bar{x}_2) - (\mu_1 - \mu_2)}{\sqrt{(s_1^2/n_1) + (s_2^2/n_2)}}; \nu = \frac{\left[\frac{s_1^2}{n_1} + \frac{s_2^2}{n_2}\right]^2}{\left[\frac{(s_1^2/n_1)^2}{(n_1 - 1)} + \frac{(s_2^2/n_2)^2}{(n_2 - 1)}\right]},$$

where t is the value of the test statistic with ν degrees of freedom.

Ultrasound

In the Robert Weiss lab, I used the VEVO® 2100™ small animal ultrasound scanner to scan several concentrations of materials suspended in agar in 60 mm Petri

dishes using the 30 MHz ultrasound probe. Definity®, the commercially available ultrasound contrast agent used as a positive control. When shaken vigorously, the Definity® contains octafluoropropane at a concentration of about 1.1 mg/mL; this concentration was assumed as the basis for comparison. Particles tested included CF_3-FITC-MSN at biologically relevant concentrations (0-0.5 mg/mL), Definity®, mixed according to the protocol, then diluted to concentrations of 62.5, 125, and 250 µg/mL octafluoropropane, assuming an initial concentration of 1.1 mg/mL. Finally PEG-Gd_2O_3-MSN was used as a control. For ultrasound visualization of labeled cells, two populations of $2.5x10^6$ cells, one of which was labeled with 200 µg/mL PEG-CF_3-FITC-Gd_2O_3-MSN, were suspended in 60 mm Petri dishes containing warm agar and stirred until the agar set. Each agar was repeated in triplicate.

Based on the concept of speckle introduced in chapter 1, I quantified the speckle originating from the cells and nanoparticles relative to the negative control agar. The threshold was determined by measuring the grayscale value two standard deviations above the mean in the negative control. This threshold value was applied to the subsequent particle-containing agars, wherein pixels above the threshold were assigned a 1, and all others were assigned zero. Thus the proportion of 1 values in a given region of interest was defined as the speckle density.

In perfusion-fixed murine hearts (described above) I mounted hearts injected with labeled cells as indicated (Figure 13) in melted agar, then placed the agar phantom in a negative 20°C freezer to rapidly cool. After the agar was set, it was returned to room temperature, and the 30 MHz ultrasound transducer was used to scan the heart. The 2-D transducer was scanned across the entire heart in short axis while acquiring a 1 second

cine loop to approximate 3-dimensional ultrasound tomography. The cine loop in AVI

format was converted to a stack of 30 2-dimensional TIF images which could then be

opened and saved as a 3-dimensional NIFTI file and processed/analyzed in a similar

manner to MRI files described above. To interpret the thickness of each 2D slice of data,

the transducer was assumed to have been moved at a constant velocity, producing 30

slices that covered approximately 10 mm in 1 second, for a slice thickness of 0.33 mm.
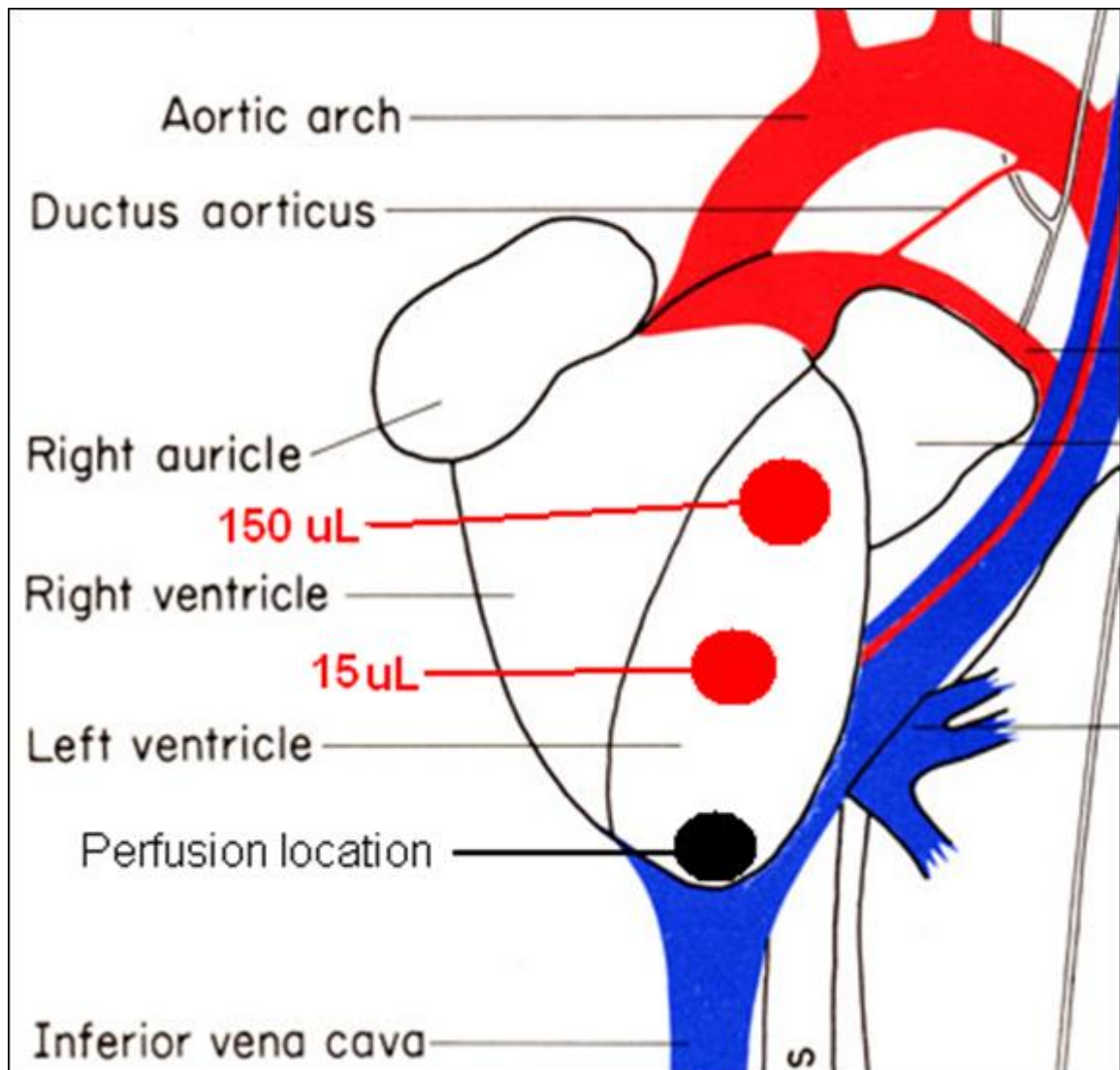
Figure 13. Schematic of injections of human mesenchymal stem cells labeled with PEG-CF$_3$-FITC-Gd$_2$O$_3$-MSN. After perfusion fixation of the mouse, injections were made into the left ventricular wall and scanned using 30 MHz ultrasound. 150 μL = 150,000 cells; 15 μL = 15,000 cells.

In order to visualize a real-time injection of particles, the probe was held steady in short axis near the midline of the heart, while a needle was inserted through the agar into the right ventricle, and 2 x 10^5 PEG-CF$_3$-FITC-Gd$_2$O$_3$-MSN-labeled hMSCs suspended in 20 μL PBS was deployed during the acquisition of a cine loop. The signal generated by the labeled cells during the injection was quantified by selecting the frame at the start of the injection and subtracting from it each subsequent frame, to obtain a 3-D (2 dimensions + time) representation of the change in signal. Using the MIPAV VOI tools, the right ventricle was isolated and the average signal difference was plotted over time.

To more closely represent a clinically relevant scenario, a freshly sacrificed mouse was scanned with a transthoracic approach, and with the probe held stationary with the heart in short axis, a needle containing 2 x 10^5 PEG-CF$_3$-FITC-Gd$_2$O$_3$-MSN-labeled hMSCs suspended in 20 μL PBS was deployed during the acquisition of a cine loop. A second mouse was given an injection of PBS alone as a negative control. In order to confirm the delivery of particles, excised hearts were washed with PBS and scanned for FITC fluorescence using the IVIS® in vivo imaging system (Xenogen, Perkin-Elmer, Waltham, MA).

Results

Particle synthesis/characterization

Various characterizations were performed at each step in the process of synthesizing the PEG-CF$_3$-TRITC-Gd$_2$O$_3$-MSN. Powder XRD analysis confirmed hexagonally arranged mesopores in the diffraction pattern of the Gd$_2$O$_3$-MSN as evident by the intense d$_{100}$, and well resolved d$_{110}$ and d$_{200}$ peaks characteristic for MSN (Figure 14A). Transmission electron micrographs of the Gd$_2$O$_3$-MSN particles showed this pattern as well as uniform

size distributions and good dispersibility with little aggregation (Figure 14A, inset).

Nitrogen sorption analysis of the TRITC-Gd_2O_3-MSN exhibited a Type-IV isotherm,

typical of mesoporous materials, with a BET surface area of 710 m^2g^{-1}. The average pore

diameter for TRITC-Gd_2O_3-MSN by BJH calculation is 24 Å. The fully synthesized

PEG-CF_3-TRITC-Gd_2O_3-MSN was characterized by DLS; the median hydrodynamic

diameter of the particles was 187.3 nm, with 96.3% of the particles falling within the

primary distribution peak, spanning between 90 and 400 nm, resulting in a polydispersity

index (PDI) of 0.535 (Figure 14B).

Figure 14. Characterization of PEG-CF₃-TRITC-Gd₂O₃-MSN. (A) Powder X-ray diffraction patterns of TRITC-Gd_2O_3-MSN before surfactant removal (blue) and after surfactant removal (red). The intense peak at 2.5 2θ is characteristic of hexagonally arranged pores in MSN. (A, inset) Transmission electron micrograph of a Gd_2O_3-MSN. Visualized particles had a uniform size distribution and showed no formation of aggregates. (B) Hydrodynamic size distribution of PEG-CF_3-TRITC-Gd_2O_3-MSN as measured by dynamic light scattering. The primary peak has a median particle size of 187.3 nm.

Characteristics of cell uptake/viability

As shown (Figure 15), early binding of FITC-MSN particles to cell membranes is observed after one hour, with further binding and early endocytosis by 7 hours. By 27 hours, most of the particles appeared to be in the outer regions of cell cytoplasm, and few particles remained outside the cells. As the days progressed, the particles were seen to homogenize into fewer, larger compartments and migrate towards the cell nuclei, likely indicating that they are being compartmentalized into vesicles. A few dividing cells were observed throughout the experiment, showing the equal cytoplasmic division of particles between daughter cells. The same patterns of internalization, compartmentalization and division appeared with the Fe-MSN particles. It was also observed in these cells, however, that cells that took up a disproportionately large amount of particles were found to be apoptotic. Sonicating the particles to ensure the particle dispersion was as uniform as possible helped to prevent this overdosing of some cells.

Following the growth curve shown (Figure 15B), the cells grew in a manner similar to unlabeled cells, doubling in number about every 3 to 4 days until reaching contact inhibition in 10 days. Imaging analysis of intensity per cell showed a concomitant decrease, with the signal approximately halving every 3-4 days (Figure 15C). This observation, combined with the observations that nearly all the particles remained within cells (Figure 15D), and all the cells remained labeled (Figure 15E), further indicates retention of particles and equal cytoplasmic division during mitosis.
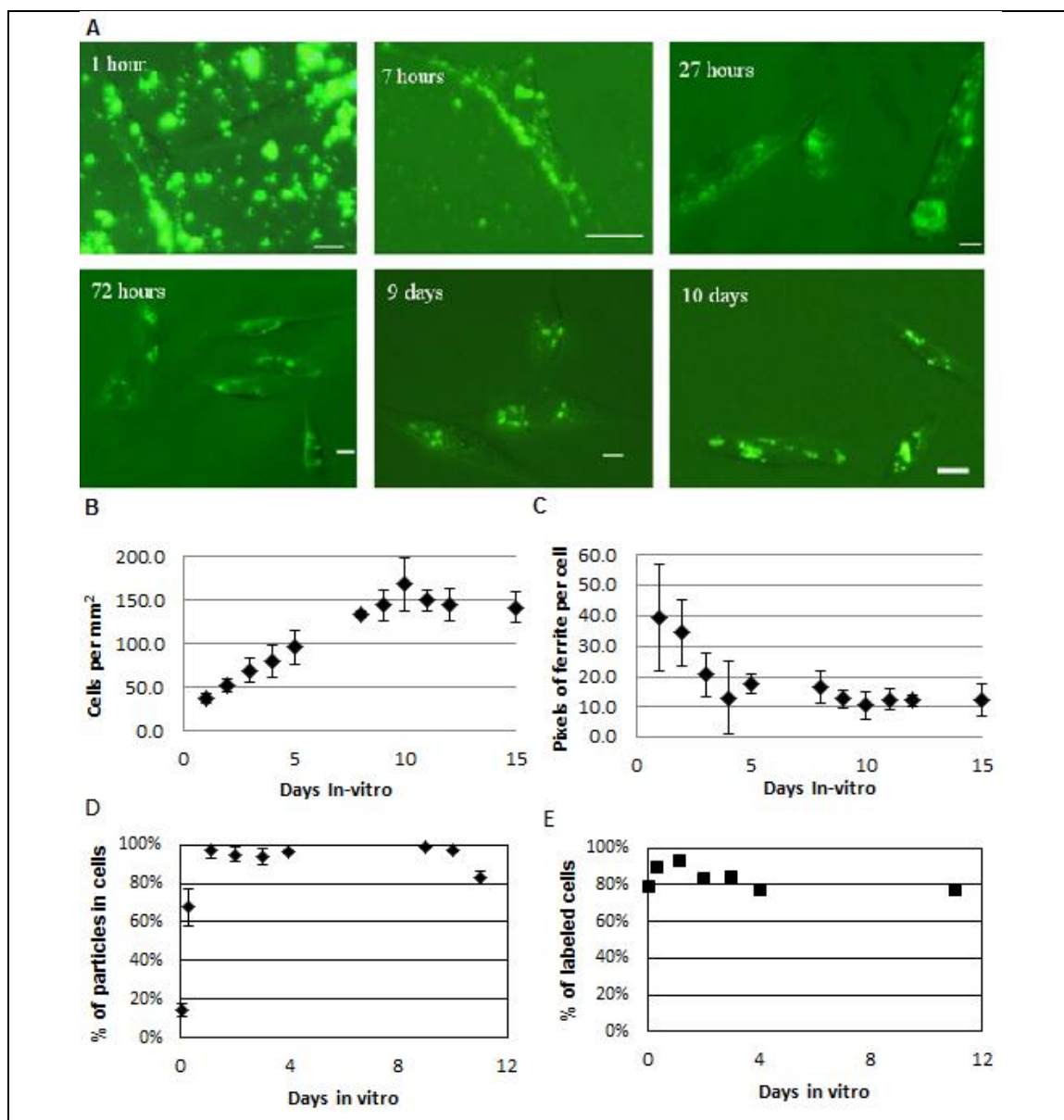
Figure 15. Kinetics of ferrite-capped, FITC-loaded mesoporous silica nanoparticles (MSN) added to human fetal mesenchymal stem cells (A). Pictures were taken at the indicated times following addition of particles to the growth medium at 125 μg/mL. Scale bars indicate 25 μm. Plots showing healthy proliferation of labeled cells (B), measurement of intracellular MSN particles (C), percentage of particles that are incorporated in cells (D) and percentage of cells that contain at least one detectable endosome of particles (E). Error bars indicate one standard deviation (n = 4 at each data point).

Ultrasound characterization

In order to compare ultrasound contrast with current standards, agar phantoms containing various concentrations of Definity®, CF_3-FITC-MSN, and PEG-Gd_2O_3-MSN were scanned at 30 MHz (Figure 16). Qualitatively, a clear difference was observed in the higher concentrations of CF_3-FITC-MSN relative to the negative control, though the Definity® contrast was clearly more intense for equivalent concentrations. Quantitatively, the Definity® contrast was maximal even at low concentrations (62.5 μg/mL), while the CF_3-FITC-MSN showed a linear response at biologically relevant concentrations (up to 500 μg/mL). A control consisting of the non-echogenic components of MSN (PEG-Gd_2O_3-MSN) showed no clear change relative to the PBS control. Though the phantoms were run in triplicate and average values were consistent across each repeated agar, the high variability within the agars led to large standard deviations, thus none of the values were statistically significantly different.

A noticeable increase in ultrasound intensity was observed in the agar containing cells labeled with CF_3-FITC-MSN compared with the same number of unlabeled cells (Figure 17A-B) and with a negative control containing only plain agar. After opening the still images in ImageJ and calculating the average greyscale value for each region of interest (ROI), the results were plotted (Figure 17C). The agar containing the labeled cells (116.7 ± 41.3) did have a higher average than both unlabeled cells (85.5 ± 35.5) and the negative control (33.4 ± 24.1). Due to the large variation within each ROI, the differences were not statistically significant.

A.

B.

Figure 16. Echogenicity of trifluoropropyl-functionalized MSN compounds (CF₃-FITC-MSN). (A) Agar phantoms were prepared with various concentrations of commercially available Definity®, CF₃-FITC-MSN, and PEG-Gd₂O₃-MSN, and scanned with 30 MHz ultrasound. (B) Definity® demonstrated a large speckle density which saturated even at very low concentrations, while the CF₃-FITC-MSN showed a more linear response curve at biologically relevant concentrations. For each data point, n=3; error bars indicate standard deviation; *-p<0.05 vs. PBS; ***-p<0.0001 vs. PBS.

A. Unlabeled cells	B. Labeled cells

C

Figure 17. Echogenicity of human mesenchymal stem cells (hMSCs) labeled with trifluoropropyl-functionalized MSN compounds (CF₃-FITC-MSN). 2.5×10^6 hMSCs were labeled with 200 µg/mL CF₃-FITC-MSN, while another 2.5×10^6 were left unlabeled. The cells were suspended in melted agar which was stirred until set. Unlabeled cells (A) have a higher speckle density than the plain agar negative control (PBS), but lower than labeled cells (B). Comparison of average grayscale value of each specimen (C). Error bars represent 1 standard deviation.

The heart receiving two injections of 150,000 and 15,000 PEG-CF$_3$-FITC-Gd$_2$O$_3$-MSN-labeled cells as indicated (Figure 13) was embedded in agar and scanned at 30 MHz using a "pseudo" 3-D tomography approach to generate a 3-dimensional map of the entire heart. (Figure 18A). Within the map, a feature could be seen on the ventral surface of the left ventricle that matched the location of the larger of the two injections (Figure 18A, circle). When the heart was re-rendered in a short axis view, two intensely bright regions were seen within the ventral surface of the ventricular wall. Dorsal to that signal (distal to the placement of the transducer) was a strongly hypointense region forming an acoustic shadow behind the high intensity region. This series of observations represents a prototypical signature from a particularly high contrast in ultrasound[145]. The rendering was further enhanced by adding a rainbow pseudocolor map; the volume of interest appears intensely red, while its shadow appears dark blue (Figure 18B). The smaller of the two injections was not detected using the same approach.

A.

B.

Right outflow tract
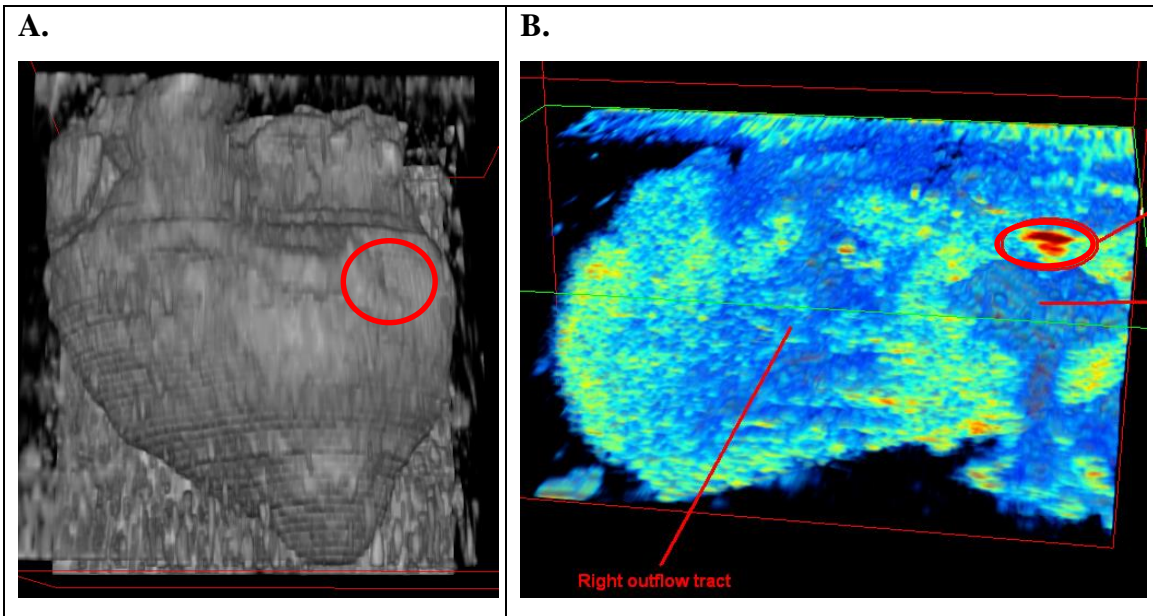
Figure 18. Echogenicity of labeled human mesenchymal stem cells (hMSCs) in an
***ex vivo* mouse heart.** Following an injection of 150,000 PEG-CF$_3$-TRITC-Gd$_2$O$_3$-MSN labeled hMSCs into the left ventricle of an excised mouse heart, the heart was mounted in agar and a "pseudo" 3-dimensional ultrasound was generated by scanning a 2-dimensional 30 MHz transducer across the agar surface (A). A surface feature was observed that matched the location of the injection (circle). (B) A short axis pseudocolor view of the same feature. Note the high intensity region and accompanying low intensity "shadow" distal from the transducer location.

The first use of ultrasound to measure real-time injection of 200,000 labeled cells was also performed in an excised heart mounted in agar. Here, the probe was held steady as the needle was guided to the right ventricle of the mounted heart (Figure 19A). A 10 second, 100 frame cine loop was recorded immediately before and during the ejection of material from the needle, with the peak signal change shown (Figure 19B, circle). The transducer was sufficiently steady from frame 35-66 that the heart itself was mainly stationary. The difference between frame 46, immediately before the injection, and each subsequent frame until 66, was used as the basis for the colorized image (Figure 19C). Within this same time frame, the average grayscale value was plotted over time (Figure 19D), clearly showing a spike from baseline values near 70 before the injection, to a peak slightly over 100. Over the subsequent 2 seconds, the injection dissipates and the average grayscale value returns to its pre-injection level.

In order to represent a more biologically relevant scenario, 2 mice were scanned with an *ex vivo* heart kept *in situ*, using a transthoracic echocardiography approach (Figure 20). Here, the absence of visual cues made coordination of the transducer, injection needle, and ejection time more difficult than in the agar-mounted heart. Although the needle is not in line with the transducer, the pulses of ejected fluid are visible in the animations. Screenshots from minimal and maximal signals are shown below for a heart injected with 200,000 PEG-CF$_3$-TRITC-Gd$_2$O$_3$-MSN-labeled hMSCs (Figure 20 A-B) and one injected with unlabeled cells (Figure 20 C-D). When the average value of the regions indicated by the circles are plotted over the time course of the cine loop, the average grayscale value of the labeled cells (50.9) is considerably higher than that of the unlabeled cells (26.3) (Figure 20E). In order to confirm the

injection of labeled and unlabeled cells, the hearts were excised, rinsed, and taken to the

IVIS for fluorescence imaging, where a clear difference in fluorescence intensity was

observed (Figure 21).

Figure 19. Real-time ultrasound tracking of stem cell injections in an agar-mounted heart. Images are screenshots from cine loops taken at 30 MHz before (A) and after (B, C) injections of 200,000 labeled cells in the right ventricle of an agar-mounted heart. (C) The injection was highlighted (red) by subtracting the frame immediately before the injection from each subsequent frame. (D) Plot of average grayscale value of the right ventricle over time (*-start of injection).

Figure 20. Real-time ultrasound tracking of stem cell injections in an *in situ/ex vivo* heart. Images are screenshots from cine loops taken at 30 MHz before (A, C) and after (B, D) injections of 200,000 labeled cells in an ex vivo mouse (A, B), injections of 200,000 non-labeled cells in an ex vivo mouse (C, D). Injection sites are indicated (circles). (E) Plot of average grayscale values for regions indicated by the circles.

Figure 21. *Ex vivo* **fluorescence corroborates real-time injections of labeled and non-labeled cells.** Following the injections shown in which ultrasound was used for real-time cell imaging, (Figure 20), the whole hearts were excised and scanned using the In Vivo Imaging System (Xenogen® IVIS), using the excitation and emission wavelengths for TRITC. Fluorescence intensity is measured in photons·s^{-1}·cm^{-2}·steradian. A clear increase in fluorescence in the heart injected with labeled stem cells indicates a successful injection.

Ex-vivo cardiac imaging (sequential MRI/ultrasound)

As described above, in my Master's thesis I reported the labeling and injections of

hMSCs with Fe_3O_4-FITC-MSN and subsequent detection using T_2-weighted MRI. Here,

three boluses of 50,000 cells injected in the left ventricular wall were found to be

qualitatively distinguishable as well as statistically significantly different from both the

surrounding myocardium as well as the negative control (the needle track at the apex of

the heart used to carry out the injections). That data is summarized below (Figure 22,

Table 5).

Table 5: Measurements, statistical comparisons of volumes of interest indicated (Figure 22)

Description	# of Voxels	Volume, uL	Avg Voxel Intensity	Std Dev of Intensity	p vs. PFA	p vs. heart
PFA control	328	0.260	0.0033	0.0016		
Average of 3 injections	649	0.514	0.0155	0.0102	p<0.005	p<0.0005
Heart tissue sample	530	0.419	0.0457	0.0039		
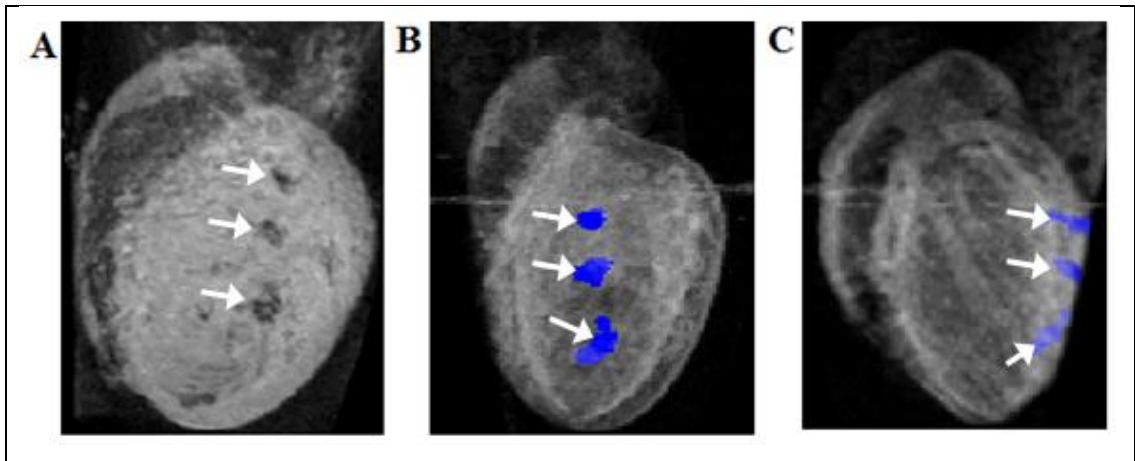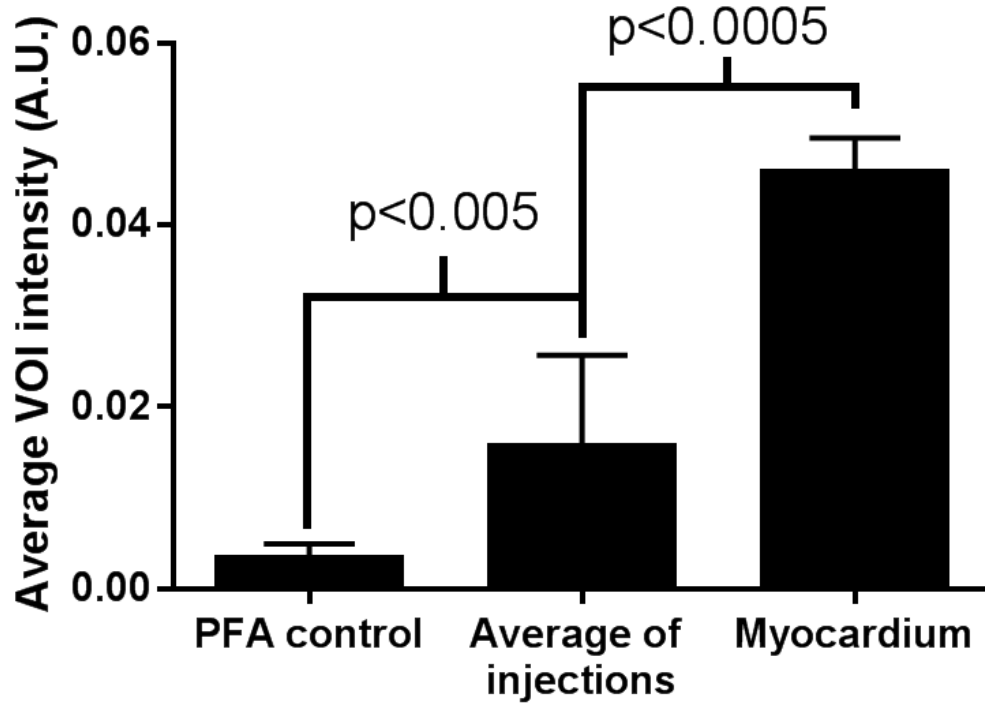
Figure 22. Fe₃O₄-FITC-MSN-labeled human mesenchymal stem cells (hMSCs) are detectable in the left ventricular wall of mouse heart. Three injections, each 50,000 cells in 20 mL phosphate buffered saline were made in the left ventricular wall (arrows) and scanned with T_2-weighted MRI. The average of the three injections (blue) are statistically significantly different from the surrounding myocardium and negative control (PFA/needle track). Error bars indicate standard deviation of each respective VOI.

When the new PEG-CF$_3$-TRITC-Gd$_2$O$_3$-MSN particles were generated, a combination of the above approaches was used to demonstrate sequential imaging. An injection of 130,000 labeled cells was injected in the right ventricular wall of an *ex vivo* mouse heart as shown (Figure 23A). The heart was immediately embedded in agar and scanned with 30 MHz ultrasound (Figure 23B). Using a similar approach as previously shown (Figure 18), a 3-dimensional scan was acquired by scanning the 2-dimensional transducer across the surface of the agar. A hyperintensity within the wall at the location of the injection was observed. This region had an average grayscale value of 140 and a peak intensity of 195, while the surrounding tissue had an average value of 115.

After the completion of the ultrasound scan, the heart was removed from the agar, placed in 4% paraformaldehyde, and scanned with T$_1$-weighted MRI (Figure 23C). With improved spatial resolution over ultrasound and high contrast arising from the particles, a bright needle track was observed. This was manually segmented using selection tools in MIPAV, and compared with sampled regions of normal myocardium and paraformaldehyde present in the ventricles (Figure 23E). The calculated MR value for the injection was statistically significantly higher than that of both the normal myocardium and the ventricles (Table 6).

Table 6: Measurements, statistical comparisons of volumes of interest indicated (Figure 23)

Name, Slice, Contour	# of Voxels	Volume (mm^3)	Avg Voxel Intensity	Std Dev of Intensity	p-value vs. injection
Ventricle	2590	1.5808	0.0017	0.0006	$p < 0.0005$
Heart tissue	8187	4.76	0.0041	0.0009	$p < 0.0005$
Injection site	301	0.1837	0.0087	0.0024	

Figure 23. Sequential imaging of transplanted human mesenchymal stem cells (hMSCs) in the *ex vivo* mouse heart. (A) An injection of 130,000 hMSCs labeled with PEG-CF$_3$-TRITC-Gd$_2$O$_3$-MSN was made in the right ventricular wall of an ex vivo mouse heart, where it was embedded in agar and scanned with 30 MHz ultrasound (B), in which the cell bolus was observed (arrow). Subsequently, the same heart was scanned with T$_1$-weighted MRI, where the needle track could be seen in greater detail (C, arrow). Following imaging, the heart was sectioned and stained for use in mapping injection data (D). The injection site was significantly more hyperintense than both heart tissue and the paraformaldehyde present in the ventricles (E). Error bars indicate the standard deviation of each respective VOI.

Summary

Particles are synthesized with reliable, repeatable characteristics

The goal of this chapter was to show feasibility of an improved approach to stem cell tracking for autologous stem cell transplant in MI, using novel, functionalized MSN produced by our lab. These particles were engineered to be nanoscale for intracellular delivery, biocompatible, and multimodal, for use in fluorescence, ultrasound, and MRI.

The particles were first provided to me synthesized as PEG-CF$_3$-TRITC-Gd$_2$O$_3$-MSN, and characterized by x-ray diffraction, pore size analysis, and electron microscopy. By each of these metrics, the particles were consistent with similarly reported MSN[77-79,146,147]. From this basis, I first characterized the particle size distribution and zeta potential by dynamic light scattering (Figure 14B)[148]. The median hydrodynamic diameter of 187.3 nm indicates that the particle is small enough to be engulfed by competent cells. By comparison, the lysosome, into which it is believed the engulfed particles are merged, can range from 100 – 1000 nm[149]. The distribution metrics indicate a strongly monodisperse size distribution, with 96.3% of the particles falling between 90 and 400 nm and a polydispersity index (PDI) of 0.535. On the Malvern instrument, a PDI of 0.1 indicates an extremely high monodispersity, such as what is seen in calibration standards, while a value greater than 0.7 indicates a polydisperse sample. The zeta potential, a measure of electrostatic repulsion between charged particles in a dispersion, is also an indicator of stability of a colloidal suspension. Zeta potentials further from zero (positive or negative) indicate a stronger repulsive force and higher shelf stability. Our measured zeta potential of +20 mV indicates a moderately stable particle. Indeed, I

observe that, over days to weeks, our particles may fall out of suspension, though they are easily resuspended by shaking or sonicating the vial.

Particles are readily engulfed by mesenchymal stem cells with no adverse effects on viability

While the particles were engineered using bioinert or biocompatible components, our lab tests each new formulation for biocompatibility by first determining the optimal dose which causes less than 10% cell death relative to unlabeled controls. In a 24 well culture plate, $2.5*10^4$ mesenchymal stem cells were seeded per well, and the MSN doses (in μg/mL) were 10, 25, 50, 125, 250, and 500. The maximum dose that did not cause an excessive observable toxicity to the cells was 125 μg/mL. This has been the optimal dose for each new particle formulation, and is consistent with other published values[68,76,150-153]. Given that result, each subsequent experiment was performed using 125 μg/mL as a standard dose for all MSN particles.

Next, the uptake kinetics and labeling efficiency were measured (Figure 15). I prepared a new culture, using a slightly sparser initial cell population so that it may be observed over a longer time course. After adding the particles, I observed the cells several times throughout the first day, then daily thereafter. Within hours, the particles could be seen aligning with the cell membranes, and lightly tapping the culture plate showed that the particles did not move from this position. They appeared to be effectively stuck to the cell membranes, rather than loosely associated. The following day, nearly all of the particles were inside the cells, and on subsequent days, the clusters of intracellular particles appeared to decrease in number but increase in size, suggesting the cells are consolidating the particles as they would a foreign object[149]. In addition, the

majority of the particles were observed to move towards the nuclei of the cells as the days progressed.

The uptake mechanism has not been determined with certainty, but in all likelihood is a non-specific form of endocytosis. Because no receptor ligands have been used on these particles, any form of receptor-mediated endocytosis can be ruled out. When labeling mesenchymal stem cells with their MSN particles, Huang et al showed electron micrographic evidence for clathrin-coated pits as the uptake mechanism[68]. In the future, however, the addition of receptor ligands may certainly be an area of interest for delivering these particles to a specific cell *in vivo*. This will be discussed in greater detail in the next chapter.

Trifluoropropyl-functionalized mesoporous silica nanoparticles are echogenic in vitro and in ex vivo animal models

As introduced in chapter 1, all clinically used ultrasound contrast agents are microspheres between 1- 5 μm in diameter loaded with a high molecular weight gas which alters the speed of the propagating sound wave. The use of nanoscale materials to improve ultrasound contrast is a relatively new field. Given the average speed of sound in soft tissue of 1540 m/s and a 30 MHz ultrasound transducer, the propagating wave has a wavelength of 51 μm, far too large to resolve a single nanoparticle. However, it is capable of resolving clusters of particles or labeled cells as specular noise. The previous studies using nanoparticles in ultrasound contrast include nanobubbles[40], silica[41,42], dextran-iron[43], or gold[44]. We chose to combine two of these approaches: by functionalizing our silica particles with trifluoropyl moieties, we anticipated an increase in contrast due to the trifluoropropane nanobubble formation on the particle surface.

Indeed, I observe a significant increase in speckle density for CF_3-FITC-MSN relative to the PBS control ($p < 0.05$) at 250 and 500 μg/mL (Figure 16). The densities are also significantly higher than the control particles (PEG-Gd_2O_3-MSN) at 250 and 500 μg/mL ($p < 0.05$). The particles without trifluoropropyl moieties showed speckle as well, but to a lesser degree; only at 500 μg/mL was the PEG-Gd_2O_3-MSN significantly higher than the negative control.

Thus, the findings show a positive ultrasound response to CF3-FITC-MSN at biologically relevant concentrations. Injections of free particles in mice are typically on the order of 1 mg in 0.1 mL saline, but quickly dilute to 0.5 mg/mL in the 2 mL of circulation. Cells in culture are exposed to growth medium containing 125 μg/mL of particles. Assuming all of the particles are internalized by the cells, a dish of 2 x 10^6 cells will contain up to 625 μg of particles, which would dilute to 312 μg/mL when injected intravenously. Additional analysis of labeled vs. non-labeled cells follows.

Comparatively, the commercially available Definity® does have a much higher contrast-one which nearly saturates the transducer even at low (62.5 μg/mL) concentrations. It is important to note here, however, that Definity® is only used as a comparison because it is well-known; we are not expecting to compete directly or outperform their product. Our CF_3-FITC-MSN address a need which is impossible for larger ultrasound contrast agents to address: intracellular delivery and tracking. To date, with a sparse few players in this niche market, any documented improvement in signal is useful.

To that end, we next labeled hMSCs with CF_3-FITC-MSN and tested them against non-labeled cells, again using agar phantoms (Figure 17). The average speckle density

for non-labeled cells was significantly higher than that of the plain agar negative control

($p < 0.01$), while the density for an equivalent number of labeled cells was significantly

higher than both the non-labeled cells ($p < 0.025$), and the negative control ($p < 0.005$).

In the preparation of these phantoms, 2.5×10^6 cells were exposed to 0.5 mg total weight

of CF_3-FITC-MSN. Assuming all of the particles were engulfed by the cells, one can

estimate the uptake by a single cell to be 0.2 ng of MSN, and the total MSN concentration

in the 2 mL agar phantom to be 250 μg/mL. Comparing the speckle density for labeled

cells (0.23 ± 0.048) to that of the ultrasound phantom at 250 μg/mL (0.10 ± 0.028), the

values are in the same order of magnitude, and any increase seen in the labeled cells can

be attributed to the cells themselves, which contribute an additional component of speckle

to the overall signal.

Moving to an *ex vivo* heart animal model, I injected 150,000 PEG-CF_3-TRITC-

Gd_2O_3-MSN labeled hMSCs into the left ventricle, mounted the heart in agar, and in

order to maximize the generated data a 3-dimensional image was acquired by scanning

across the agar surface with the 2-dimensional transducer at a constant rate (Figure 18).

This technique was particularly useful for mapping out the entirety of the heart, locating

the injection site, and processing the 2-D images that contain it. The signal observed was

small in volume but highly intense, with an acoustic shadow in the tissue behind the

obstruction relative to the transducer. This is a prototypical signature for a very large

contrast in which insufficient sound passes through the obstruction to further highlight

tissue interfaces[145]. While this form of shadowing is not necessarily desirable in a

clinical setting when precise delivery of stem cells to the MI zone is of the utmost

importance, for the purposes of feasibility, it does demonstrate the presence of a high intensity signal.

Because the ultrasound component of this project is to be used for guidance of the initial cell transplant, as part of my feasibility demonstration, I also wanted to show the measurement of injections of cells into the heart in real-time. In the first round of experiments, I again used ex vivo hearts mounted in agar phantoms. Holding the transducer steady while delivering a bolus of cells to the right ventricle, a cine loop recorded the seconds before and after the ejection of material from the needle (Figure 19). Initially the ejection was clearly visible, but to further enhance the visualization, the frame immediately before the start of the ejection was subtracted from each subsequent frame. Assuming the transducer was held stationary during the acquisition, the only signal difference should be a result of the fluid movement. Indeed, for 20 frames (2 seconds), the signal enhancement, shown in red, worked well. After that point the transducer moves slightly and withdrawal of the needle changes the shape of the right ventricle. The average grayscale value of the right ventricle is plotted during this time as well (Figure 19D), reaching a peak greyscale value over 100, about 30 levels of gray higher than the value prior to the injection. The ejected cell suspension then dissipates throughout the right ventricle over the course of about 2 seconds as the average gray level returns to its initial value.

In order to more closely represent a clinical scenario, the subsequent studies were carried out in ex vivo mice, but with the heart still in the chest cavity. In this way, the signal must be acquired using a clinical transthoracic approach, in short axis from below or between the ribs. In addition, the co-localization of the transducer and injection needle

in the correct position in the heart is a logistical challenge. Nevertheless, labeled cells were delivered, as confirmed by fluorescence imaging of the excised hearts following the procedure (Figure 21). In the acquired cine loops, it is difficult to qualitatively identify clear intensity changes resulting from the ejection of material from the needle (Figure 20) in either the labeled or non-labeled cells. However, pulses of fluid in parts of the image belie the location of the needle slightly outside the scope of the transducer. Using these pulses as the region of interest, the average grayscale value was plotted on a time scale for the regions indicated (Figure 20E). Again, no large changes are observed from the pulses, however there is about a 2-fold increase in grayscale value of the labeled cells versus the non-labeled cells.

Feasibility of sequential imaging (ultrasound and MRI) demonstrated in animal models

As stated previously, the goal of this project is to show efficacy of a novel technology in the tracking and transplantation of stem cells in MI in a clinically relevant manner. This involves ultrasound, with results described above, as a model for transplant guidance, and MRI for longitudinal tracking of stem cell fate. In preliminary MRI studies of *ex vivo* heart imaging, hMSCs were labeled with Fe_3O_4-FITC-MSN and injected into the left ventricular wall for T_2-weighted imaging. Three injections of 50,000 labeled cells were made. The needle track at the apex of the heart, used for perfusion fixation, was segmented as a negative control (Figure 22). In T_2-weighted MRI, iron oxide has a darkening effect on the tissue, thus the site of the 3 injections are clearly distinguishable from the surrounding heart muscle. Qualitatively, it is more difficult to distinguish the

injection sites from the perfusion site, as the paraformaldehyde also has a low intensity in T_2. Quantitatively, the difference is sufficient to be statistically significant.

With the development of PEG-CF$_3$-TRITC-Gd$_2$O$_3$-MSN, the MRI strategy was changed to T_1-weighting, with everything else remaining equal. In this trial, the same heart was used for both ultrasound and MRI sequentially (Figure 23). After injections of labeled hMSCs, the heart was mounted in agar and scanned 3-dimensionally as described previously. Unlike the previous trial, no acoustic shadow was seen; however, a volume of significantly higher intensity than the surrounding tissue was observed at the injection site (Figure 23B). Corroboration was received when the heart was scanned in T_1-weighted MRI and a large hyperintense volume was observed at the injection site as well (Figure 23C). When the injection site was manually segmented and its average intensity compared with that of surrounding heart tissue and the paraformaldehyde-filled ventricles, the differences were statistically significant in both cases (Table 6, Figure 23E).

Chapters 2 and 3 represent the preliminary work necessary to accomplish the work in this chapter, which makes up the bulk of my work on the project. Here, through a variety of approaches designed to mimic the clinically relevant scenarios, feasibility was shown. Our novel technology, the functionalized mesoporous silica nanoparticles, are indeed capable of intracellular labeling, with high biocompatibility. Further, labeled cells are detectable in the heart using ultrasound in a transplant delivery approach, followed by MRI in a longitudinal follow-up approach. The detection threshold is limited by ultrasound rather than MRI, and is approximately 100,000 cells per injection. In the

next chapter, I will further discuss my conclusions regarding the approach as a whole, as well as additional ongoing and future work.

CHAPTER 5: CONCLUSIONS, ONGOING AND FUTURE WORK

In the Assouline lab, a wide range of biomedical applications, from cancer and inflammation, to environmental remediation, rapid detection of pathogens, and imaging in the nervous system, are addressed using novel nanoparticle agents. In the course of development of the particles, I was listed as a co-inventor on 2 patents (S/N 61/645,712 filed May 11, 2012, and 61/679,941, filed August 6, 2012) for my contributions to the larger work of the lab. As I completed my Master's work and began preparing my PhD research, I identified a problem (tissue regeneration following MI), for which the particles would be a novel solution. I began gathering preliminary data and prepared a proposal to use the particles in animal models for MI, which became the basis of my comps proposal, prepared and defended in 2014. Based on my proposal, I was provided with particles and immortalized stem cells to use as tools towards my work on MI. Thus, while the particles themselves are intellectual property of the lab at large (work to which I contributed), my intellectual contribution in this project is the novel application of the particles to potentially improve patient outcome following MI.

A number of findings of importance to the scientific community at large have resulted from my research contributions as well. While expression of STRO-1, a definitive marker for mesenchymal stem cells, has been observed by many in human adult bone marrow specimens[13,154-157], this is the first known observation of the marker in fetal specimens, and with respect to cardiac-derived stem cells, very few reports exist of isolating spontaneously contracting cells from fetal sources[158]. On the nanoparticles themselves, while a number of investigators are studying the multimodal uses of MSN[142,146,147], to the best of my knowledge this is the first reported use of nanoparticles

functionalized with trifluoropropyl moieties for ultrasound. This opens the possibility of intracellular labeling and tracking with ultrasound that did not previously exist. While tracking of injected stem cells is important for manifold reasons described in chapter 1, the clinical potential of an agent that is used only for cell tracking is limited. Using these tools to gather ex vivo and in situ images, I have demonstrated an entirely new strategy for cell tracking in myocardial infarction, and owing to the capacity of the MSN for loading and delivery, the potential also exists for therapeutic applications, the concepts I introduce in future work below. In the long term, I feel strongly that the lessons I have learned have prepared me to become a contributing member of the scientific community at large.

In MI, clinical trials with autologous stem cell transplants have led to mixed results, largely because the delivery of cells is imprecise due to insufficient guidance. The current standard method for clinical trials, catheterized delivery guided by intracardiac echocardiography, is more invasive, shorter-lived, and does not employ an agent for imaging the cells directly. In other words, the fate of the cells after transplantation is unknown. In pre-clinical animal studies, stem cell fate can be determined using histopathology; however, this is obviously a terminal procedure and cannot be translated to clinical use, in addition to being time consuming and costly. For all these reasons, there exists an opportunity to improve upon the current paradigm.

In this project, I aimed to address this need by taking advantage of our lab's core technology, the functionalized mesoporous silica nanoparticle, as a tool for the multimodal (ultrasound and MRI) tracking of labeled stem cells in animal models for MI. In order to accomplish this, I first evaluated two of the 3 primary sources of stem cells in

the heart: resident cardiac stem cells, and bone marrow-derived mesenchymal stem cells (chapter 2; the third cell type, endothelial cells, were studied by other members of the Assouline lab and ruled out due to their impracticality in ordinary tissue culture). Examples of progenitors of each cell type were grown and characterized accordingly. Due to its favorable growth and particle uptake, the bone marrow-derived mesenchymal stem cells were chosen for use in subsequent studies, and to generate a continuous supply of cells, the Assouline lab immortalized a population of cells. Following the viral transduction, I monitored the transfected and non-transfected cells until it was clear that the immortalization was a success (chapter 3).

With the cells well-characterized, in chapter 4 I test the novel PEG-CF$_3$-TRITC-Gd$_2$O$_3$-MSN, first *in vitro*, then demonstrating feasibility as a tool for intracellular labeling and stem cell tracking in the application of MI.

Particle performance

As outlined previously, the design criteria for a solution to the problem of stem cell tracking in MI are defined as: it must be nanoscale, for intracellular labeling; it must be biocompatible; and it must be multimodal, for imaging in fluorescence, ultrasound, and MRI. Our engineered nanoparticles, the PEG-CF$_3$-TRITC-Gd$_2$O$_3$-MSN, meet or exceed each of these criteria. With a median particle size of 187 nm, the particles are easily engulfed by hMSCs, with no cytotoxic effect. And particles, as well as labeled cells, were measured intracellularly with fluorescence, and using both ultrasound and MRI imaging modalities.

Selection of model cell

As described in chapter 1, both resident cardiac progenitor cells and bone marrow-derived mesenchymal stem cells have been implemented for regenerative approaches in MI, and both have mixed results. While the resident cardiac progenitors are already committed to a cardiac lineage, thus eliminating the need for chemical manipulations, the yield is very low, about 1 cell for every 10^4 collected in a biopsy. Conversely, while the yield is much higher for mesenchymal stem cells, which proliferate rapidly in tissue culture, the manipulations required to commit them to a cardiac lineage may confer immunogenicity not normally observed in these cells. Indeed, the results presented herein are consistent with published reports, and because of their high yield and rapid proliferation, the mesenchymal stem cell line was chosen as the model cell line for all labeling and tracking studies.

Assessment of animal model

The ultimate goal of any biomedical research should be its implementation in clinical settings to the benefit of the patient. In all therapeutic/diagnostic applications, this necessarily requires a pre-clinical (animal) stage of study. The approach taken by our lab is to ensure full characterization of the material in an *in vitro* setting (i.e., measuring the imaging signal in agar phantoms) prior to *ex vivo* studies (i.e., testing the interaction of a material with excised tissue). At this stage, many of the technical logistics of the study can be worked out at a minimum of cost and effort.

The final progression from *ex vivo* to *in vivo* animal studies adds many complexities that must be addressed carefully. Foremost on that list is to be compliant with all regulatory guidelines regarding animal welfare. All protocols must be proposed

to a qualified board and approved prior to their implementation. This can be a lengthy

process requiring results that show anything injected into an animal is non-toxic to both

the animal and the investigator. To that end, studies are ongoing in which various animal

models are implemented to assess the *in vivo* biocompatibility of our particles (see below:

"Ongoing/Future Directions")

A number of additional *in vivo* complexities present themselves in this study. For

instance, a live, beating heart is going to be nearly impossible to inject labeled cells into,

particularly a heart as small as a mouse. The risk of puncturing the heart is significant,

and insertion of even a small needle into the wall of the heart may disrupt its rhythm and

create a cardiac arrest. Larger animals are available, but at much higher cost, and until

recently, the only research MRI scanner available with a magnetic field larger than 3 T

was the Varian® small animal MRI. In our conversations with Dan Thedens, this scanner

is not equipped for the rapid pulse sequences and ecg gating necessary for cardiac MRI.

Ridgway et al presents a thorough review of strategies and pulse sequences for cardiac

MRI[159]; with the new research scanners available here, this portion of the research may

be more feasible in the near future.

Ongoing/Future Directions

Evaluate in vitro/in vivo biocompatibility and clearance of particles and labeled cells

in a mouse model (ongoing)

Evaluating in vitro biocompatibility-cell culture

Prior to undertaking any animal studies, tolerance by cells in tissue culture must

be determined for various configurations of MSN particles. Cell lines at our disposal for

testing include several adherence-dependent cell lines: human bone marrow derived

mesenchymal stem cells[13,160] (hMSCs), NIH3T3 murine embryonic fibroblasts[161], H4IIE murine hepatoma[162], and MB49 murine bladder cancer cells[163,164]. Consistently, the optimal particle dose proves to be 100-150 μg/mL regardless of cell type or particle configuration. Other groups have reported similar values for similar particles and cell types[150,165].

Compared with adherence-dependent cells, non-adherent cells are more difficult to label[166]. In a mouse model for bone marrow transplantation, murine induced pluripotent stem cells (iPSCs) stimulated for bone marrow production[167] were exposed to PEG-CF$_3$-FITC-Gd$_2$O$_3$-MSN particles. Initial studies showed poor labeling (less than 30% of cells were labeled) and an abundance of freely floating particles between the cells. Subsequently, the cell culture media was supplemented with polybrene or protamine sulfate during labeling; these polycationic supplements have long been used to improve uptake for viral transduction[168]. Protamine sulfate treatment improved binding to 58.9%.

Assessment of biocompatibility in vivo: bone marrow mouse-longitudinal tolerance

Using the mouse model for bone marrow transplant described above, I have begun to evaluate biocompatibility of labeled cells in intravenously exposed mice for longitudinal studies. The benefits of using this model for studying biocompatibility are that it is well-established[167], it allows for the *in vivo* tracking of labeled cells in addition to free MSN particles, and it represents another clinically relevant scenario in which the MSN can be utilized. Labeled iPSCs described above were injected intravenously using a retro-orbital approach. T$_2$-weighted MRI scans were acquired and the injection sites were analyzed relative to the contralateral eye revealing a noticeable signal change in the first

114

scan 3 hours after injection followed by a return to intensities equal to that of the contralateral side the following day, as particles entered the circulation. Similar hypointensities were observed in the kidneys, but with a longer latency; relative to pre-injection scans, the renal vasculature was darkened considerably 3 hours after injections. This hypointensity was observed 1 day following the injections, and largely returned to pre-injection values by the next scan, 6 days after injections. Our observations are consistent with similar studies involving intravenous injection of nanoparticles of various sizes[169].

Assessment of biocompatibility *in vivo*: pregnant mouse-maternal-fetal measures, MRI, cytokine/ROS assays

A pregnant mouse model is favorable for studies of *in vivo* biocompatibility for a myriad of reasons. First, it allows for multigenerational studies of exposure (mothers versus pups), and with a 21 day gestation, data is acquired rapidly. Additionally the large litter size (6-8 pups or more) allows for different assays to be carried out on multiple individuals within one litter. To that end, a number of gravid mice were injected with 1 mg PEG-CF$_3$-TRITC-Gd$_2$O$_3$-MSN particles, or saline as a control, at varying points during gestation: early/mid gestation (6-9 days), or late gestation (15-16 days). Throughout gestation, the maternal body weights were monitored, and the fetuses and placentas were scanned with MRI and ultrasound imaging. On gestation day 16-17, the mothers were sacrificed, and the weights of the maternal organs, as well as the fetal/placental weights and crown-rump lengths of each fetus were measured. Thus far I have seen no significant differences in maternal weight during gestation, or in maternal organs after sacrifice and necropsy. After the dissection of fetuses and placentas, a

number of spontaneous resorptions and/or underdeveloped fetuses were observed, though neither the proportion of these events nor the litter sizes were found to be significantly different in MSN-exposed mice relative to controls.

Thus far, the majority of data involving weights of maternal organs and fetuses do not show evidence of an adverse reaction to MSN. To further support our hypothesis, maternal BAL fluid and serum were collected at the time of necropsy and tested for an array of inflammatory cytokines and reactive oxygen species/reactive nitrogen species. The only cytokine tested for which showed a significantly different concentration in MSN-exposed mice relative to controls was granulocyte-colony stimulating factor (G-CSF), and only in mice injected during late gestation. An elevated level of G-CSF in MSN-exposed animals is expected, as G-CSF is a known stimulator of the production of neutrophils, which clear various debris from tissue.

Table A1: Timeline of observations in immortalization of mesenchymal stem cells

d.i.v.	Observation (% confluence)	Action
0		Fetal Bone Marrow specimen collected onto 3-60 mm dishes
1		Removed non-adherent cells
4	20% confluence	half-medium change on all 3 dishes (DMEM+10%fbs)
5	35% confluence	Wright's stain on non-adherent cells
		Immune labeling for STRO-1 on treated coverslips (experiment IF009)
		Day one of infection protocol
6		Day two of infection protocol
		half-medium change on uninfected cells (DMEM+10%fbs)
8	All 3 dishes look the same; 50% confluence	half-medium change on all 3 dishes (DMEM+10%fbs)
11	All 3 dishes look the same; 70% confluence	half-medium change on all 3 dishes (DMEM+10%fbs)
13	All 3 dishes look the same; 90% confluence	half-medium change on all 3 dishes (DMEM+10%fbs)
15	All 3 dishes of cells are confluent	trypsinized, seeded onto 100 mm dishes
18	Infected 30%, uninfected 50%; all bipolar	half-medium change on all 3 dishes (DMEM+10%fbs)
20	Infected 40%, uninfected 80%; all bipolar	half-medium change on all 3 dishes (DMEM+10%fbs)

Table A1, continued

22	Infected 50%, uninfected 100%; all bipolar	uninfected cells trypsinized, seeded onto 2-100 mm dishes
25	Both infected cells 50% and flattening slightly	Trypsinized infected cells, moved from 100 mm dish to T25 flask
	uninfected cells 50% and flattening	half-medium change on uninfected cells (DMEM+10%fbs)
27	E6/E7 cells 50%, slightly less bipolar	half-medium change (DMEM+10%fbs)
	LXSN cells 50%, flatter than E6/E7	half-medium change (DMEM+10%fbs)
	Uninfected cells appearing senescent	half-medium change (DMEM+10%fbs)
29	E6/E7 cells 50%, still mostly bipolar	half-medium change (DMEM+10%fbs)
	LXSN cells 50%, flatter than E6/E7	half-medium change (DMEM+10%fbs)
	Uninfected cells fully senescent, many apoptotic bodies	*Discontinued uninfected cells*
32	E6/E7 cells 60%, still mostly bipolar	half-medium change (DMEM+10%fbs)
	LXSN cells 40%, some have detached from culture	half-medium change (DMEM+10%fbs)
34	E6/E7 cells 60%, still mostly bipolar	half-medium change (DMEM+10%fbs)
	LXSN cells 10%, nearly all have detached from culture	Added 1 mL DMEM+10%fbs
36	E6/E7 cells 70%, still mostly bipolar	half-medium change (DMEM+10%fbs)

Table A1, continued

	all LXSN cells have detached from culture	*Discontinued feedings*
38	E6/E7 cells 70%, still mostly bipolar, slow growth	Trypsinized E6/E7 cells, seeded on a new T25 flask
41	E6/E7 cells 60%, a mix of bipolar and flattened cells, slow growth	half-medium change (DMEM+10%fbs)
44	E6/E7 cells 60%, a mix of bipolar and flattened cells, slow growth	half-medium change (DMEM+10%fbs)
46	E6/E7 cells 60%, a mix of bipolar and flattened cells, slow growth	half-medium change (DMEM+10%fbs)
48	E6/E7 cells 70%, a mix of bipolar and flattened cells, slow growth	Trypsinized E6/E7 cells, seeded on a new T25 flask
50	E6/E7 cells 60%, a mix of bipolar and flattened cells, slow growth	half-medium change (MesenCult + mesenchymal supplement)
53	E6/E7 cells 70%, a mix of bipolar and flattened cells, slow growth	full-medium change (MesenCult + mesenchymal supplement)

REFERENCES

1. Roger, V. L.; Go, A. S.; Lloyd-Jones, D. M.; Adams, R. J.; Berry, J. D.; Brown, T. M.; Carnethon, M. R.; Dai, S.; de Simone, G.; Ford, E. S.; Fox, C. S.; Fullerton, H. J.; Gillespie, C.; Greenlund, K. J.; Hailpern, S. M.; Heit, J. A.; Ho, P. M.; Howard, V. J.; Kissela, B. M.; Kittner, S. J.; Lackland, D. T.; Lichtman, J. H.; Lisabeth, L. D.; Makuc, D. M.; Marcus, G. M.; Marelli, A.; Matchar, D. B.; McDermott, M. M.; Meigs, J. B.; Moy, C. S.; Mozaffarian, D.; Mussolino, M. E.; Nichol, G.; Paynter, N. P.; Rosamond, W. D.; Sorlie, P. D.; Stafford, R. S.; Turan, T. N.; Turner, M. B.; Wong, N. D.; Wylie-Rosett, J.; American Heart Association Statistics Committee and Stroke Statistics Subcommittee Heart disease and stroke statistics--2011 update: a report from the American Heart Association. *Circulation* **2011**, *123*, e18-e209.

2. Henning, R. J. Stem cells in cardiac repair. *Future Cardiol.* **2011**, *7*, 99-117.

3. Lalit, P. A.; Hei, D. J.; Raval, A. N.; Kamp, T. J. Induced pluripotent stem cells for post-myocardial infarction repair: remarkable opportunities and challenges. *Circ. Res.* **2014**, *114*, 1328-1345.

4. Clayton, Z. E.; Sadeghipour, S.; Patel, S. Generating induced pluripotent stem cell derived endothelial cells and induced endothelial cells for cardiovascular disease modelling and therapeutic angiogenesis. *Int. J. Cardiol.* **2015**, *197*, 116-122.

5. Koudstaal, S.; Jansen Of Lorkeers, S. J.; Gaetani, R.; Gho, J. M.; van Slochteren, F. J.; Sluijter, J. P.; Doevendans, P. A.; Ellison, G. M.; Chamuleau, S. A. Concise review: heart regeneration and the role of cardiac stem cells. *Stem Cells Transl. Med.* **2013**, *2*, 434-443.

6. Choi, Y. H.; Kurtz, A.; Stamm, C. Mesenchymal stem cells for cardiac cell therapy. *Hum. Gene Ther.* **2011**, *22*, 3-17.

7. Sutton, M. G.; Sharpe, N. Left ventricular remodeling after myocardial infarction: pathophysiology and therapy. *Circulation* **2000**, *101*, 2981-2988.

8. Zamilpa, R.; Navarro, M. M.; Flores, I.; Griffey, S. Stem cell mechanisms during left ventricular remodeling post-myocardial infarction: Repair and regeneration. *World J. Cardiol.* **2014**, *6*, 610-620.

9. Cutts, J.; Nikkhah, M.; Brafman, D. A. Biomaterial Approaches for Stem Cell-Based Myocardial Tissue Engineering. *Biomark Insights* **2015**, *10*, 77-90.

10. Pattanayak, P.; Bleumke, D. A. Tissue characterization of the myocardium: state of the art characterization by magnetic resonance and computed tomography imaging. *Radiol. Clin. North Am.* **2015**, *53*, 413-423.

11. Saeed, M.; Van, T. A.; Krug, R.; Hetts, S. W.; Wilson, M. W. Cardiac MR imaging: current status and future direction. *Cardiovasc. Diagn. Ther.* **2015***, 5*, 290-310.

12. Doppler, S. A.; Deutsch, M. A.; Lange, R.; Krane, M. Cardiac regeneration: current therapies-future concepts. *J. Thorac. Dis.* **2013***, 5*, 683-697.

13. Simmons, P. J.; Torok-Storb, B. Identification of stromal cell precursors in human bone marrow by a novel monoclonal antibody, STRO-1. *Blood* **1991***, 78*, 55-62.

14. Pittenger, M. F.; Mackay, A. M.; Beck, S. C.; Jaiswal, R. K.; Douglas, R.; Mosca, J. D.; Moorman, M. A.; Simonetti, D. W.; Craig, S.; Marshak, D. R. Multilineage potential of adult human mesenchymal stem cells. *Science* **1999***, 284*, 143-147.

15. Bartholomew, A.; Sturgeon, C.; Siatskas, M.; Ferrer, K.; McIntosh, K.; Patil, S.; Hardy, W.; Devine, S.; Ucker, D.; Deans, R.; Moseley, A.; Hoffman, R. Mesenchymal stem cells suppress lymphocyte proliferation in vitro and prolong skin graft survival in vivo. *Exp. Hematol.* **2002***, 30*, 42-48.

16. Di Nicola, M.; Carlo-Stella, C.; Magni, M.; Milanesi, M.; Longoni, P. D.; Matteucci, P.; Grisanti, S.; Gianni, A. M. Human bone marrow stromal cells suppress T-lymphocyte proliferation induced by cellular or nonspecific mitogenic stimuli. *Blood* **2002***, 99*, 3838-3843.

17. Le Blanc, K.; Tammik, C.; Rosendahl, K.; Zetterberg, E.; Ringden, O. HLA expression and immunologic properties of differentiated and undifferentiated mesenchymal stem cells. *Exp. Hematol.* **2003***, 31*, 890-896.

18. Tse, W. T.; Pendleton, J. D.; Beyer, W. M.; Egalka, M. C.; Guinan, E. C. Suppression of allogeneic T-cell proliferation by human marrow stromal cells: implications in transplantation. *Transplantation* **2003***, 75*, 389-397.

19. Rasmusson, I. Immune modulation by mesenchymal stem cells. *Exp. Cell Res.* **2006***, 312*, 2169-2179.

20. Le Blanc, K.; Ringden, O. Immunomodulation by mesenchymal stem cells and clinical experience. *J. Intern. Med.* **2007***, 262*, 509-525.

21. Nauta, A. J.; Fibbe, W. E. Immunomodulatory properties of mesenchymal stromal cells. *Blood* **2007***, 110*, 3499-3506.

22. Atoui, R.; Shum-Tim, D.; Chiu, R. C. Myocardial regenerative therapy: immunologic basis for the potential "universal donor cells". *Ann. Thorac. Surg.* **2008***, 86*, 327-334.

23. Comite, P.; Cobianchi, L.; Avanzini, M. A.; Mantelli, M.; Achille, V.; Zonta, S.; Ferrari, C.; Alessiani, M.; De Silvestri, A.; Gandolfo, G. M.; Inverardi, L.; Brescia, L.; Pietrabissa, A.; Dionigi, P.; Locatelli, F.; Bernardo, M. E. Immunomodulatory properties of porcine, bone marrow-derived multipotent mesenchymal stromal cells and comparison with their human counterpart. *Cell. Mol. Biol. (Noisy-le-grand)* **2011**, *57 Suppl*, OL1600-5.

24. Kim, J.; Breunig, M. J.; Escalante, L. E.; Bhatia, N.; Denu, R. A.; Dollar, B. A.; Stein, A. P.; Hanson, S. E.; Naderi, N.; Radek, J.; Haughy, D.; Bloom, D. D.; Assadi-Porter, F. M.; Hematti, P. Biologic and immunomodulatory properties of mesenchymal stromal cells derived from human pancreatic islets. *Cytotherapy* **2012**, *14*, 925-935.

25. Eliopoulos, N.; Stagg, J.; Lejeune, L.; Pommey, S.; Galipeau, J. Allogeneic marrow stromal cells are immune rejected by MHC class I- and class II-mismatched recipient mice. *Blood* **2005**, *106*, 4057-4065.

26. Nauta, A. J.; Westerhuis, G.; Kruisselbrink, A. B.; Lurvink, E. G.; Willemze, R.; Fibbe, W. E. Donor-derived mesenchymal stem cells are immunogenic in an allogeneic host and stimulate donor graft rejection in a nonmyeloablative setting. *Blood* **2006**, *108*, 2114-2120.

27. Stagg, J.; Pommey, S.; Eliopoulos, N.; Galipeau, J. Interferon-gamma-stimulated marrow stromal cells: a new type of nonhematopoietic antigen-presenting cell. *Blood* **2006**, *107*, 2570-2577.

28. Teng, C. J.; Luo, J.; Chiu, R. C.; Shum-Tim, D. Massive mechanical loss of microspheres with direct intramyocardial injection in the beating heart: implications for cellular cardiomyoplasty. *J. Thorac. Cardiovasc. Surg.* **2006**, *132*, 628-632.

29. Zhuo, Y.; Li, S. H.; Chen, M. S.; Wu, J.; Kinkaid, H. Y.; Fazel, S.; Weisel, R. D.; Li, R. K. Aging impairs the angiogenic response to ischemic injury and the activity of implanted cells: combined consequences for cell therapy in older recipients. *J. Thorac. Cardiovasc. Surg.* **2010**, *139*, 1286-94, 1294.e1-2.

30. Nayan, M.; Paul, A.; Chen, G.; Chiu, R. C.; Prakash, S.; Shum-Tim, D. Superior therapeutic potential of young bone marrow mesenchymal stem cells by direct intramyocardial delivery in aged recipients with acute myocardial infarction: in vitro and in vivo investigation. *J. Tissue Eng.* **2011**, *2011*, 741213.

31. Beltrami, A. P.; Barlucchi, L.; Torella, D.; Baker, M.; Limana, F.; Chimenti, S.; Kasahara, H.; Rota, M.; Musso, E.; Urbanek, K.; Leri, A.; Kajstura, J.; Nadal-Ginard, B.; Anversa, P. Adult cardiac stem cells are multipotent and support myocardial regeneration. *Cell* **2003**, *114*, 763-776.

32. Hou, M.; Yang, K. M.; Zhang, H.; Zhu, W. Q.; Duan, F. J.; Wang, H.; Song, Y. H.; Wei, Y. J.; Hu, S. S. Transplantation of mesenchymal stem cells from human bone marrow improves damaged heart function in rats. *Int. J. Cardiol.* **2007***, 115*, 220-228.

33. Hida, N.; Nishiyama, N.; Miyoshi, S.; Kira, S.; Segawa, K.; Uyama, T.; Mori, T.; Miyado, K.; Ikegami, Y.; Cui, C.; Kiyono, T.; Kyo, S.; Shimizu, T.; Okano, T.; Sakamoto, M.; Ogawa, S.; Umezawa, A. Novel cardiac precursor-like cells from human menstrual blood-derived mesenchymal cells. *Stem Cells* **2008***, 26*, 1695-1704.

34. Grinnemo, K. H.; Mansson-Broberg, A.; Leblanc, K.; Corbascio, M.; Wardell, E.; Siddiqui, A. J.; Hao, X.; Sylven, C.; Dellgren, G. Human mesenchymal stem cells do not differentiate into cardiomyocytes in a cardiac ischemic xenomodel. *Ann. Med.* **2006***, 38*, 144-153.

35. Katritsis, D. G.; Sotiropoulou, P. A.; Karvouni, E.; Karabinos, I.; Korovesis, S.; Perez, S. A.; Voridis, E. M.; Papamichail, M. Transcoronary transplantation of autologous mesenchymal stem cells and endothelial progenitors into infarcted human myocardium. *Catheter. Cardiovasc. Interv.* **2005***, 65*, 321-329.

36. Anonymous Demand for Imaging in Healthcare Drives Sales of Imaging Agents. *http://www.kaloramainformation.com/about/release.asp?id=2994* (accessed 10/12, 2012).

37. Webster, J. G.; Clark, J. W., Eds.; In *Medical Instrumentation: Application and Design;* Wiley: New York, 1998; Vol. 3rd ed.

38. Chelliah, R. K.; Senior, R. Contrast echocardiography: an update. *Curr. Cardiol. Rep.* **2009***, 11*, 216-224.

39. Hobbs, S. K.; Monsky, W. L.; Yuan, F.; Roberts, W. G.; Griffith, L.; Torchilin, V. P.; Jain, R. K. Regulation of transport pathways in tumor vessels: role of tumor type and microenvironment. *Proc. Natl. Acad. Sci. U. S. A.* **1998***, 95*, 4607-4612.

40. Perera, R. H.; Hernandez, C.; Zhou, H.; Kota, P.; Burke, A.; Exner, A. A. Ultrasound imaging beyond the vasculature with new generation contrast agents. *Wiley Interdiscip. Rev. Nanomed Nanobiotechnol* **2015***, 7*, 593-608.

41. Casciaro, S.; Conversano, F.; Ragusa, A.; Malvindi, M. A.; Franchini, R.; Greco, A.; Pellegrino, T.; Gigli, G. Optimal enhancement configuration of silica nanoparticles for ultrasound imaging and automatic detection at conventional diagnostic frequencies. *Invest. Radiol.* **2010***, 45*, 715-724.

42. Milgroom, A.; Intrator, M.; Madhavan, K.; Mazzaro, L.; Shandas, R.; Liu, B.; Park, D. Mesoporous silica nanoparticles as a breast-cancer targeting ultrasound contrast agent. *Colloids Surf. B Biointerfaces* **2014***, 116*, 652-657.

43. Bara, C.; Ghodsizad, A.; Niehaus, M.; Makoui, M.; Piechaczek, C.; Martin, U.; Warnecke, G.; Karck, M.; Gams, E.; Klein, H. M.; Haverich, A.; Ruhparwar, A. In vivo echocardiographic imaging of transplanted human adult stem cells in the myocardium labeled with clinically applicable CliniMACS nanoparticles. *J. Am. Soc. Echocardiogr.* **2006***, 19*, 563-568.

44. Mallidi, S.; Joshi, P. P.; Sokolov, K.; Emelianov, S. On sensitivity of molecular specific photoacoustic imaging using plasmonic gold nanoparticles. *Conf. Proc. IEEE Eng. Med. Biol. Soc.* **2009***, 2009*, 6338-6340.

45. Abbott, J. G.; Thurstone, F. L. Acoustic speckle: theory and experimental analysis. *Ultrason. Imaging* **1979***, 1*, 303-324.

46. Liang, Z.; Lauterbur, P. C.; IEEE Engineering in Medicine and Biology Society *Principles of magnetic resonance imaging : a signal processing perspective;* IEEE Press series in biomedical engineering; SPIE Optical Engineering Press ;New York: Bellingham, Wash., 2000; , pp 416.

47. Lauffer, R. B. Paramagnetic metal complexes as water proton relaxation agents for NMR imaging: theory and design. *Chem. Rev.* **1987***, 87*, 901-927.

48. Rohrer, M.; Bauer, H.; Mintorovitch, J.; Requardt, M.; Weinmann, H. J. Comparison of magnetic properties of MRI contrast media solutions at different magnetic field strengths. *Invest. Radiol.* **2005***, 40*, 715-724.

49. Deloison, B.; Siauve, N.; Aimot, S.; Balvay, D.; Thiam, R.; Cuenod, C. A.; Ville, Y.; Clement, O.; Salomon, L. J. SPIO-enhanced magnetic resonance imaging study of placental perfusion in a rat model of intrauterine growth restriction. *BJOG* **2012***, 119*, 626-633.

50. Huang, C.; Neoh, K. G.; Xu, L.; Kang, E. T.; Chiong, E. Polymeric nanoparticles with encapsulated superparamagnetic iron oxide and conjugated cisplatin for potential bladder cancer therapy. *Biomacromolecules* **2012***, 13*, 2513-2520.

51. Lee, M. J.; Kim, M. J.; Yoon, C. S.; Song, S. Y.; Park, K.; Kim, W. S. The T2-shortening effect of gadolinium and the optimal conditions for maximizing the CNR for evaluating the biliary system: a phantom study. *Korean J. Radiol.* **2011***, 12*, 358-364.

52. Park, J. Y.; Baek, M. J.; Choi, E. S.; Woo, S.; Kim, J. H.; Kim, T. J.; Jung, J. C.; Chae, K. S.; Chang, Y.; Lee, G. H. Paramagnetic ultrasmall gadolinium oxide nanoparticles as advanced T1 MRI contrast agent: account for large longitudinal relaxivity, optimal particle diameter, and in vivo T1 MR images. *ACS Nano* **2009***, 3*, 3663-3669.

53. Faucher, L.; Tremblay, M.; Lagueux, J.; Gossuin, Y.; Fortin, M. A. Rapid synthesis of PEGylated ultrasmall gadolinium oxide nanoparticles for cell labeling and tracking with MRI. *ACS Appl. Mater. Interfaces* **2012***, 4*, 4506-4515.

54. Hedlund, A.; Ahren, M.; Gustafsson, H.; Abrikossova, N.; Warntjes, M.; Jonsson, J. I.; Uvdal, K.; Engstrom, M. Gd(2)O(3) nanoparticles in hematopoietic cells for MRI contrast enhancement. *Int. J. Nanomedicine* **2011***, 6*, 3233-3240.

55. Yu, S. B.; Watson, A. D. Metal-Based X-ray Contrast Media. *Chem. Rev.* **1999***, 99*, 2353-2378.

56. Hainfeld, J. F.; Slatkin, D. N.; Focella, T. M.; Smilowitz, H. M. Gold nanoparticles: a new X-ray contrast agent. *Br. J. Radiol.* **2006***, 79*, 248-253.

57. Rabin, O.; Manuel Perez, J.; Grimm, J.; Wojtkiewicz, G.; Weissleder, R. An X-ray computed tomography imaging agent based on long-circulating bismuth sulphide nanoparticles. *Nat. Mater.* **2006***, 5*, 118-122.

58. Cormode, D. P.; Skajaa, T.; van Schooneveld, M. M.; Koole, R.; Jarzyna, P.; Lobatto, M. E.; Calcagno, C.; Barazza, A.; Gordon, R. E.; Zanzonico, P.; Fisher, E. A.; Fayad, Z. A.; Mulder, W. J. Nanocrystal core high-density lipoproteins: a multimodality contrast agent platform. *Nano Lett.* **2008***, 8*, 3715-3723.

59. Cormode, D. P.; Jarzyna, P. A.; Mulder, W. J.; Fayad, Z. A. Modified natural nanoparticles as contrast agents for medical imaging. *Adv. Drug Deliv. Rev.* **2010***, 62*, 329-338.

60. Van Unnik, J. G.; Broerse, J. J.; Geleijns, J.; Jansen, J. T.; Zoetelief, J.; Zweers, D. Survey of CT techniques and absorbed dose in various Dutch hospitals. *Br. J. Radiol.* **1997***, 70*, 367-371.

61. Brenner, D. J.; Hall, E. J. Computed tomography--an increasing source of radiation exposure. *N. Engl. J. Med.* **2007***, 357*, 2277-2284.

62. Carlson, N. R. *Physiology of Behavior 11th Edition;* Pearson: 2012; .

63. Biersack, H. J.; Freeman, L. M., Eds.; In *Clinical Nuclear Medicine, 1st Ed.* Springer-Verlag: Berlin Heidelberg, 2007; , pp 548.

64. Fu, Y.; Azene, N.; Xu, Y.; Kraitchman, D. L. Tracking stem cells for cardiovascular applications in vivo: focus on imaging techniques. *Imaging Med.* **2011**, *3*, 473-486.

65. Doyle, B.; Kemp, B. J.; Chareonthaitawee, P.; Reed, C.; Schmeckpeper, J.; Sorajja, P.; Russell, S.; Araoz, P.; Riederer, S. J.; Caplice, N. M. Dynamic tracking during intracoronary injection of 18F-FDG-labeled progenitor cell therapy for acute myocardial infarction. *J. Nucl. Med.* **2007**, *48*, 1708-1714.

66. Kim, M. H.; Woo, S. K.; Lee, K. C.; An, G. I.; Pandya, D.; Park, N. W.; Nahm, S. S.; Eom, K. D.; Kim, K. I.; Lee, T. S.; Kim, C. W.; Kang, J. H.; Yoo, J.; Lee, Y. J. Longitudinal monitoring adipose-derived stem cell survival by PET imaging hexadecyl-4-(1)(2)(4)I-iodobenzoate in rat myocardial infarction model. *Biochem. Biophys. Res. Commun.* **2015**, *456*, 13-19.

67. Lakowicz, J. R. *Principles of Fluorescence Spectroscopy, 3rd Ed.* Springer-Verlag: U.S., 2006; , pp 954.

68. Huang, D. M.; Hung, Y.; Ko, B. S.; Hsu, S. C.; Chen, W. H.; Chien, C. L.; Tsai, C. P.; Kuo, C. T.; Kang, J. C.; Yang, C. S.; Mou, C. Y.; Chen, Y. C. Highly efficient cellular labeling of mesoporous nanoparticles in human mesenchymal stem cells: implication for stem cell tracking. *FASEB J.* **2005**, *19*, 2014-2016.

69. Knapp, D. W.; Adams, L. G.; Degrand, A. M.; Niles, J. D.; Ramos-Vara, J. A.; Weil, A. B.; O'Donnell, M. A.; Lucroy, M. D.; Frangioni, J. V. Sentinel lymph node mapping of invasive urinary bladder cancer in animal models using invisible light. *Eur. Urol.* **2007**, *52*, 1700-1708.

70. van Dam, G. M.; Themelis, G.; Crane, L. M.; Harlaar, N. J.; Pleijhuis, R. G.; Kelder, W.; Sarantopoulos, A.; de Jong, J. S.; Arts, H. J.; van der Zee, A. G.; Bart, J.; Low, P. S.; Ntziachristos, V. Intraoperative tumor-specific fluorescence imaging in ovarian cancer by folate receptor-alpha targeting: first in-human results. *Nat. Med.* **2011**, *17*, 1315-1319.

71. Derfus, A. M.; Chan, W. C. W.; Bhatia, S. N. Probing the Cytotoxicity of Semiconductor Quantum Dots. *Nano Lett.* **2004**, *4*, 11-18.

72. Shiohara, A.; Hoshino, A.; Hanaki, K.; Suzuki, K.; Yamamoto, K. On the cyto-toxicity caused by quantum dots. *Microbiol. Immunol.* **2004**, *48*, 669-675.

73. Kirchner, C.; Liedl, T.; Kudera, S.; Pellegrino, T.; Munoz Javier, A.; Gaub, H. E.; Stolzle, S.; Fertig, N.; Parak, W. J. Cytotoxicity of colloidal CdSe and CdSe/ZnS nanoparticles. *Nano Lett.* **2005**, *5*, 331-338.

74. Lovric, J.; Bazzi, H. S.; Cuie, Y.; Fortin, G. R.; Winnik, F. M.; Maysinger, D. Differences in subcellular distribution and toxicity of green and red emitting CdTe quantum dots. *J. Mol. Med. (Berl)* **2005**, *83*, 377-385.

75. Hardman, R. A toxicologic review of quantum dots: toxicity depends on physicochemical and environmental factors. *Environ. Health Perspect.* **2006**, *114*, 165-172.

76. Lai, C. Y.; Trewyn, B. G.; Jeftinija, D. M.; Jeftinija, K.; Xu, S.; Jeftinija, S.; Lin, V. S. A mesoporous silica nanosphere-based carrier system with chemically removable CdS nanoparticle caps for stimuli-responsive controlled release of neurotransmitters and drug molecules. *J. Am. Chem. Soc.* **2003**, *125*, 4451-4459.

77. Giri, S.; Trewyn, B. G.; Stellmaker, M. P.; Lin, V. S. Stimuli-responsive controlled-release delivery system based on mesoporous silica nanorods capped with magnetic nanoparticles. *Angew. Chem. Int. Ed Engl.* **2005**, *44*, 5038-5044.

78. Slowing, I.; Trewyn, B. G.; Lin, V. S. Effect of surface functionalization of MCM-41-type mesoporous silica nanoparticles on the endocytosis by human cancer cells. *J. Am. Chem. Soc.* **2006**, *128*, 14792-14793.

79. Slowing, I. I.; Trewyn, B. G.; Lin, V. S. Mesoporous silica nanoparticles for intracellular delivery of membrane-impermeable proteins. *J. Am. Chem. Soc.* **2007**, *129*, 8845-8849.

80. Zhao, Y.; Vivero-Escoto, J. L.; Slowing, I. I.; Trewyn, B. G.; Lin, V. S. Capped mesoporous silica nanoparticles as stimuli-responsive controlled release systems for intracellular drug/gene delivery. *Expert Opin. Drug Deliv.* **2010**, *7*, 1013-1029.

81. Zhao, Y.; Sun, X.; Zhang, G.; Trewyn, B. G.; Slowing, I. I.; Lin, V. S. Interaction of mesoporous silica nanoparticles with human red blood cell membranes: size and surface effects. *ACS Nano* **2011**, *5*, 1366-1375.

82. Valenstein, J. S.; Kandel, K.; Melcher, F.; Slowing, I. I.; Lin, V. S.; Trewyn, B. G. Functional mesoporous silica nanoparticles for the selective sequestration of free fatty acids from microalgal oil. *ACS Appl. Mater. Interfaces* **2012**, *4*, 1003-1009.

83. Makino, S.; Fukuda, K.; Miyoshi, S.; Konishi, F.; Kodama, H.; Pan, J.; Sano, M.; Takahashi, T.; Hori, S.; Abe, H.; Hata, J.; Umezawa, A.; Ogawa, S. Cardiomyocytes can be generated from marrow stromal cells in vitro. *J. Clin. Invest.* **1999**, *103*, 697-705.

84. Fukuda, K. Development of regenerative cardiomyocytes from mesenchymal stem cells for cardiovascular tissue engineering. *Artif. Organs* **2001**, *25*, 187-193.

85. Shim, W. S.; Jiang, S.; Wong, P.; Tan, J.; Chua, Y. L.; Tan, Y. S.; Sin, Y. K.; Lim, C. H.; Chua, T.; Teh, M.; Liu, T. C.; Sim, E. Ex vivo differentiation of human adult bone marrow stem cells into cardiomyocyte-like cells. *Biochem. Biophys. Res. Commun.* **2004**, *324*, 481-488.

86. Xu, W.; Zhang, X.; Qian, H.; Zhu, W.; Sun, X.; Hu, J.; Zhou, H.; Chen, Y. Mesenchymal stem cells from adult human bone marrow differentiate into a cardiomyocyte phenotype in vitro. *Exp. Biol. Med. (Maywood)* **2004***, 229*, 623-631.

87. Balana, B.; Nicoletti, C.; Zahanich, I.; Graf, E. M.; Christ, T.; Boxberger, S.; Ravens, U. 5-Azacytidine induces changes in electrophysiological properties of human mesenchymal stem cells. *Cell Res.* **2006***, 16*, 949-960.

88. Kadivar, M.; Khatami, S.; Mortazavi, Y.; Shokrgozar, M. A.; Taghikhani, M.; Soleimani, M. In vitro cardiomyogenic potential of human umbilical vein-derived mesenchymal stem cells. *Biochem. Biophys. Res. Commun.* **2006***, 340*, 639-647.

89. Sen, A.; Miller, J. C.; Reynolds, R.; Willerson, J. T.; Buja, L. M.; Chien, K. R. Inhibition of the release of arachidonic acid prevents the development of sarcolemmal membrane defects in cultured rat myocardial cells during adenosine triphosphate depletion. *J. Clin. Invest.* **1988***, 82*, 1333-1338.

90. Maass, A. H.; Buvoli, M. Cardiomyocyte preparation, culture, and gene transfer. *Methods Mol. Biol.* **2007***, 366*, 321-330.

91. de Haas, H. J.; Arbustini, E.; Fuster, V.; Kramer, C. M.; Narula, J. Molecular imaging of the cardiac extracellular matrix. *Circ. Res.* **2014***, 114*, 903-915.

92. Toma, C.; Pittenger, M. F.; Cahill, K. S.; Byrne, B. J.; Kessler, P. D. Human mesenchymal stem cells differentiate to a cardiomyocyte phenotype in the adult murine heart. *Circulation* **2002***, 105*, 93-98.

93. Fujita, J.; Hemmi, N.; Tohyama, S.; Seki, T.; Tamura, Y.; Fukuda, K. Practical Applications of Confocal Laser Scanning Microscopy for Cardiac Regenerative Medicine. In *Confocal Laser Microscopy: Principles and Applications in Medicine, Biology, and the Food Sciences*; Lagali, N., Ed.; InTech: Rijeka, Croatia, 2013; pp 1.

94. Lian, X.; Zhang, J.; Azarin, S. M.; Zhu, K.; Hazeltine, L. B.; Bao, X.; Hsiao, C.; Kamp, T. J.; Palecek, S. P. Directed cardiomyocyte differentiation from human pluripotent stem cells by modulating Wnt/beta-catenin signaling under fully defined conditions. *Nat. Protoc.* **2013***, 8*, 162-175.

95. Li, X.; Yu, X.; Lin, Q.; Deng, C.; Shan, Z.; Yang, M.; Lin, S. Bone marrow mesenchymal stem cells differentiate into functional cardiac phenotypes by cardiac microenvironment. *J. Mol. Cell. Cardiol.* **2007***, 42*, 295-303.

96. Ma, J.; Guo, L.; Fiene, S. J.; Anson, B. D.; Thomson, J. A.; Kamp, T. J.; Kolaja, K. L.; Swanson, B. J.; January, C. T. High purity human-induced pluripotent stem cell-derived cardiomyocytes: electrophysiological properties of action potentials and ionic currents. *Am. J. Physiol. Heart Circ. Physiol.* **2011***, 301*, H2006-17.

97. Torney, F.; Trewyn, B. G.; Lin, V. S.; Wang, K. Mesoporous silica nanoparticles deliver DNA and chemicals into plants. *Nat. Nanotechnol* **2007**, *2*, 295-300.

98. Francis, J.; Weiss, R. M.; Wei, S. G.; Johnson, A. K.; Felder, R. B. Progression of heart failure after myocardial infarction in the rat. *Am. J. Physiol. Regul. Integr. Comp. Physiol.* **2001**, *281*, R1734-45.

99. Francis, J.; Zhang, Z. H.; Weiss, R. M.; Felder, R. B. Neural regulation of the proinflammatory cytokine response to acute myocardial infarction. *Am. J. Physiol. Heart Circ. Physiol.* **2004**, *287*, H791-7.

100. Lei, L.; Zhou, R.; Zheng, W.; Christensen, L. P.; Weiss, R. M.; Tomanek, R. J. Bradycardia induces angiogenesis, increases coronary reserve, and preserves function of the postinfarcted heart. *Circulation* **2004**, *110*, 796-802.

101. Miller, J. D.; Peotta, V. A.; Chu, Y.; Weiss, R. M.; Zimmerman, K.; Brooks, R. M.; Heistad, D. D. MnSOD protects against COX1-mediated endothelial dysfunction in chronic heart failure. *Am. J. Physiol. Heart Circ. Physiol.* **2010**, *298*, H1600-7.

102. Zell, K.; Sperl, J. I.; Vogel, M. W.; Niessner, R.; Haisch, C. Acoustical properties of selected tissue phantom materials for ultrasound imaging. *Phys. Med. Biol.* **2007**, *52*, N475-84.

103. Demitri, C.; Sannino, A.; Conversano, F.; Casciaro, S.; Distante, A.; Maffezzoli, A. Hydrogel based tissue mimicking phantom for in-vitro ultrasound contrast agents studies. *J. Biomed. Mater. Res. B. Appl. Biomater.* **2008**, *87*, 338-345.

104. Culjat, M. O.; Goldenberg, D.; Tewari, P.; Singh, R. S. A review of tissue substitutes for ultrasound imaging. *Ultrasound Med. Biol.* **2010**, *36*, 861-873.

105. Nakano, A.; Nakano, H.; Chien, K. R. Multipotent islet-1 cardiovascular progenitors in development and disease. *Cold Spring Harb. Symp. Quant. Biol.* **2008**, *73*, 297-306.

106. Bu, L.; Jiang, X.; Martin-Puig, S.; Caron, L.; Zhu, S.; Shao, Y.; Roberts, D. J.; Huang, P. L.; Domian, I. J.; Chien, K. R. Human ISL1 heart progenitors generate diverse multipotent cardiovascular cell lineages. *Nature* **2009**, *460*, 113-117.

107. Garry, D. J.; Olson, E. N. A common progenitor at the heart of development. *Cell* **2006**, *127*, 1101-1104.

108. Moretti, A.; Caron, L.; Nakano, A.; Lam, J. T.; Bernshausen, A.; Chen, Y.; Qyang, Y.; Bu, L.; Sasaki, M.; Martin-Puig, S.; Sun, Y.; Evans, S. M.; Laugwitz, K. L.; Chien, K. R. Multipotent embryonic isl1+ progenitor cells lead to cardiac, smooth muscle, and endothelial cell diversification. *Cell* **2006**, *127*, 1151-1165.

109. Laugwitz, K. L.; Moretti, A.; Lam, J.; Gruber, P.; Chen, Y.; Woodard, S.; Lin, L. Z.; Cai, C. L.; Lu, M. M.; Reth, M.; Platoshyn, O.; Yuan, J. X.; Evans, S.; Chien, K. R. Postnatal isl1+ cardioblasts enter fully differentiated cardiomyocyte lineages. *Nature* **2005***, 433*, 647-653.

110. Chien, K. R.; Domian, I. J.; Parker, K. K. Cardiogenesis and the complex biology of regenerative cardiovascular medicine. *Science* **2008***, 322*, 1494-1497.

111. Youssoufian, H.; McAfee, M.; Kwiatkowski, D. J. Cloning and chromosomal localization of the human cytoskeletal alpha-actinin gene reveals linkage to the beta-spectrin gene. *Am. J. Hum. Genet.* **1990***, 47*, 62-72.

112. Ogneva, I. V.; Biryukov, N. S.; Leinsoo, T. A.; Larina, I. M. Possible role of non-muscle alpha-actinins in muscle cell mechanosensitivity. *PLoS One* **2014***, 9*, e96395.

113. Hamill, K. J.; Hiroyasu, S.; Colburn, Z. T.; Ventrella, R. V.; Hopkinson, S. B.; Skalli, O.; Jones, J. C. Alpha actinin-1 regulates cell-matrix adhesion organization in keratinocytes: consequences for skin cell motility. *J. Invest. Dermatol.* **2015***, 135*, 1043-1052.

114. Leger, J. J.; Berson, G.; Delcaryre, C.; Klotz, C.; Schwartz, K.; Leger, J.; Stephens, M.; Swynghedauw, B. Heart contractile proteins. *Biochimie* **1975***, 57*, 1249-1273.

115. Chiu, C.; Bagnall, R. D.; Ingles, J.; Yeates, L.; Kennerson, M.; Donald, J. A.; Jormakka, M.; Lind, J. M.; Semsarian, C. Mutations in alpha-actinin-2 cause hypertrophic cardiomyopathy: a genome-wide analysis. *J. Am. Coll. Cardiol.* **2010***, 55*, 1127-1135.

116. Seidman, C. E.; Seidman, J. G. Identifying sarcomere gene mutations in hypertrophic cardiomyopathy: a personal history. *Circ. Res.* **2011***, 108*, 743-750.

117. Fukuda, K.; Fujita, J. Mesenchymal, but not hematopoietic, stem cells can be mobilized and differentiate into cardiomyocytes after myocardial infarction in mice. *Kidney Int.* **2005***, 68*, 1940-1943.

118. Citro, L.; Naidu, S.; Hassan, F.; Kuppusamy, M. L.; Kuppusamy, P.; Angelos, M. G.; Khan, M. Comparison of human induced pluripotent stem-cell derived cardiomyocytes with human mesenchymal stem cells following acute myocardial infarction. *PLoS One* **2014***, 9*, e116281.

119. Fang, Y. B.; Liu, X.; Wen, J.; Tang, X. J.; Yu, F. X.; Deng, M. B.; Wu, C. X.; Liao, B. Differentiation induction of mouse cardiac stem cells into sinus node-like cells by co-culturing with sinus node. *Int. J. Clin. Exp. Pathol.* **2014***, 7*, 1868-1879.

120. Klabunde, R. E. *Cardiovascular Physiology Concepts, 2nd Ed.* Wolters Kluwer-Lippincott Williams & Wilkins: Philadelphia, 2011; .

121. Robinson, B. F.; Epstein, S. E.; Beiser, G. D.; Braunwald, E. Control of heart rate by the autonomic nervous system. Studies in man on the interrelation between baroreceptor mechanisms and exercise. *Circ. Res.* **1966***, 19*, 400-411.

122. Eschenhagen, T.; Didie, M.; Heubach, J.; Ravens, U.; Zimmermann, W. H. Cardiac tissue engineering. *Transpl. Immunol.* **2002***, 9*, 315-321.

123. Tao, Z. W.; Mohamed, M.; Hogan, M.; Gutierrez, L.; Birla, R. K. Optimizing a spontaneously contracting heart tissue patch with rat neonatal cardiac cells on fibrin gel. *J. Tissue Eng. Regen. Med.* **2014**.

124. Vidyasekar, P.; Shyamsunder, P.; Santhakumar, R.; Arun, R.; Verma, R. S. A simplified protocol for the isolation and culture of cardiomyocytes and progenitor cells from neonatal mouse ventricles. *Eur. J. Cell Biol.* **2015**.

125. Mummery, C.; Ward-van Oostwaard, D.; Doevendans, P.; Spijker, R.; van den Brink, S.; Hassink, R.; van der Heyden, M.; Opthof, T.; Pera, M.; de la Riviere, A. B.; Passier, R.; Tertoolen, L. Differentiation of human embryonic stem cells to cardiomyocytes: role of coculture with visceral endoderm-like cells. *Circulation* **2003***, 107*, 2733-2740.

126. Shintani, S. A.; Oyama, K.; Kobirumaki-Shimozawa, F.; Ohki, T.; Ishiwata, S.; Fukuda, N. Sarcomere length nanometry in rat neonatal cardiomyocytes expressed with alpha-actinin-AcGFP in Z discs. *J. Gen. Physiol.* **2014***, 143*, 513-524.

127. Kleber, A. G. The shape of the electrical action-potential upstroke: a new aspect from optical measurements on the surface of the heart. *Circ. Res.* **2005***, 97*, 204-206.

128. Halbert, C. L.; Demers, G. W.; Galloway, D. A. The E6 and E7 genes of human papillomavirus type 6 have weak immortalizing activity in human epithelial cells. *J. Virol.* **1992***, 66*, 2125-2134.

129. Zabner, J.; Karp, P.; Seiler, M.; Phillips, S. L.; Mitchell, C. J.; Saavedra, M.; Welsh, M.; Klingelhutz, A. J. Development of cystic fibrosis and noncystic fibrosis airway cell lines. *Am. J. Physiol. Lung Cell. Mol. Physiol.* **2003***, 284*, L844-54.

130. Jeong Seo, E.; Jung Kim, H.; Jae Lee, C.; Tae Kang, H.; Seong Hwang, E. The role of HPV oncoproteins and cellular factors in maintenance of hTERT expression in cervical carcinoma cells. *Gynecol. Oncol.* **2004***, 94*, 40-47.

131. Narisawa-Saito, M.; Yoshimatsu, Y.; Ohno, S.; Yugawa, T.; Egawa, N.; Fujita, M.; Hirohashi, S.; Kiyono, T. An in vitro multistep carcinogenesis model for human cervical cancer. *Cancer Res.* **2008***, 68*, 5699-5705.

132. Kiyono, T.; Foster, S. A.; Koop, J. I.; McDougall, J. K.; Galloway, D. A.; Klingelhutz, A. J. Both Rb/p16INK4a inactivation and telomerase activity are required to immortalize human epithelial cells. *Nature* **1998**, *396*, 84-88.

133. DeHoratius, D. M.; Cowper, S. E. Nephrogenic systemic fibrosis: an emerging threat among renal patients. *Semin. Dial.* **2006**, *19*, 191-194.

134. Idee, J. M.; Fretellier, N.; Robic, C.; Corot, C. The role of gadolinium chelates in the mechanism of nephrogenic systemic fibrosis: A critical update. *Crit. Rev. Toxicol.* **2014**, *44*, 895-913.

135. Haneder, S.; Kucharczyk, W.; Schoenberg, S. O.; Michaely, H. J. Safety of magnetic resonance contrast media: a review with special focus on nephrogenic systemic fibrosis. *Top. Magn. Reson. Imaging* **2015**, *24*, 57-65.

136. Crich, S. G.; Biancone, L.; Cantaluppi, V.; Duo, D.; Esposito, G.; Russo, S.; Camussi, G.; Aime, S. Improved route for the visualization of stem cells labeled with a Gd-/Eu-chelate as dual (MRI and fluorescence) agent. *Magn. Reson. Med.* **2004**, *51*, 938-944.

137. Groman, E. V.; Bouchard, J. C.; Reinhardt, C. P.; Vaccaro, D. E. Ultrasmall mixed ferrite colloids as multidimensional magnetic resonance imaging, cell labeling, and cell sorting agents. *Bioconjug. Chem.* **2007**, *18*, 1763-1771.

138. Daldrup-Link, H. E.; Rudelius, M.; Oostendorp, R. A.; Settles, M.; Piontek, G.; Metz, S.; Rosenbrock, H.; Keller, U.; Heinzmann, U.; Rummeny, E. J.; Schlegel, J.; Link, T. M. Targeting of hematopoietic progenitor cells with MR contrast agents. *Radiology* **2003**, *228*, 760-767.

139. Daldrup-Link, H. E.; Rudelius, M.; Oostendorp, R. A.; Jacobs, V. R.; Simon, G. H.; Gooding, C.; Rummeny, E. J. Comparison of iron oxide labeling properties of hematopoietic progenitor cells from umbilical cord blood and from peripheral blood for subsequent in vivo tracking in a xenotransplant mouse model XXX. *Acad. Radiol.* **2005**, *12*, 502-510.

140. Daldrup-Link, H. E.; Rudelius, M.; Piontek, G.; Metz, S.; Brauer, R.; Debus, G.; Corot, C.; Schlegel, J.; Link, T. M.; Peschel, C.; Rummeny, E. J.; Oostendorp, R. A. Migration of iron oxide-labeled human hematopoietic progenitor cells in a mouse model: in vivo monitoring with 1.5-T MR imaging equipment. *Radiology* **2005**, *234*, 197-205.

141. Jendelova, P.; Herynek, V.; Urdzikova, L.; Glogarova, K.; Kroupova, J.; Andersson, B.; Bryja, V.; Burian, M.; Hajek, M.; Sykova, E. Magnetic resonance tracking of transplanted bone marrow and embryonic stem cells labeled by iron oxide nanoparticles in rat brain and spinal cord. *J. Neurosci. Res.* **2004**, *76*, 232-243.

142. Bridot, J. L.; Faure, A. C.; Laurent, S.; Riviere, C.; Billotey, C.; Hiba, B.; Janier, M.; Josserand, V.; Coll, J. L.; Elst, L. V.; Muller, R.; Roux, S.; Perriat, P.; Tillement, O. Hybrid gadolinium oxide nanoparticles: multimodal contrast agents for in vivo imaging. *J. Am. Chem. Soc.* **2007**, *129*, 5076-5084.

143. Salvado, O.; Hillenbrand, C.; Zhang, S.; Wilson, D. L. Method to correct intensity inhomogeneity in MR images for atherosclerosis characterization. *IEEE Trans. Med. Imaging* **2006**, *25*, 539-552.

144. Salvado, O.; Hillenbrand, C. M.; Wilson, D. L. Partial volume reduction by interpolation with reverse diffusion. *Int. J. Biomed. Imaging* **2006**, *2006*, 92092.

145. Larsson, M.; Larsson, M.; Oddo, L.; Margheritelli, S.; Paradossi, G.; Nowak, J.; Brodin, L. A.; Caidahl, K.; Bjallmark, A. Visualization of multimodal polymer-shelled contrast agents using ultrasound contrast sequences: an experimental study in a tissue mimicking flow phantom. *Cardiovasc. Ultrasound* **2013**, *11*, 33-7120-11-33.

146. Benezra, M.; Penate-Medina, O.; Zanzonico, P. B.; Schaer, D.; Ow, H.; Burns, A.; DeStanchina, E.; Longo, V.; Herz, E.; Iyer, S.; Wolchok, J.; Larson, S. M.; Wiesner, U.; Bradbury, M. S. Multimodal silica nanoparticles are effective cancer-targeted probes in a model of human melanoma. *J. Clin. Invest.* **2011**, *121*, 2768-2780.

147. Luo, T.; Huang, P.; Gao, G.; Shen, G.; Fu, S.; Cui, D.; Zhou, C.; Ren, Q. Mesoporous silica-coated gold nanorods with embedded indocyanine green for dual mode X-ray CT and NIR fluorescence imaging. *Opt. Express* **2011**, *19*, 17030-17039.

148. Lin, Y. S.; Abadeer, N.; Hurley, K. R.; Haynes, C. L. Ultrastable, redispersible, small, and highly organomodified mesoporous silica nanotherapeutics. *J. Am. Chem. Soc.* **2011**, *133*, 20444-20457.

149. Zhou, J.; Tan, S. H.; Nicolas, V.; Bauvy, C.; Yang, N. D.; Zhang, J.; Xue, Y.; Codogno, P.; Shen, H. M. Activation of lysosomal function in the course of autophagy via mTORC1 suppression and autophagosome-lysosome fusion. *Cell Res.* **2013**, *23*, 508-523.

150. Hsiao, J. K.; Tsai, C. P.; Chung, T. H.; Hung, Y.; Yao, M.; Liu, H. M.; Mou, C. Y.; Yang, C. S.; Chen, Y. C.; Huang, D. M. Mesoporous silica nanoparticles as a delivery system of gadolinium for effective human stem cell tracking. *Small* **2008**, *4*, 1445-1452.

151. Lu, J.; Liong, M.; Li, Z.; Zink, J. I.; Tamanoi, F. Biocompatibility, biodistribution, and drug-delivery efficiency of mesoporous silica nanoparticles for cancer therapy in animals. *Small* **2010**, *6*, 1794-1805.

152. Vivero-Escoto, J. L.; Taylor-Pashow, K. M.; Huxford, R. C.; Della Rocca, J.; Okoruwa, C.; An, H.; Lin, W.; Lin, W. Multifunctional mesoporous silica nanospheres with cleavable Gd(III) chelates as MRI contrast agents: synthesis, characterization, target-specificity, and renal clearance. *Small* **2011***, 7*, 3519-3528.

153. Roggers, R. A.; Lin, V. S.; Trewyn, B. G. Chemically reducible lipid bilayer coated mesoporous silica nanoparticles demonstrating controlled release and HeLa and normal mouse liver cell biocompatibility and cellular internalization. *Mol. Pharm.* **2012***, 9*, 2770-2777.

154. Hodgetts, S. I.; Simmons, P. J.; Plant, G. W. Human mesenchymal precursor cells (Stro-1(+)) from spinal cord injury patients improve functional recovery and tissue sparing in an acute spinal cord injury rat model. *Cell Transplant.* **2013***, 22*, 393-412.

155. Williams, E. L.; White, K.; Oreffo, R. O. Isolation and enrichment of Stro-1 immunoselected mesenchymal stem cells from adult human bone marrow. *Methods Mol. Biol.* **2013***, 1035*, 67-73.

156. Zhang, Y.; Zhao, D.; Tian, C.; Li, F.; Li, X.; Zhang, L.; Yang, H. Stro-1-positive human mesenchymal stem cells prolong skin graft survival in mice. *Transplant. Proc.* **2013***, 45*, 726-729.

157. Samsonraj, R. M.; Rai, B.; Sathiyanathan, P.; Puan, K. J.; Rotzschke, O.; Hui, J. H.; Raghunath, M.; Stanton, L. W.; Nurcombe, V.; Cool, S. M. Establishing criteria for human mesenchymal stem cell potency. *Stem Cells* **2015***, 33*, 1878-1891.

158. Mummery, C.; Ward, D.; van den Brink, C. E.; Bird, S. D.; Doevendans, P. A.; Opthof, T.; Brutel de la Riviere, A.; Tertoolen, L.; van der Heyden, M.; Pera, M. Cardiomyocyte differentiation of mouse and human embryonic stem cells. *J. Anat.* **2002***, 200*, 233-242.

159. Ridgway, J. P. Cardiovascular magnetic resonance physics for clinicians: part I. *J. Cardiovasc. Magn. Reson.* **2010***, 12*, 71-429X-12-71.

160. D'Ippolito, G.; Diabira, S.; Howard, G. A.; Menei, P.; Roos, B. A.; Schiller, P. C. Marrow-isolated adult multilineage inducible (MIAMI) cells, a unique population of postnatal young and old human cells with extensive expansion and differentiation potential. *J. Cell. Sci.* **2004***, 117*, 2971-2981.

161. Westerman, K. A.; Leboulch, P. Reversible immortalization of mammalian cells mediated by retroviral transfer and site-specific recombination. *Proc. Natl. Acad. Sci. U. S. A.* **1996***, 93*, 8971-8976.

162. PITOT, H. C.; PERAINO, C.; MORSE, P. A.,Jr; POTTER, V. R. Hepatomas in Tissue Culture Compared with Adapting Liver in Vivo. *Natl. Cancer Inst. Monogr.* **1964***, 13*, 229-245.

163. Summerhayes, I. C.; Franks, L. M. Effects of donor age on neoplastic transformation of adult mouse bladder epithelium in vitro. *J. Natl. Cancer Inst.* **1979**, *62*, 1017-1023.

164. Luo, Y.; Knudson, M. J. Mycobacterium bovis bacillus Calmette-Guerin-induced macrophage cytotoxicity against bladder cancer cells. *Clin. Dev. Immunol.* **2010**, *2010*, 357591.

165. Kempen, P. J.; Greasley, S.; Parker, K. A.; Campbell, J. L.; Chang, H. Y.; Jones, J. R.; Sinclair, R.; Gambhir, S. S.; Jokerst, J. V. Theranostic mesoporous silica nanoparticles biodegrade after pro-survival drug delivery and ultrasound/magnetic resonance imaging of stem cells. *Theranostics* **2015**, *5*, 631-642.

166. Janic, B.; Rad, A. M.; Jordan, E. K.; Iskander, A. S.; Ali, M. M.; Varma, N. R.; Frank, J. A.; Arbab, A. S. Optimization and validation of FePro cell labeling method. *PLoS One* **2009**, *4*, e5873.

167. Tabayoyong, W. B.; Salas, J. G.; Bonde, S.; Zavazava, N. HOXB4-transduced embryonic stem cell-derived Lin-c-kit+ and Lin-Sca-1+ hematopoietic progenitors express H60 and are targeted by NK cells. *J. Immunol.* **2009**, *183*, 5449-5457.

168. Cornetta, K.; Anderson, W. F. Protamine sulfate as an effective alternative to polybrene in retroviral-mediated gene-transfer: implications for human gene therapy. *J. Virol. Methods* **1989**, *23*, 187-194.

169. Choi, H. S.; Liu, W.; Misra, P.; Tanaka, E.; Zimmer, J. P.; Itty Ipe, B.; Bawendi, M. G.; Frangioni, J. V. Renal clearance of quantum dots. *Nat. Biotechnol.* **2007**, *25*, 1165-1170.